AD-A224 068

AL-TR-90-033   AD:

Final Report
for the period
January 1989
to May 1990

SPECTROSCOPY OF PROPELLANT-RELATED FLAMES

June 1990

Author:
T. Edwards

Approved for Public Release

Distribution is unlimited. The AL Technical Services Office has reviewed this report, and it is releasable to the National Technical Information Service, where it will be available to the general public, including foreign nationals.

Astronautics Laboratory (AFSC)
Air Force Space Technology Center
Space Systems Division
Air Force Systems Command
Edwards AFB CA 93523-5000

DTIC
ELECTE
JUL 20 1990
S B D

90 07 18 014

NOTICE TO ACCOMPANY THE DISSEMINATION OF
EXPORT-CONTROLLED TECHNICAL DATA

1. Export of information contained herein, which includes, in some circumstances, release to foreign nationals within the United States, without first obtaining approval or license from the Department of State for items controlled by the International Traffic in Arms Regulations (ITAR), or the Department of Commerce for items controlled by the Export Administration Regulations (EAR), may constitute a violation of law.

2. Under 22 U.S.C. 2778 the penalty for unlawful export of items or information controlled under the ITAR is up to 2 years imprisonment, or a fine of $100,000, or both. Under 50 U.S.C., Appendix 2410, the penalty for unlawful export of items or information controlled under the EAR is a fine up of up to $1,000,000, or five times the value of the exports, whichever is greater; or for an individual, imprisonment of up to 10 years, or a fine of up to $250,000, or both.

3. In accordance with your certification that establishes you as a "qualified U.S. contractor," unauthorized dissemination of this information is prohibited and may result in disqualification as a qualified U.S. contractor, and may be considered in determining your eligibility for future contracts with the Department of Defense.

4. The U.S. Government assumes no liability for direct patent infringement, or contributory patent infringement or misuse of technical data.

5. The U.S. Government does not warrant the adequacy, accuracy, currency, or completeness of the technical data.

6. The U.S. Government assumes no liability for loss, damage, or injury resulting from manufacture or use for any purpose of any product, article, system, or material involving reliance upon any or all technical data furnished in response to the request for technical data.

7. If the technical data furnished by the Government will be used for commercial manufacturing or other profit potential, a license for such use may be necessary. Any payments made in support of the request for data do not include or involve any license rights.

8. A copy of this notice shall be provided with any partial or complete reproduction of these data that are provided to qualified U.S. contractors.

NOTICE

When U. S. Government drawings, specifications, or other data are used for any purpose other than a definitely related Government procurement operation, the fact that the Government may have formulated, furnished, or in any way supplied the said drawings, specifications, or other data, is not to be regarded by implication or otherwise, or in any way licensing the holder or any other person or corporation, or conveying any rights or permission to manufacture, use , or sell any patented invention that may be related thereto.

FOREWORD

This report summarizes the solid propellant related experimental and modeling results obtained during the Combustion Sciences project in the Combustion Research Laboratory at the Air Force Astronautics Laboratory. This report covers the period 1/89-5/90. AL project manager during this time was Tim Edwards. The project was funded by the Aerospace Sciences Directorate of AFOSR.

This technical report has been reviewed and is approved for release and distribution in accordance with the distribution statement on the cover and on the DD Form 1473.

TIM EDWARDS
Project Manager

LAWRENCE P. QUINN
Chief, Aerothermochemistry Branch

FOR THE DIRECTOR

MICHAEL L. HEIL, Lt Col, USAF
Deputy Director, Astronautical
Sciences Division

REPORT DOCUMENTATION PAGE

1a. REPORT SECURITY CLASSIFICATION	1b. RESTRICTIVE MARKINGS
UNCLASSIFIED	

2a. SECURITY CLASSIFICATION AUTHORITY	3. DISTRIBUTION / AVAILABILITY OF REPORT
	Approved for public release.
2b. DECLASSIFICATION / DOWNGRADING SCHEDULE	Distribution is unlimited.

4. PERFORMING ORGANIZATION REPORT NUMBER(S)	5. MONITORING ORGANIZATION REPORT NUMBER(S)
AL-TR-90-033	

6a. NAME OF PERFORMING ORGANIZATION	6b. OFFICE SYMBOL (If applicable)	7a. NAME OF MONITORING ORGANIZATION
Astronautics Laboratory (AFSC)	AL/LSCC	

6c. ADDRESS (City, State, and ZIP Code)	7b. ADDRESS (City, State, and ZIP Code)
AL/LSCC Edwards AFB, CA 93523-5000	

8a. NAME OF FUNDING / SPONSORING ORGANIZATION	8b. OFFICE SYMBOL (If applicable)	9. PROCUREMENT INSTRUMENT IDENTIFICATION NUMBER

8c. ADDRESS (City, State, and ZIP Code)	10. SOURCE OF FUNDING NUMBERS			
	PROGRAM ELEMENT NO.	PROJECT NO.	TASK NO.	WORK UNIT ACCESSION NO.
	61102F	2308	M1	Q2

11. TITLE (Include Security Classification)

Spectroscopy of Propellant-Related Flames (U)

12. PERSONAL AUTHOR(S) Edwards, Tim

13a. TYPE OF REPORT	13b. TIME COVERED FROM 89/1 TO 90/5	14. DATE OF REPORT (Year, Month, Day) 9006	15. PAGE COUNT 132
Interim			

16. SUPPLEMENTARY NOTATION

17.	COSATI CODES		18. SUBJECT TERMS (Continue on reverse if necessary and identify by block number)
FIELD	GROUP	SUB-GROUP	Laser-Induced Fluorescence; Combustion Spectroscopy, Chemical Kinetics; Solid Propellant Combustion .
21	08		

19. ABSTRACT (Continue on reverse if necessary and identify by block number)

This report summarizes the progress made in solid propellant flame chemistry studies, from 1/89 to 5/90 during the Combustion Sciences project at the Astronautics Laboratory. This work involves LIF studies of OH, CN, NO, and C_2. Success was achieved in laboratory flame studies, but was rare in solid propellant applications. Preliminary studies in a hydrazine/methane/nitrogen dioxide diffusion flame yielded emission spectra from OH, NH, CN, CH, and C_2. The vibrational temperatures of the NH and CN were consistent with published mechanisms for chemiluminescent excitation. Chemical kinetic studies of high pressure propellant flame yielded inconclusive results because of gaps in the knowledge of the combustion mechanisms of important species such as CN and NO_2.

20. DISTRIBUTION / AVAILABILITY OF ABSTRACT	21. ABSTRACT SECURITY CLASSIFICATION
☒ UNCLASSIFIED/UNLIMITED ☐ SAME AS RPT. ☐ DTIC USERS	Unclassified/Unlimited distribution

22a. NAME OF RESPONSIBLE INDIVIDUAL	22b. TELEPHONE (Include Area Code)	22c. OFFICE SYMBOL
Tim Edwards	(805) 275-5656	AL/LSCC

DD Form 1473, JUN 86 — Previous editions are obsolete. — SECURITY CLASSIFICATION OF THIS PAGE

TABLE OF CONTENTS

LIST OF FIGURES

LIST OF FIGURES (continued)

LIST OF FIGURES (continued)

LIST OF TABLES

INTRODUCTION

The purpose of this technical report is to document experimental and modeling results obtained during FY 89 and FY90 on the High Pressure Combustion Kinetics (E3) and Combustion Sciences (Q2) projects. This work was performed in the Combustion Research Laboratory at the Astronautics Laboratory (AFSC). In general, the experiments involved the spectroscopic study of propellant flames. The modeling work involved chemical kinetic modeling of solid propellant flame chemistry. Previous work can be found in References 1-8.

The next section ("Laser-Induced Fluorescence Measurements") reports attempts to apply laser-induced fluorescence (LIF) measurements of various molecules to solid propellant flames. "Hydrazine Diffusion Flame Experiments" presents initial results obtained in the study of hydrazine diffusion flames at low pressure. The last section ("Chemical Kinetic Modeling") presents the chemical kinetic modeling results. The buildup of the hydrazine burner occurred in projects G5 and Q3. Future results obtained from this burner will be reported under the UV Mechanisms project (N3).

The composition of the propellants discussed in this report is listed in Table 1. Further information can be found in Reference 5.

Table 1. Propellant Formulations.

	HMX1	HMX2	AP1	AP2	AN1	DB1	DB2
Ingredient, wt % (approx)							
HMX (200/20 μm)	73	80	0	0	0	0	0
polyester binder	10	20	0	0	0	29	27
TMETN	17	0	0	0	12	0	0
NG	0	0	0	0	0	71	67
AP (400/20/2 μm)	0	0	87	68	0	0	6
Polybutadiene binder	0	0	13	16	0	0	0
AN	0	0	0	0	16	0	0
GAP binder	0	0	0	0	16	0	0
Aluminum powder	0	0	0	16	0	0	0

HMX=cyclotetramethylene tetranitramine $C_4H_8N_8O_8$, TMETN=trimethylolethanetrinitrate $C_5H_9O_9N_3$, NG=nitroglycerin $C_3H_5N_3O_9$, AP=ammonium perchlorate NH_4ClO_4, AN=ammonium nitrate NH_4NO_3, GAP=glycidyl azide polymer. The "polyester" binder in the DB propellants is a polyethylene glycol-based polymer ("PEG"), while the HMX binder is based on polydiethylene glycol adipate ("PGA").

LASER-INDUCED FLUORESCENCE MEASUREMENTS

OH LIF TEMPERATURE MEASUREMENTS

In recent OH LIF measurements at the Astronautics Laboratory, a detection system employing a much smaller bandpass coupled with a double spectrometer (Spex 1404) has been used to increase the light rejection capabilities of the experiment, compared with earlier work [6,7]. The bandpass was decreased from 20 nm to 0.45 nm, as shown in Figure 1. Wide detection bandpass is desirable because it greatly simplifies the calculation of a rotational temperature [9]. This decrease in bandpass increases the light rejection capability of the detection system at the expense of ease of calculating a rotational temperature from the data. The narrow bandpass was centered on the OH 1,1 R_1 bandhead so that LIF from the OH 1,1 $R_1$1-$R_1$10 transitions was collected. It was hoped that this detection bandpass would increase light rejection while providing an accurate sample of the LIF. Successful OH LIF measurements were made using this system, as shown in Figures 2 and 3. In Figure 2, an OH LIF profile in an atmospheric pressure (N_2 atmosphere) flame of an 87% ammonium perchlorate, 13% polybutadiene binder propellant is shown. The profile was measured by allowing the propellant to burn down through the laser beam/collection volume [4,5]. The transmission of the laser across the surface is also shown, giving a relatively accurate location of the surface. The "spikes" in the LIF data below the surface come from reflections of the laser off the side of the propellant strand. The corresponding experiment with the laser detuned from an OH resonance is shown in Figure 3, demonstrating the capability of the detection system to differentiate between OH LIF and scattering at the laser wavelength. This discrimination didn't occur in the "wide" bandpass experiments [6,7]. The experiment corresponding to Figure 2 was attempted in the HMX1 propellant at 18 atm, but no detectable OH LIF signal was measured. This is perhaps not surprising since the equilibrium OH concentration in the AP propellant flame is 15 times greater than that in the HMX1 propellant flame (0.014 vs 0.0009 mole fraction), indicative of the dramatically different stoichiometries in the two propellant flames (calculations made with NASA Lewis thermochemical code). Quenching is probably much more important at the higher pressure also, decreasing the LIF signal strength. The "good news" is that no scattering was seen, indicating that the measurement can be successful in a high pressure, highly scattering environment, provided that a sufficient amount of OH is present. For comparison, the equilibrium OH mole fraction in a pure HMX flame at 18 atm is 0.017, indicating that such an OH LIF temperature measurement in a strand of pure HMX might be successful.

If one has two profiles such as the one shown in Figure 2, with the only difference between the two being the OH transition excited, then it is relatively simple to calculate a rotational temperature [6,10]. This was done in the AP propellant flame using the OH 1,0 $R_1$4 and $R_1$10 transitions. Note that the directly coupled OH 1,1 $R_1$4 and $R_1$10 lines (312.395 and 312.247 nm, respectively) are within the detection bandpass. Then, with the two excitation lines denoted by subscripts 1 and 2: $kT/hc = (E_{r1}-E_{r2})/\ln[(I_{fl}/g''B)_1/(I_{fl}/g''B)_2]$ in the unsaturated case and $kT/hc = (E_{r1}-E_{r2})/\ln\{[I_{fl}(1/g''+1/g')]_1/[I_{fl}(1/g''+1/g')]_2\}$ for the saturated case. In these equations, I_{fl} is the collected LIF intensity, E_r is the rotational energy of the transition, B is the absorption coefficient and g is the degeneracy [6]. The reproducibility of the data was only fair, so three experiments with each excited transition were averaged and the resulting OH

3

rotational temperature profile is shown in Figure 4 for the unsaturated case. For highest accuracy, the data should be corrected for partial saturation [6,11]. In the partially saturated regime, the rotational temperatures yielded by the main and satellite branches differ when either total saturation or unsaturation is assumed. Since this correction was not made, the temperature profile in Figure 4 is only a rough estimate at this point. To calculate a more accurate rotational temperature from the narrow bandpass data will require background experiments in a flame, ideally a flame with a similar pressure and stoichiometry to the propellant flame. In some preliminary work in a CH_4/N_2O flame, an excitation scan was performed with the narrow detection bandpass. The result is shown in Figure 5. Rather than the straight line found with wide detection bandpass [6,10], the Boltzmann plot shows some substantial scatter. The temperature is also higher than that found with wide detection bandpass. Thus, accurate temperature measurements will require calibration in a flame with a known temperature profile. In summary, then, it has been demonstrated that OH LIF temperature measurements can be made with this type of detection system, although the OH concentration must be relatively high. OH absorption temperature measurements have also been reported in high pressure solid propellant flames [12], as have CARS temperature measurements [13]. Both of these techniques have lower spatial resolution than the potential possible for OH LIF temperature measurements, but have yielded more successful results thus far.
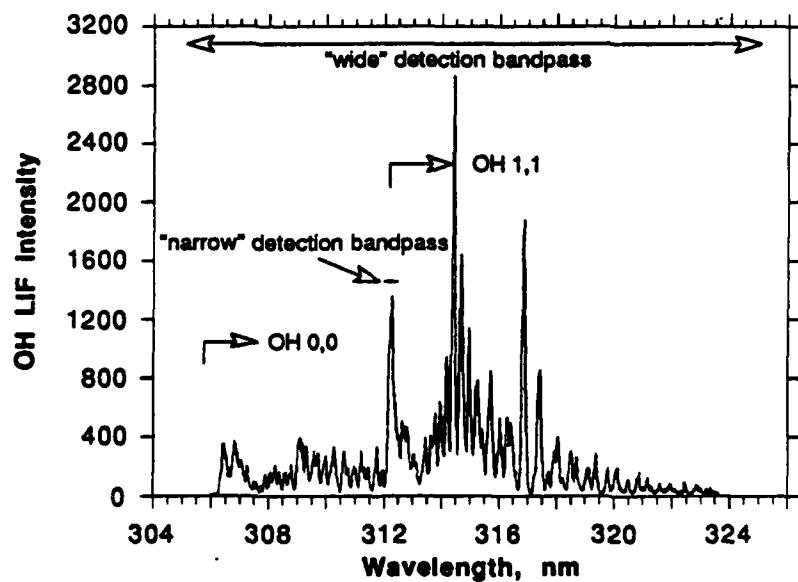
Figure 1. Bandpass comparisons for OH LIF temperature measurements. The narrow bandpass is 312.25 ± 0.22 nm, encompassing the OH 1,1 R_14-$R_1 11$ lines.
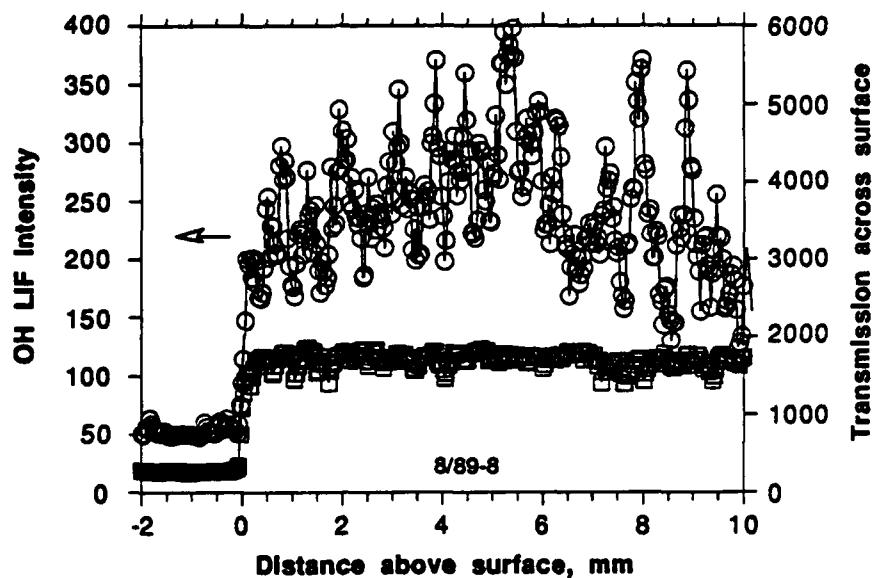
Figure 2. **Results of OH LIF "burndown" experiment.** AP propellant, 1 atm N_2, 0.2 mJ/pulse in flame, 50 Hz, OH 1,0 $R_1$10 excitation (281.537 nm), slit: 200 μm X 1 cm projected 1:1 on flame (≈spatial resolution), single pulse (no averaging), 1.7 mm/s propellant burn rate. Data offset from zero on Y axes for clarity.
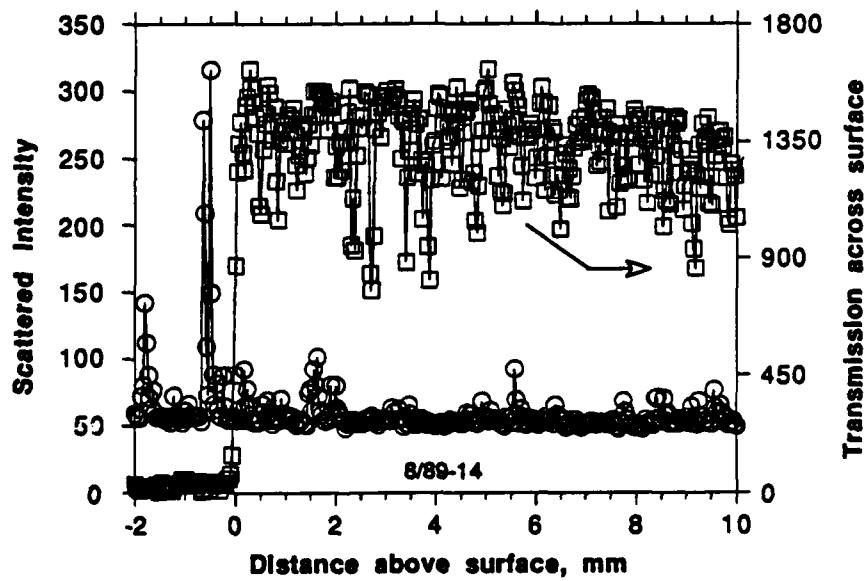
Figure 3. **Same as Figure 2, except laser detuned from OH resonance lines (281.11 nm).**

5
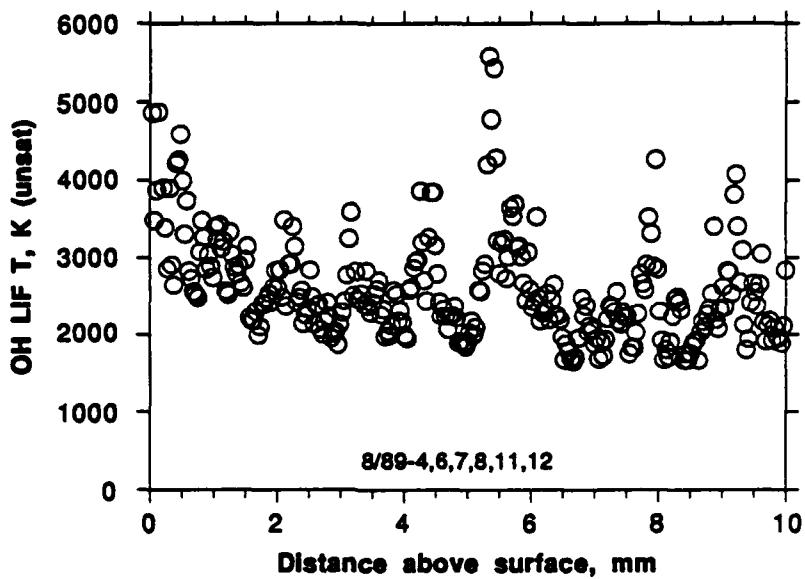
Figure 4. AP propellant temperature profile. Obtained for unsaturated case with $R_1 4$ and $R_1 10$ profiles (e.g., Figure 2). The average of three experiments for each excitation line was used. The adiabatic flame temperature for this propellant is about 2900 K.
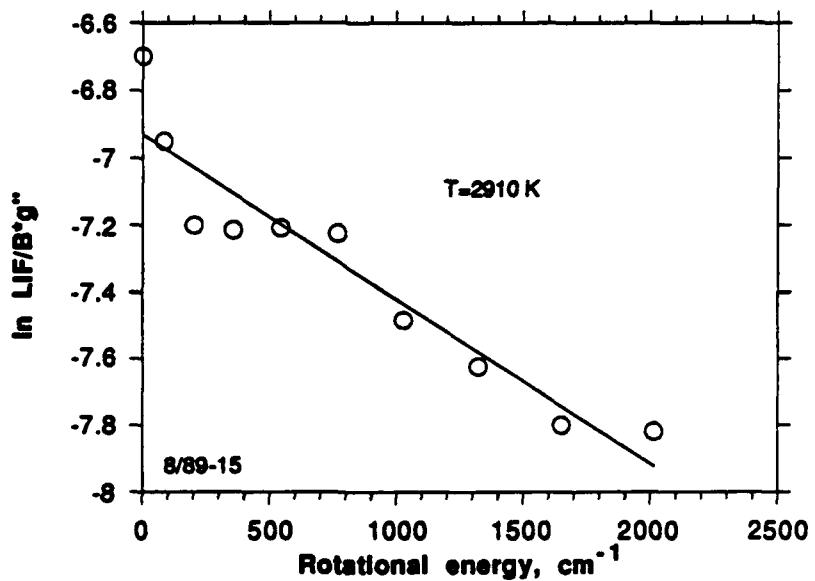
Figure 5. Results of excitation scan (Boltzmann plot) in CH_4/N_2O flame using "narrow" detection bandpass. 0.4 mJ/pulse in flame, laser scanned from 281.1 to 281.6 nm (OH 1,0 $R_1 1$-$R_1 10$).

CN LIF MEASUREMENTS

Several CN LIF excitation spectra have been reduced obtain a rotational temperature. This may be of interest as an alternative temperature measurement in the reaction zone of flames although OH would be better for general use since OH is found throughout flames, while CN is found only in the "reaction zone." Relatively extensive CN LIF experiments in solid propellant flames have been performed at AL [4,5] although the signal levels would be marginal at best for temperature measurements similar to those discussed below. In any case, both the propellant and excitation scan measurements were made by exciting the CN 0,1 transition at ~421 nm and detecting the CN 0,0 band at ~388 nm, as shown in Figures 6-8. In Figure 7, the CN 0,0 LIF spectrum from excitation of the CN 0,1 P branch bandhead at 421.6 nm is shown. In Figure 8, the CN 0,1 excitation scan is shown, with the detection bandpass of 0.09 nm approximately centered on the 388.3 nm CN LIF P branch peak shown in Figure 7. These measurements were performed in a conical premixed CH_4/N_2O flame above a 0.2 inch tube [5], at the tip of the "inner cone", where the CN LIF signal is maximum. The result of a brief examination of the CN LIF intensity vs laser power is shown in Figure 9. Thus, the excitation scan of Figure 8 is apparently partially saturated. A problem with this scheme is the possibility of self-absorption of the emitted radiation in the 0,0 band. Significant self-absorption has been seen in a 50 torr CH_4/N_2O premixed flat flame in this laboratory using 0,1 excitation/0,0 detection.

To obtain a temperature from Figure 8, first the CN lines must be identified. Only limited literature data was found for the 0,1 band (N=1-29, doublets not resolved [15]), so the CN 0,1 lines were calculated. This was done by creating a "synthetic" CN 0,1 spectrum using standard techniques and data [14-17]. The program is a modification of the program listed in Reference 5, with the data listed in Tables 2 and 3. The model data matched literature CN line data fairly well, as is shown in Figures 10 and 11. The model and experimental CN LIF data were then compared and line identification was relatively easy, as shown in Figures 12, 13 and 14. The peak heights were then (roughly) measured, and Boltzmann plots were constructed as shown in Figures 15 and 16. The same process was performed for an excitation scan performed at lower power, with the Boltzmann plots shown in Figures 17 and 18. The resulting temperature of about 1700 K (only the "unsaturated" temperatures were reasonable) were somewhat lower than the 2600 K measured in the same flame with OH LIF [6], which seems possible since the CN excitation scans were performed in the region of the flame with maximum CN signal (the "reaction" zone), while the OH LIF excitation scans were performed in the region above the reaction zone. However, modeling and experimental measurements of CN in flames in References 7 and 11 and in the modeling section of this report show the CN peak occurs where the flame temperature first reaches its maximum. Thus, it is also possible that the excitation scans are yielding temperatures that are substantially lower than the correct value. Perhaps the fact that the laser is exciting v"=1 is contributing to this error. It would be interesting to determine the CN rotational temperature in a flame with a known T distribution. Since the LIF is collected from the 0,0 band, there is a possibility that self-absorption is also important. The partial resolution of the two spin components also leads to errors in the data. The partial resolution of the CN lines was corrected for when reducing the excitation scan data by calculating a correction factor based upon how well resolved the peaks were. For totally unresolved peaks (N"≤20), the factor was 1. Totally resolved peaks had a factor of 0, with the

partially resolved peaks in between. The peak height was then divided by 1+correction factor. For example, the height of the P_1 10 + P_2 10 unresolved doublet was divided by 2 to obtain the heights of the individual P_1 10 and P_2 10 lines, while the P_1 37 peaks were divided by 1.3 to account for the contribution of one peak to the height of the other. Another obvious conclusion is that the R branch would be better for temperature measurements, since there is no bandhead to confuse the measurement. Note that the structure of the CN 0,1 P branch is inconvenient for temperature measurements for another reason: the rotational levels with the highest population (Fig. 19) coincide with the bandhead. As can be seen by the laser power vs wavelength curve in Figure 8, however, the dye used in these experiments (Coumarin 120) would not be useful for such a measurement. Bis-MSB would be better [5]. In reducing the data, the line strength was calculated as in Herzberg, rather than using tabular Einstein coefficients as in OH temperature measurements [17].

Another experiment was performed that included more CN lines. The new lines are illustrated in Figures 20 and 21. The lines were easy to assign, as shown in Figure 22. However, the Boltzmann plot still yielded lower temperatures, as shown in Figure 23. Another possible source of error is the detection bandpass used (0.09 nm for Figures 15,16 and 0.22 nm for Figures 17,18). Assuming that the bandpass is centered to include the maximum number of CN lines, a bandpass of 0.09 nm would include N=20 to 36 P branch lines, while a bandpass of 0.22 nm would include N=15 to 41. Thus, the bandpasses for Figures 15-18 includes the directly excited lines at high rotational energy, but not at low rotational energy. Thus, the two sets of points should not be expected to fall on the same Boltzmann curve. Obviously, more careful attention must be paid to bandpass (as in OH). However, a small bandpass is required to enhance the light rejection for propellant experiments. A better bandpass would be 0.76 nm (387.58 to 388.34 nm), which includes all the P branch lines from N=1 to 56 and none of the R branch lines. The CN LIF intensity vs bandpass behavior is shown in Figure 24.

$T = T_e + G(v) + F(N) = T_e + \omega_e (v+0.5) - \omega_e x_e(v+0.5)^2 + B_v N(N+1) - D_v N^2(N+1)^2$
where $N = K$ in Herzberg [14]

$F_1(N) = B_v N(N+1) - D_v N^2(N+1)^2 + 0.5\gamma N$ $J=N+0.5$
$F_2(N) = B_v N(N+1) - D_v N^2(N+1)^2 - 0.5\gamma(N+1)$ $J=N-0.5$

then, energy (wavenumber) of transition is $v = T'-T''$, for P branch N'-N"=-1, R branch N'-N"=1
line strength: (Honl-London factor) $S_p=N$, $S_r=N+1$ for $\Lambda=0$ (Σ-Σ transition)

Data from Engleman [16] (B_v, D_v, γ) and Huber and Herzberg [21] (ω_e, $\omega_e x_e$, T_e):
For CN 0,1 band v'=0, v"=1:

$B_v'=1.95874$	$B_v^{\wedge}=1.87364$	$T_e=25751.8$ cm^{-1}
$D_v'=6.58 \times 10^{-6}$	$D_v''=6.42 \times 10^{-6}$	
$\gamma'=15.65 \times 10^{-3}$	$\gamma''=5.96 \times 10^{-3}$	
$\omega_e'=2163.90$	$\omega_e''=2068.59$	
$\omega_e x_e'=20.2$	$\omega_e x_e''=13.087$	

For 0,0 band (v"=0):

$B_v''=1.8910$
$D_v''=6.41 \times 10^{-6}$
$\gamma''=6.16 \times 10^{-3}$
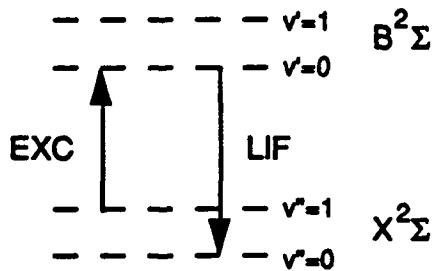
Figure 6. CN LIF schematic for 0,1 band excitation--0,0 band detection.

Table 3: Calculated lines for CN 0,1 band including Jevons data [15]. Doublets not resolved in [15].

N"	P_1	P_2	R_1	R_2	Jevons P	Jevons R
0			420.7711	420.7715		420.7691
1	420.9071	420.9071	420.6987	420.6992	420.9040	420.6957
2	420.9704	420.9706	420.6233	420.6239	420.9670	420.6212
3	421.0307	421.0311	420.5448	420.5457	421.0270	420.5423
4	421.0880	421.0885	420.4634	420.4645	421.0850	420.4613
5	421.1423	421.1429	420.3791	420.3803	421.1400	420.5542
6	421.1935	421.1944	420.2917	420.2931	421.1910	420.2909
7	421.2418	421.2428	420.2015	420.2030	421.2390	420.2008
8	421.2870	421.2881	420.1083	420.1100	421.2860	420.1065
9	421.3291	421.3305	420.0121	420.0140	421.3270	420.0109
10	421.3683	421.3698	419.9131	419.9151	421.3660	419.9108
11	421.4044	421.4060	419.8111	419.8133	421.4020	419.8096
12	421.4374	421.4393	419.7062	419.7086	421.4360	419.7044
13	421.4674	421.4695	419.5983	419.6009	421.4660	419.5917
14	421.4943	421.4966	419.4876	419.4904	421.4920	419.4876
15	421.5182	421.5206	419.3741	419.3770	421.5170	419.3730
16	421.5390	421.5416	419.2576	419.2607	421.5400	419.2570
17	421.5568	421.5596	419.1382	419.1414	421.5570	419.1366
18	421.5715	421.5744	419.0160	419.0194	421.5720	419.0157
19	421.5832	421.5862	418.8910	418.8945	421.5840	418.8902
20	421.5917	421.5950	418.7630	418.7668		
21	421.5972	421.6007	418.6323	418.6362		
22	421.5997	421.6033	418.4987	418.5028		
23	421.5990	421.6028	418.3624	418.3666		
24	421.5953	421.5992	418.2232	418.2276		
25	421.5885	421.5927	418.0811	418.0858		
26	421.5786	421.5829	417.9364	417.9412		
27	421.5657	421.5702	417.7888	417.7938		
28	421.5497	421.5544	417.6385	417.6436		
29	421.5306	421.5354	417.4855	417.4908		
30	421.5085	421.5134	417.3297	417.3351		
31	421.4832	421.4884	417.1711	417.1768		
32	421.4549	421.4602	417.0099	417.0157		
33	421.4235	421.4290	416.8459	416.8518		
34	421.3890	421.3947	416.6793	416.6853		
35	421.3515	421.3573	416.5099	416.5162		
36	421.3109	421.3169	416.3379	416.3443		
37	421.2672	421.2733	416.1632	416.1698		
38	421.2205	421.2268	415.9859	415.9926		
39 .	421.1706	421.1771	415.8059	415.8128		
40	421.1177	421.1244	415.6233	415.6303		
41	421.0618	421.0686	415.4381	415.4453		
42	421.0028	421.0098	415.2503	415.2577		
43	420.940`	420.9479	415.0598	415.0674		
44	420.8756	420.8830	414.8669	414.8746		
45	420.8074	420.8150	414.6714	414.6792		
46	420.7362	420.7439	414.4732	414.4813		
47	420.6619	420.6698	414.2726	414.2808		
48	420.5847	420.5927	414.0695	414.0778		
49	420.5043	420.5125	413.8639	413.8723		

Table 3: Calculated lines for CN 0,1 band including Jevons data [15] (cont).

N"	P_1	P_2	R_1	R_2	Jevons P	Jevons R
50	420.4209	420.4293	413.6557	413.6643		
51	420.3345	420.3431	413.4450	413.4539		
52	420.2451	420.2538	413.2320	413.2409		
53	420.1526	420.1615	413.0164	413.0255		
54	420.0572	420.0662	412.7984	412.8077		
55	419.9587	419.9679	412.5780	412.5874		
56	419.8572	419.8666	412.3552	412.3647		
57	419.7527	419.7623	412.1300	412.1397		
58	419.6453	419.6550	411.9024	411.9123		
59	419.5348	419.5446	411.6724	411.6824		
60	419.4213	419.4314	411.4401	411.4503		
61	419.3049	419.3151	411.2054	411.2158		
62	419.1855	419.1959	410.9685	410.9789		
63	419.0631	419.0737	410.7292	410.7399		
64	418.9379	418.9485	410.4876	410.4984		
65	418.8096	418.8204	410.2438	410.2547		
66	418.6784	418.6894	409.9977	410.0088		
67	418.5443	418.5555	409.7493	409.7606		
68	418.4072	418.4185	409.4987	409.5102		
69	418.2672	418.2787	409.2460	409.2575		
70	418.1243	418.1360	408.9910	409.0027		
71	417.9785	417.9903	408.7338	408.7456		
72	417.8297	417.8417	408.4745	408.4865		
73	417.6782	417.6903	408.2130	408.2252		
74	417.5237	417.5360	407.9494	407.9617		
75	417.3664	417.3788	407.6837	407.6960		
76	417.2061	417.2188	407.4158	407.4284		
77	417.0431	417.0559	407.1459	407.1586		
78	416.8772	416.8901	406.8739	406.8867		
79	416.7084	416.7216	406.5999	406.6129		
80	416.5369	416.5502	406.3238	406.3369		
81	416.3625	416.3759	406.0457	406.0590		
82	416.1854	416.1989	405.7656	405.7791		
83	416.0054	416.0191	405.4836	405.4971		
84	415.8226	415.8365	405.1995	405.2132		
85	415.6371	415.6511	404.9135	404.9274		
86	415.4488	415.4630	404.6256	404.6396		
87	415.2577	415.2721	404.3358	404.3499		
88	415.0639	415.0784	404.0440	404.0583		
89	414.8674	414.8821	403.7504	403.7648		
90	414.6682	414.6830	403.4550	403.4695		
91	414.4662	414.4812	403.1576	403.1723		
92	414.2616	414.2767	402.8585	402.8733		
93	414.0542	414.0695	402.5575	402.5724		
94	413.8442	413.8596	402.2547	402.2698		
95	413.6315	413.6471	401.9502	401.9654		
96	413.4162	413.4319	401.6439	401.6592		
97	413.1983	413.2141	401.3358	401.3513		
98	412.9777	412.9937	401.0261	401.0417		
99	412.7545	412.7707	400.7146	400.7303		

Table 4: Calculated line list for CN 0,0 band, including Engleman data [16].

N"	P_1	P_2	R_1	R_2	Engle. P_1	Engle. P_2	Engle. R_1	Engle. R_2
0			387.4635	387.4638			387.462	387.462
1	387.5793	387.5793	387.4026	387.4030	387.577	387.577	387.401	387.401
2	387.6341	387.6342	387.3397	387.3403	387.632	387.632	387.338	387.338
3	387.6868	387.6871	387.2747	387.2755	387.685	387.685	387.273	387.273
4	387.7375	387.7379	387.2078	387.2087	387.736	387.736	387.206	387.206
5	387.7861	387.7866	387.1389	387.1399	387.784	387.784	387.137	387.137
6	387.8327	387.8334	387.0679	387.0691	387.831	387.831	387.067	387.067
7	387.8773	387.8781	386.9951	386.9964	387.876	387.876	386.993	386.993
8	387.9198	387.9207	386.9202	386.9216	387.919	387.919	386.918	386.918
9	387.9602	387.9614	386.8433	386.8449	387.959	387.959	386.841	386.841
10	387.9987	387.9999	386.7644	386.7662	387.997	387.997	386.763	386.763
11	388.0350	388.0364	386.6837	386.6855	388.034	388.034	386.682	386.682
12	388.0693	388.0709	386.6009	386.6029	388.068	388.068	386.600	386.600
13	388.1016	388.1033	386.5162	386.5183	388.101	388.101	386.514	386.516
14	388.1318	388.1336	386.4295	386.4318	388.131	388.131	?	386.429
15	388.1599	388.1619	386.3409	386.3434	388.158	388.160	386.338	386.341
16	388.1859	388.1881	386.2504	386.2530	388.186	388.188	386.248	386.251
17	388.2100	388.2122	386.1579	386.1606	388.208	388.211	386.155	386.158
18	388.2318	388.2343	386.0635	386.0664	388.230	388.233	386.061	386.064
19	388.2517	388.2543	385.9672	385.9702	388.250	388.253	385.965	385.968
20	388.2695	388.2722	385.8690	385.8721	388.268	388.271	385.866	385.870
21	388.2852	388.2880	385.7689	385.7722	388.284	388.287	385.767	385.770
22	388.2988	388.3018	385.6668	385.6702	388.298	388.300	385.665	385.668
23	388.3103	388.3134	385.5629	385.5665	388.309	388.312	385.577	385.583
24	388.3198	388.3230	385.4571	385.4608	388.318	388.321	385.473	385.477
25	388.3271	388.3306	385.3495	385.3533	388.326	388.330	385.348	385.369
26	388.3324	388.3360	385.2399	385.2439	388.330	388.335	385.238	385.260
27	388.3357	388.3394	385.1285	385.1326	388.335	388.339	385.143	385.149
28	388.3368	388.3406	385.0152	385.0194	388.335	388.339	385.031	385.036
29	388.3358	388.3398	384.9001	384.9045	388.335	388.339		384.902
30	388.3328	388.3369	384.7831	384.7877				
31	388.3276	388.3319	384.6644	384.6690				
32	388.3204	388.3248	384.5437	384.5485				
33	388.3111	388.3157	384.4213	384.4262				
34	388.2997	388.3044	384.2971	384.3021				
35	388.2862	388.2911	384.1710	384.1762				
36	388.2707	388.2756	384.0432	384.0485				
37	388.2530	388.2581	383.9135	383.9190				
38	388.2333	388.2385	383.7821	383.7878				
39	388.2115	388.2169	383.6489	383.6547				
40	388.1875	388.1931	383.5140	383.5199				
41	388.1616	388.1672	383.3773	383.3833				
42	388.1335	388.1393	383.2389	383.2450				
43	388.1033	388.1093	383.0987	383.1050				
44	388.0710	388.0772	382.9568	382.9633				
45	388.0367	388.0430	382.8132	382.8198				
46	388.0004	388.0068	382.6679	382.6746				
47	387.9619	387.9684	382.5209	382.5277				
48	387.9214	387.9280	382.3722	382.3791				
49	387.8787	387.8856	382.2218	382.2289				
50	387.8340	387.8410	382.0697	382.0769				

Table 4: Calculated line list for CN 0,0 band, including Engleman data [16] (cont).

N"	P_1	P_2	R_1	R_2	Engle. P_1	Engle. P_2	Engle. R_1	Engle. R_2
51	387.7873	387.7944	381.9160	381.9234				
52	387.7385	387.7457	381.7606	381.7681				
53	387.6876	387.6950	381.6036	381.6112				
54	387.6346	387.6422	381.4449	381.4527				
55	387.5796	387.5873	381.2847	381.2925				
56	387.5226	387.5304	381.1227	381.1308				
57	387.4635	387.4714	380.9593	380.9674				
58	387.4023	387.4104	380.7942	380.8024				
59	387.3391	387.3473	380.6275	380.6359				
60	387.2738	387.2822	380.4592	380.4678				
61	387.2065	387.2151	380.2894	380.2981				
62	387.1372	387.1459	380.1180	380.1269				
63	387.0658	387.0746	379.9451	379.9541				
64	386.9924	387.0014	379.7707	379.7798				
65	386.9171	386.9261	379.5948	379.6039				
66	386.8396	386.8488	379.4173	379.4266				
67	386.7602	386.7695	379.2383	379.2477				
68	386.6787	386.6882	379.0578	379.0674				
69	386.5952	386.6048	378.8759	378.8856				
70	386.5097	386.5195	378.6924	378.7023				
71	386.4223	386.4322	378.5076	378.5175				
72	386.3328	386.3428	378.3213	378.3313				
73	386.2413	386.2515	378.1335	378.1437				
74	386.1479	386.1582	377.9443	377.9546				
75	386.0525	386.0629	377.7537	377.7642				
76	385.9550	385.9656	377.5617	377.5723				
77	385.8557	385.8664	377.3683	377.3790				
78	385.7543	385.7652	377.1736	377.1844				
79	385.6510	385.6620	376.9774	376.9883				
80	385.5458	385.5569	376.7799	376.7910				
81	385.4386	385.4499	376.5811	376.5923				
82	385.3295	385.3409	376.3809	376.3922				
83	385.2184	385.2299	376.1794	376.1908				
84	385.1054	385.1170	375.9766	375.9881				
85	384.9904	385.0023	375.7725	375.7841				
86	384.8736	384.8856	375.5670	375.5789				
87	384.7549	384.7669	375.3604	375.3723				
88	384.6342	384.6464	375.1524	375.1645				
89	384.5117	384.5240	374.9432	374.9554				
90	384.3872	384.3997	374.7328	374.7451				
91	384.2609	384.2735	374.5211	374.5335				
92	384.1327	384.1454	374.3083	374.3208				
93	384.0026	384.0155	374.0942	374.1068				
94	383.8707	383.8837	373.8789	373.8917				
95	383.7369	383.7500	373.6624	373.6753				
96	383.6012	383.6145	373.4448	373.4578				
97	383.4637	383.4771	373.2260	373.2391				
98	383.3245	383.3380	373.0061	373.0193				
99	383.1833	383.1970	372.7850	372.7984				
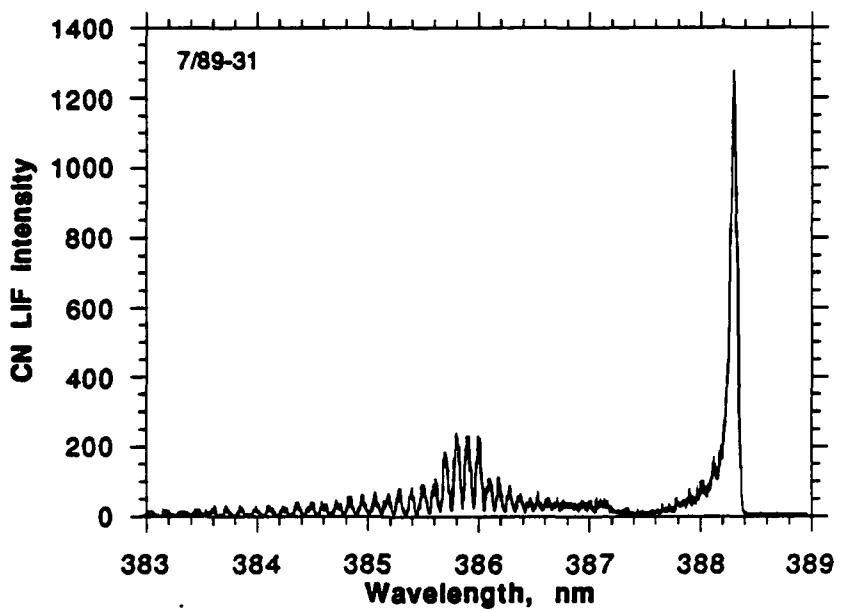
Figure 7. CN 0,0 LIF spectrum from 0,1 excitation. 0.15 mJ/pulse in flame, S1=100 μm X 1 cm, S4 =200 μm (0.09 nm detection bandpass), 421.6 nm excitation. S1, S4 refer to front and rear slits of double spectrometer.
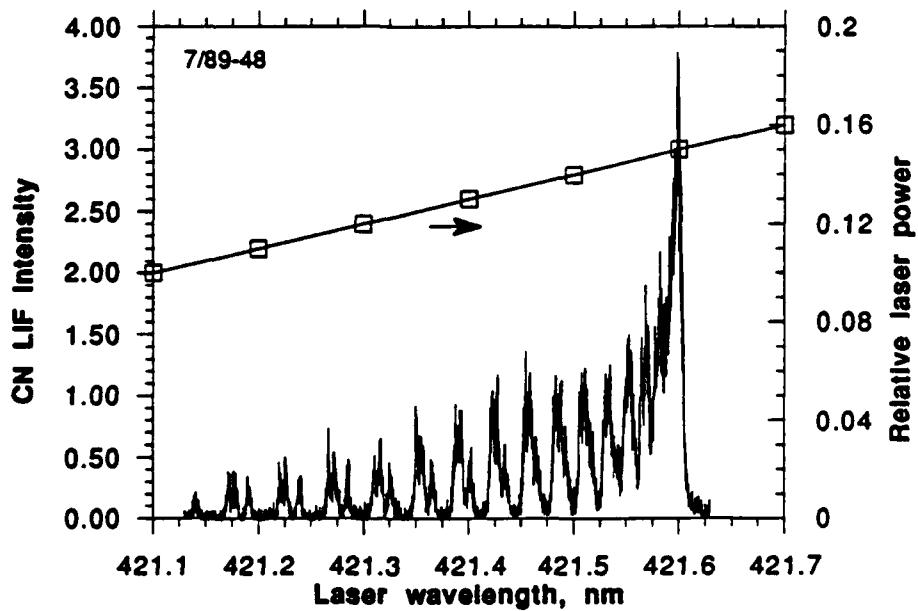
Figure 8. CN 1,0 LIF excitation spectrum. 0.6 mJ/pulse in flame (est.), S1=100 μm X 0.2 cm, S4=200 μm (0.09 nm detection bandpass).

14
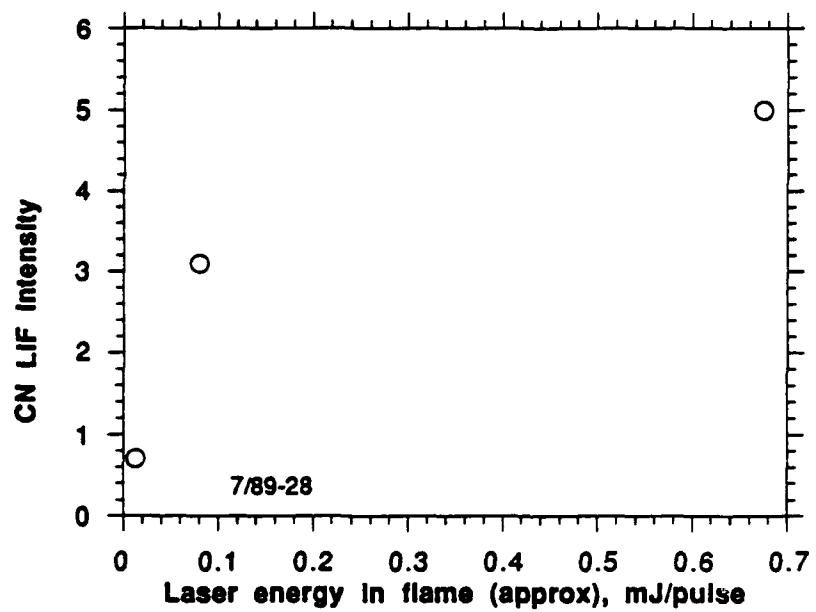
Figure 9. Laser power vs CN LIF intensity.
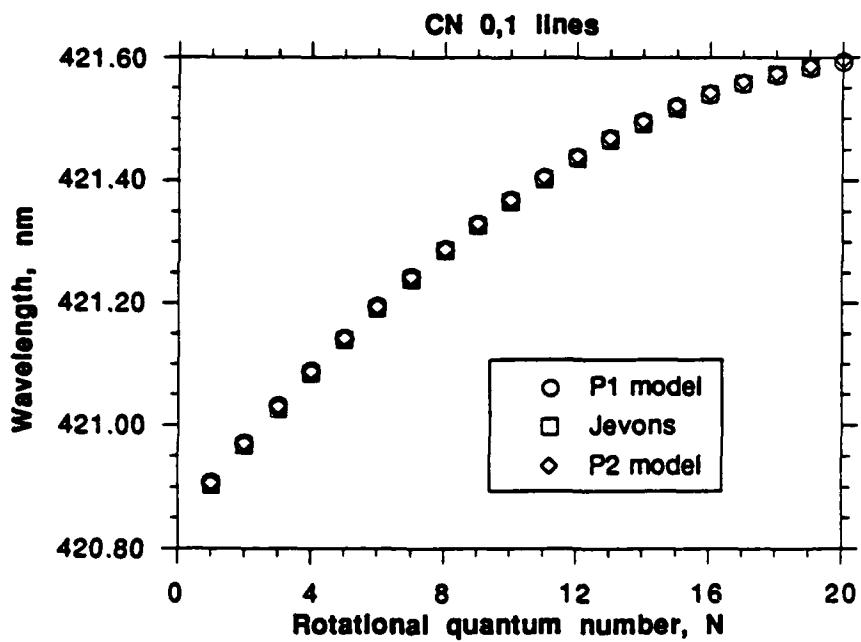
Figure 10. Comparison of model and Jevons data [15].
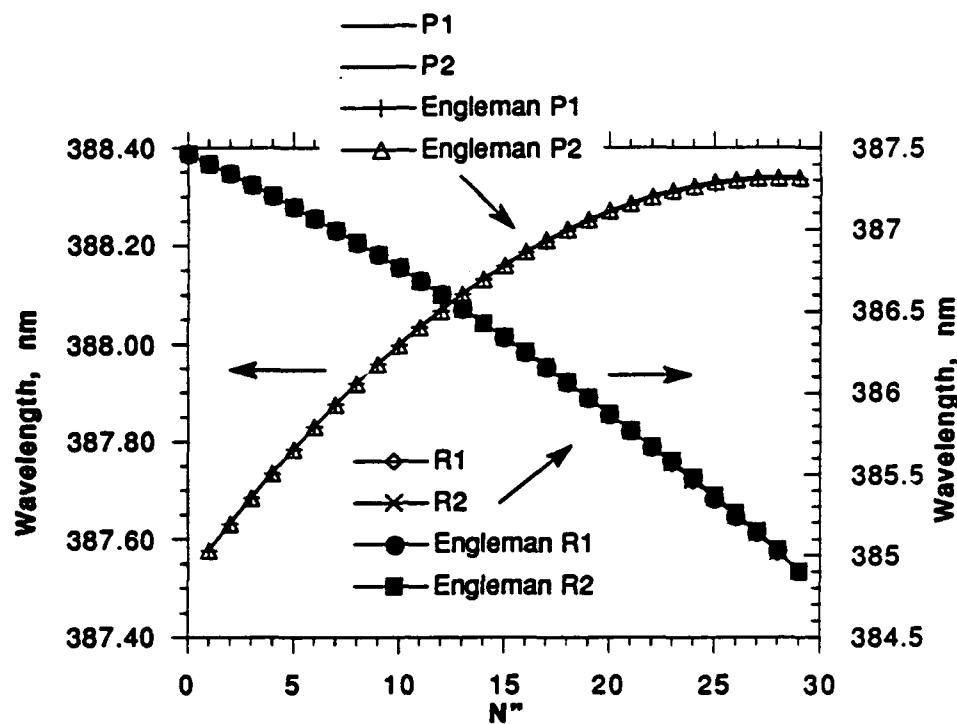
Figure 11. Comparison of model and Engleman data [16].
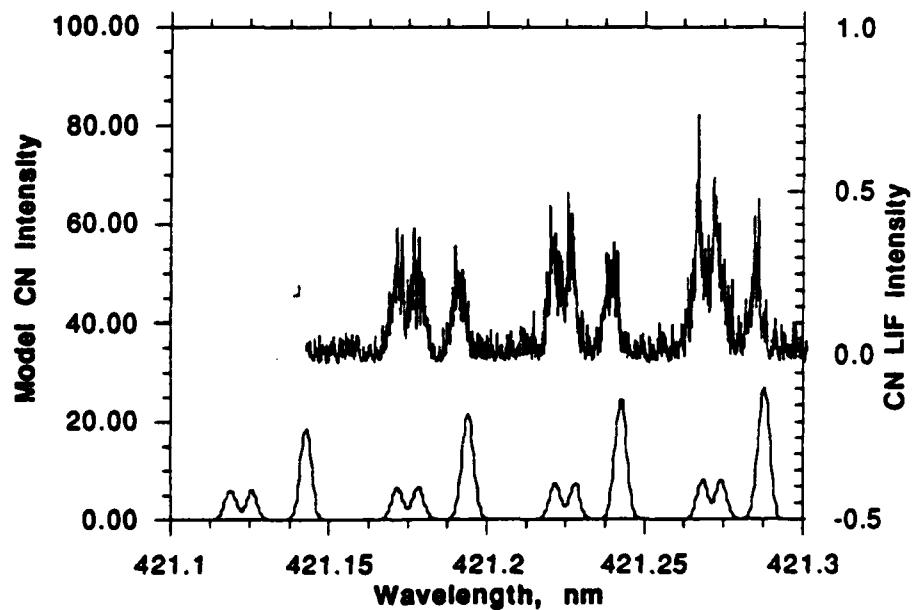
Figure 12. Comparison of model and experimental CN spectra #1. Dye laser bandwidth is 0.2 cm^{-1} (0.004 nm), same as model. Model yields Boltzmann distribution, so intensities aren't expected to match experimental LIF data.
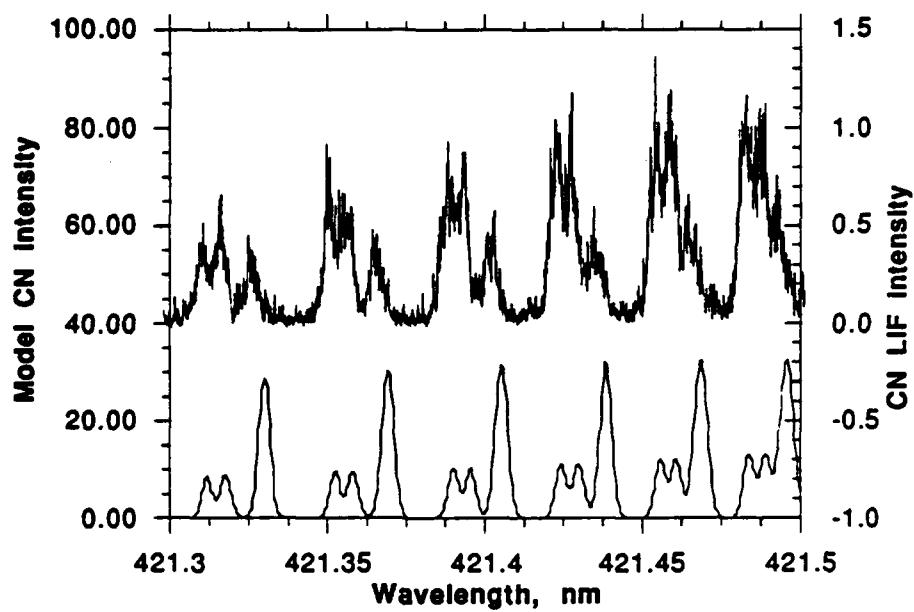
Figure 13. Comparison of model and experimental CN spectra #2.
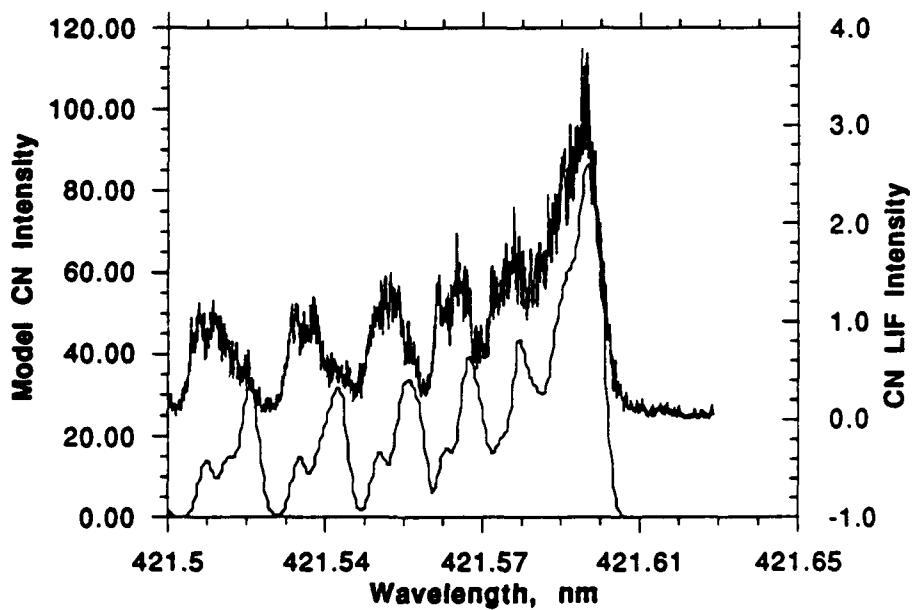
Figure 14. Comparison of model and experimental CN spectra #3.
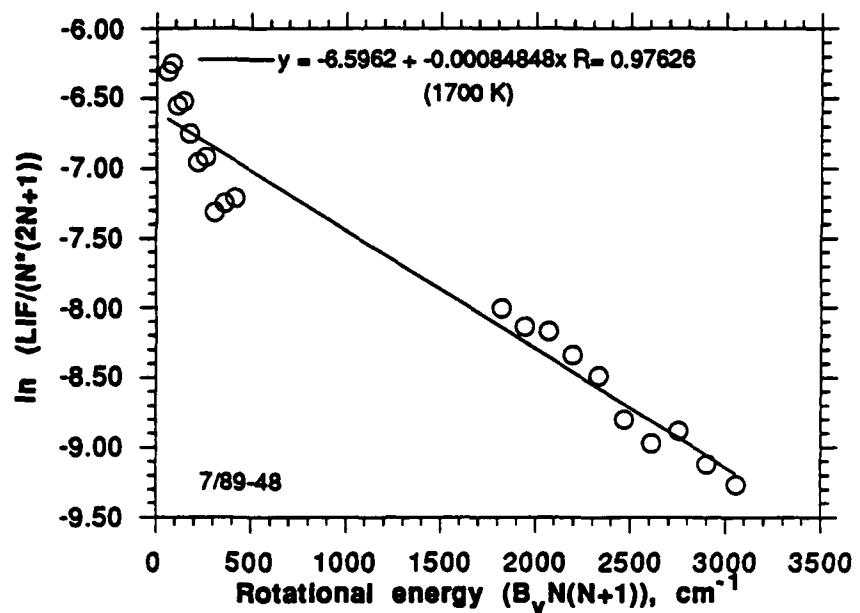
Figure 15. Boltzmann plot #1 unsaturated–high power (0.6mJ/pulse in flame (est.)).
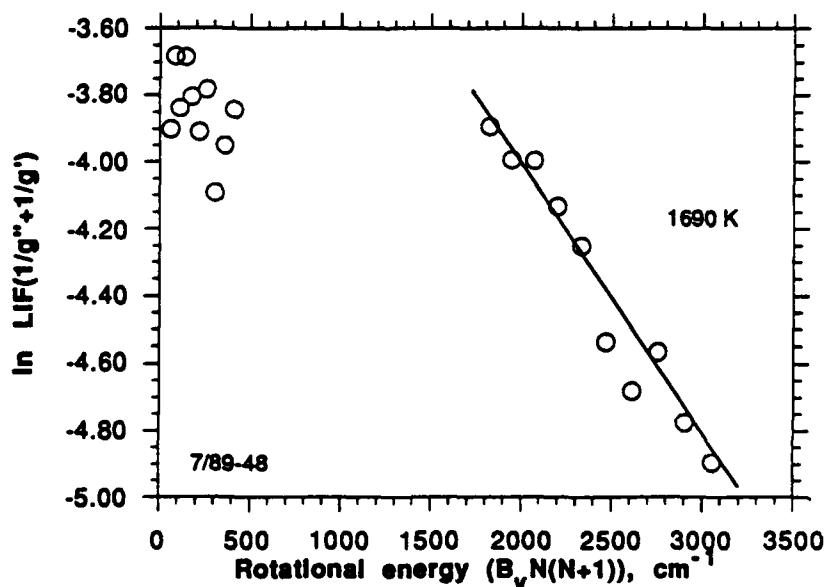
Figure 16. Boltzmann plot #2 saturated-high power. A fit through all points gives a temperature of 5230 K.

18
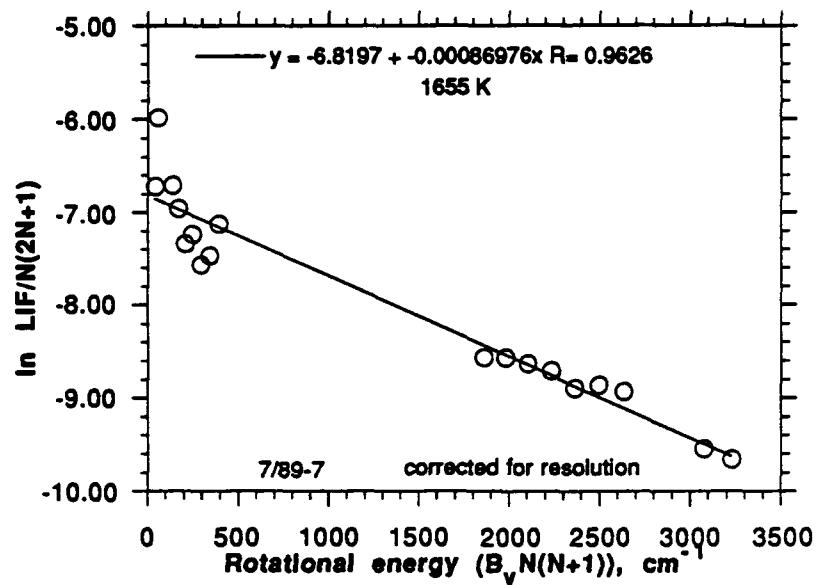
Figure 17. **Boltzmann plot #3 unsaturated-low power** (0.26 mJ/pulse in flame). S1=100 μm, S4=500 μm, 0.22 nm bandpass detection.
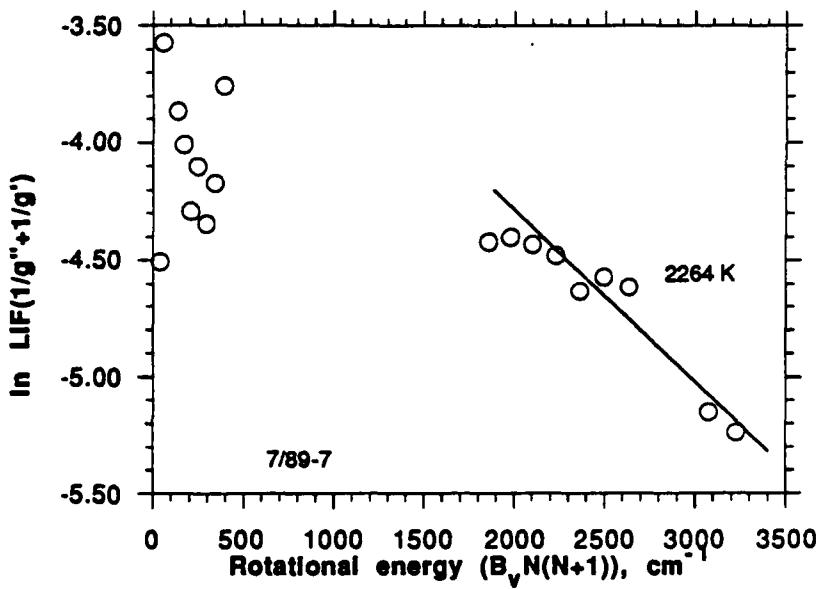
Figure 18. **Boltzmann plot #4 saturated, low power.** A fit through all points gives a temperature of 4955 K.
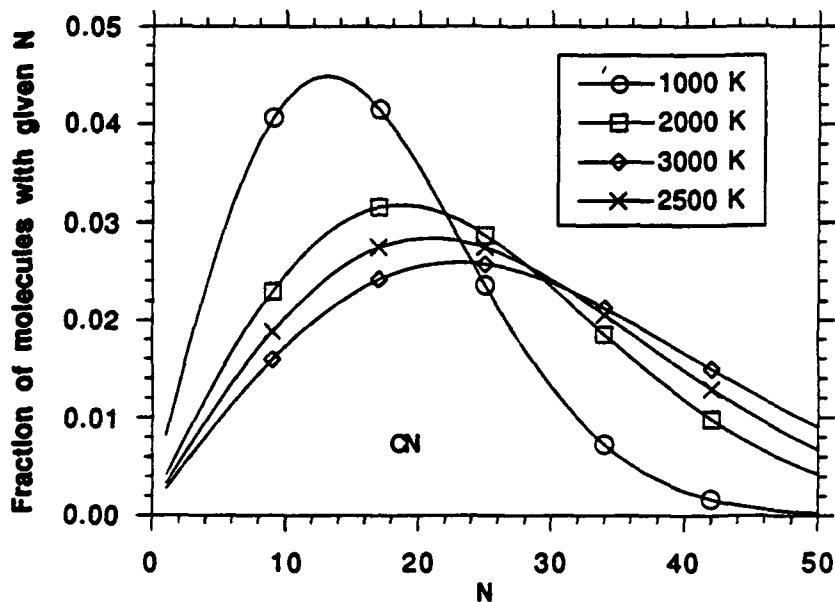
Figure 19. CN rotational level population as a function of temperature. The equation used is $f_j=(hcB_v(2N+1)/kT)exp(-hcB_vN(N+1)/kT)$ [9]. Maximum is found by solving $2-\{(2N+1)^2(hcB_v/kT)\}=0$ for given T.
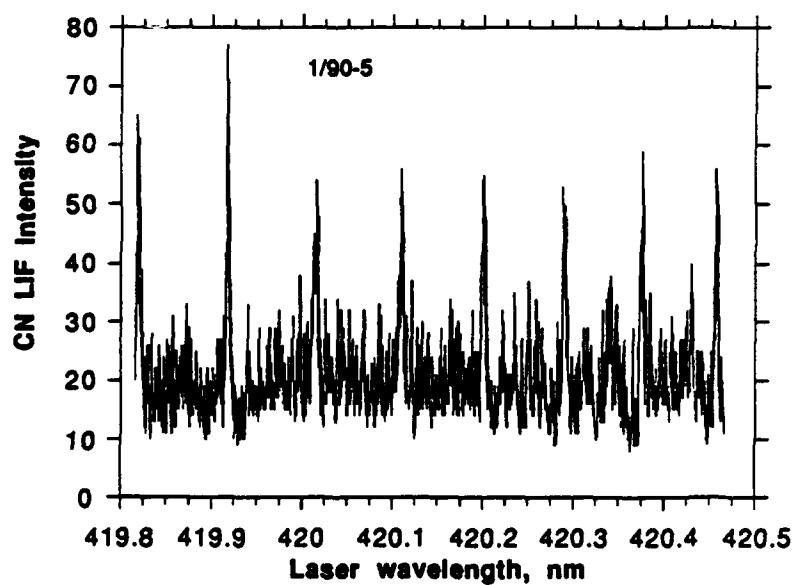
Figure 20. CN 1,0 LIF excitation scan. Laser power varied from 0.04 mJ/pulse at 420 nm to 0.27 mJ/pulse at 421.9 nm, S1=200 μm X 0.2 cm, S4=400 μm (0.18 nm detection bandpass).

20
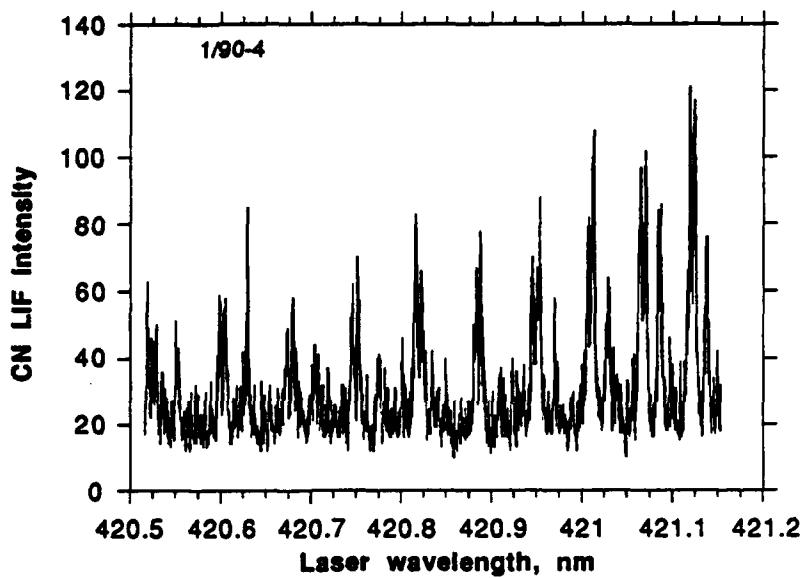
Figure 21. Same conditions as **Figure 20.** A third scan (in addition to Figures 20 and 21) looks essentially identical to Figure 8 and is not shown.
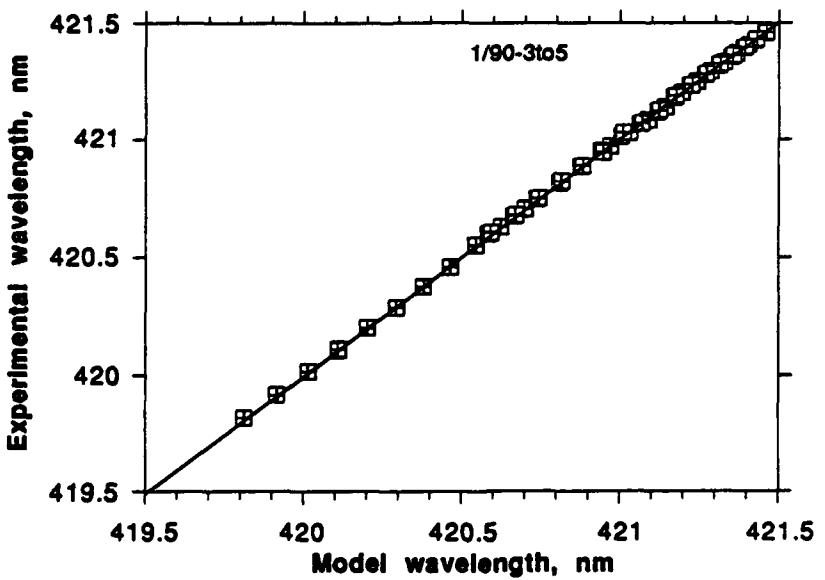
Figure 22. Comparison of calculated and experimental CN 0,1 band line locations (for experiment of Figures 20 and 21).
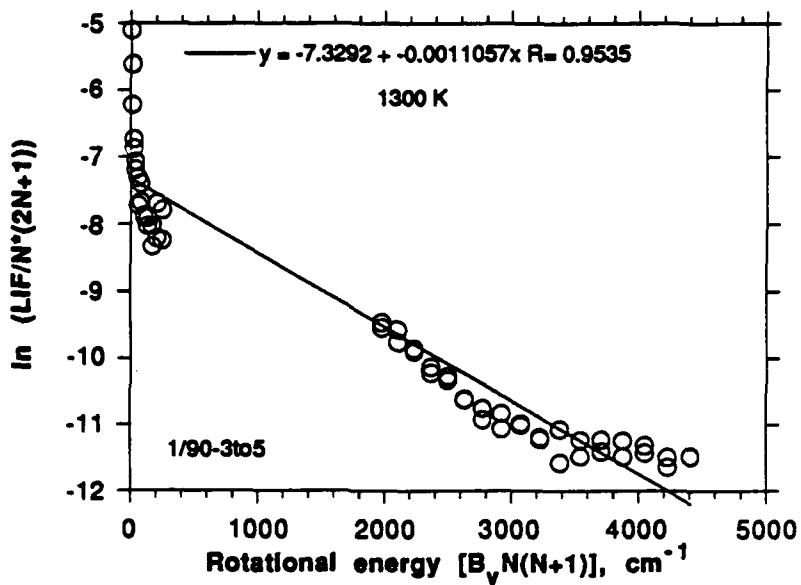
Figure 23. Boltzmann plot for excitation scans of Figures 20 and 21.
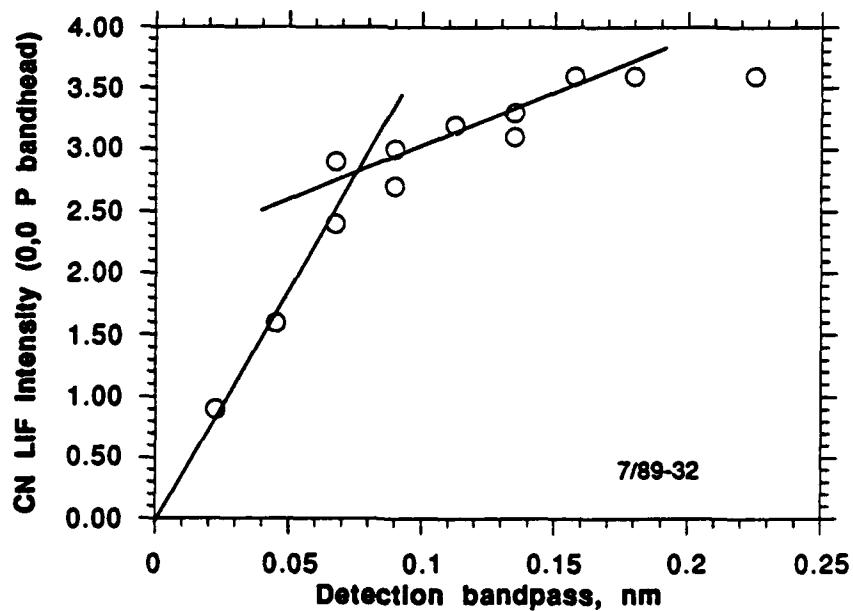
Figure 24. CN LIF intensity as a function of bandpass. A possible explanation for this behavior: First linear region represents P branch bandhead, second linear region represents slower inclusion of CN rotational lines with increasing bandpass. Similar behavior seen in emission, although second linear region extends out to larger detection bandpasses because of the larger P bandhead in emission (wider rotational distribution).

22

C$_2$ LIF MEASUREMENTS

During the initial stages of attempting NO LIF at about 255 nm, C$_2$ LIF experiments were attempted at about 510 nm. Coumarin 334 dye was used with a nominal dye laser output of 506-537 nm. It was not too difficult to obtain C$_2$ LIF in the reaction zone of a CH$_4$/N$_2$O (about 1:2) flame, and even stronger C$_2$ LIF signals were seen in a similar C$_3$H$_8$/N$_2$O flame. Initially, R and P branch transitions from 512 to 514.5 nm were excited and the LIF observed in the 0,0 bandhead at 516.5 nm. This is illustrated in Figures 25-31 for the C$_3$H$_8$/N$_2$O flame and Figure 32 for the CH$_4$/N$_2$O flame. By comparing Figures 29 and 32, the lower C$_2$ LIF signal (concentration) in the CH$_4$ flame can be seen. The goal in this work was to obtain species profiles in propellant flames. An excite 0,0-observe 0,0 LIF scheme will not work in propellant flames (too hard to discriminate between large scattering at laser wavelength and desired LIF signal), so one possibility is excite 0,0-observe 0,1 scheme (the reverse of the propellant CN LIF experiments, which were excite 0,1-observe 0,0). A part of the C$_2$ 0,1 LIF spectrum from 0,0 excitation is shown in Figure 33. An excitation scan is shown in Figures 34 and 35 for 0,1 detection. Note the significantly lower signal due to the lower transition probability for 0,1 vs 0,0 LIF. Detecting the LIF in the 0,1 bandhead does allow the excitation of the 0,0 bandhead, as shown in Figure 35. For comparison purposes, the C$_2$ emission spectrum in a CH$_4$/N$_2$O flame is shown in Figure 36.

C$_2$ has a small rotational constant (B$_V$"=1.7495 cm^{-1}) so many rotational levels are populated. The R branch consists of triplets and the P branch of doublets, with the splitting decreasing with increasing J. The rotational level with the maximum population is shown in Figure 37 as a function of temperature. Also shown in Figure 37 is the rotational level with a population with the minimum temperature dependence. The equations used in these calculations are listed in Table 5. At flame temperatures of 2000-2500 K, the best transition to excite for C$_2$ profile measurements is about J=30. C$_2$ line locations are listed in Table 6 (data from Shea [19]). I also calculated a (rough) rotational temperature from the excitation scans of Figures 26-32. I assumed unsaturated LIF, and found T from plotting ln LIF/S$_J$*g vs the rotational energy (B$_V$J(J+1)). The temperatures ranged from 1300-1600 K, depending upon the assumptions made for calculating the P branch peak heights (the P branch peaks are small and partially (at best) resolved). An example is shown in Figure 38, with the assumption that the P branch peaks are totally resolved. This temperature is rather lower than the expected 2500 K (from OH LIF measurements), but is close to the CN rotational temperature measurements discussed in the previous section. More research would have to be done to get reliable C$_2$ temperature measurements although relative C$_2$ concentration profiles can be obtained with this information. Note that the rotational temperature of the upper state as shown in the emission spectrum is much higher than that of the LIF excitation scan. This is typical behavior for chemiluminescence [20] where emission temperatures of 5000 K are not uncommon for radicals such as CN and C$_2$.

For the propellant experiments, the detection of C$_2$ 0,1 LIF with 0,0 bandhead excitation (516.52 nm) was attempted in a 1 atm AP propellant flame. The AP propellant was chosen because the binder is polybutadiene, and if any propellant flame is going to have C$_2$ in detectable quantities, it should be the AP propellant. However, when the spectrometer slits were closed enough to discriminate between the scattering off the side of the propellant and the

desired C_2 LIF signal, no C_2 LIF signal was seen. This was not unexpected since C_2 was not seen in emission in propellant flames [5], but the effort was worthwhile since C_2 is probably indicative only of binder combustion. The source of other molecules, such as CN, is more ambiguous.

Table 5. General spectroscopic information for C_2 Swan bands [21].

Transition: $A\ ^3\Pi_g$ - $X\ ^3\Pi_u$ [22], $d\ ^3\Pi_g$ - $a\ ^3\Pi_u$ [21], $\Lambda'=\Lambda''=1$

Line strength (Honl-London factors) (S_J) [14]:
$S_J{}^R=(J''+1+\Lambda'')(J''+1-\Lambda'')/(J''+1)$
$S_J{}^P=(J''+\Lambda'')(J''-\Lambda'')/J''$
g (degeneracy)$=2J+1$

Rotational population [18]:
$f_j=(hcB_v/kT)(2J+1)(\exp-[B_vJ(J+1)hc/kT])$
$J*^2+J*-(k/hcB_v)T_{avg}=0$ ($J*$=rotational level with minimum T dependence)
$J_{max}=((2kT/B_vhc)^{0.5}-1)/2$ (J_{max}=rotational level with maximum population)

Table 6. Shea data for C_2 0,0 line locations [19] from 511.5-516.5 nm.

R_1	R_2	R_3	P_1	P_2	J"
					1
					2
	515.6117				3
	515.5024				4
	515.3783				5
515.2972	515.2535				6
515.1531	515.1202				7
515.0175	514.9808	514.9352			8
514.8636	514.8350	514.7952			9
514.7150	514.6837	514.6487			10
514.5507	514.5264	514.4951			11
514.3892	514.3622	514.3362			12
514.2135	514.1923	514.1678			13
514.0411	514.0173	513.9978			14
513.8538	513.8340	513.8139	516.5292	516.5116	15
513.6682	513.6468	513.6294	516.5292	516.5116	16
513.4698	513.4510	513.4342	516.5116	516.4961	17
513.2726	513.2523	513.2386	516.4961	516.4814	18
513.0661	513.0445	513.0295	516.4814	516.4556	19
512.8516	512.8337	512.8189	516.4425	516.4268	20

Table 6 (cont.). Shea data for C_2 0,0 line locations [19] from 511.5-516.5 nm.

R_1	R_2	R_3	P_1	P_2	J"
512.6294	512.6141	512.6005		516.3870	21
512.4079	512.3911	512.3821	516.3606	516.3464	22
512.1732	512.1577	512.1469	516.3096	516.2939	23
511.9416	511.9237	511.9193	516.2563	516.2404	24
511.6935	511.6790	511.6699	516.1878	516.1735	25
511.4500	511.4325	511.4325	516.1219	516.1084	26
			516.0417	516.0282	27
			515.9691	515.9502	28
			515.8695	515.8562	29
			515.7783	515.7652	30
			515.6715	515.6591	31
			515.5678	515.5561	32
			515.4476	515.4357	33
			515.3323	515.3199	34
			515.1974	515.1871	35
			515.0703	515.0589	36
			514.9236	514.9119	37
			514.7847	514.7729	38
			514.6235	514.6121	39
			514.4720	514.4609	40
			514.2976	514.2870	41
			514.1339	514.1234	42
			513.9481	513.9360	43
			513.7719	513.7611	44
			513.5718	513.5610	45
			513.3839	513.3746	46
			513.1722	513.1614	47
			512.9726	512.9621	48
					49
			512.5287	512.5287	50
			512.2868	512.2868	51
			512.0743	512.0674	52
			511.8203	511.8123	53
			511.5900	511.5824	54
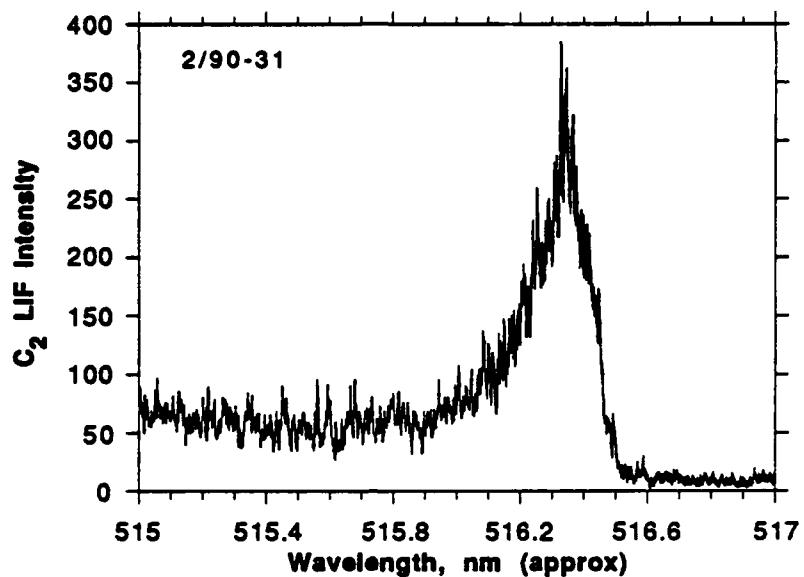
Figure 25. C_2 **LIF spectrum from 0,0 R_1 17 excitation at 513.47 nm.** Detection bandwidth=0.24 nm, slit=600 μm X 2 cm, 3 mJ/pulse @ 10 Hz, 10 pulse avg, 30 ns gate width, 50 mV sensitivity on SR 250. Conditions same for Fig. 26-35 unless otherwise noted.
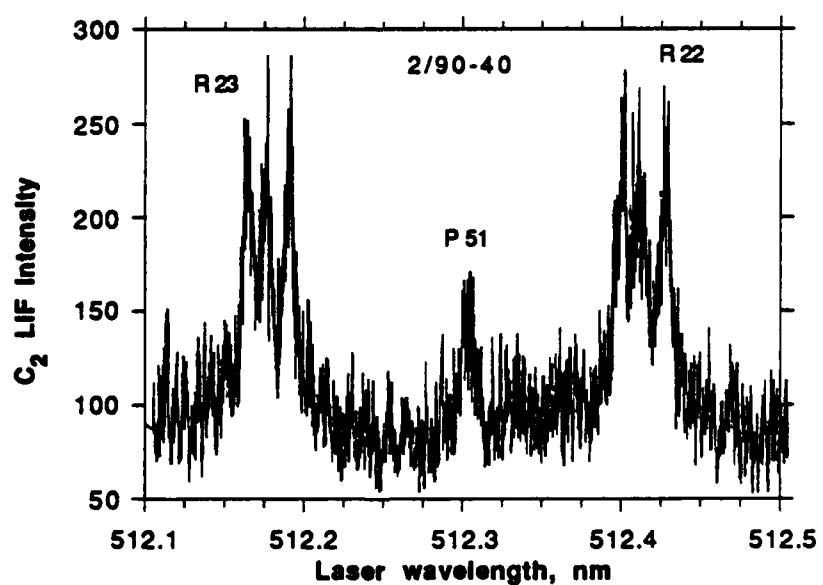
Figure 26. C_2 **LIF excitation scan.** Detection ~516.4±0.12 nm.
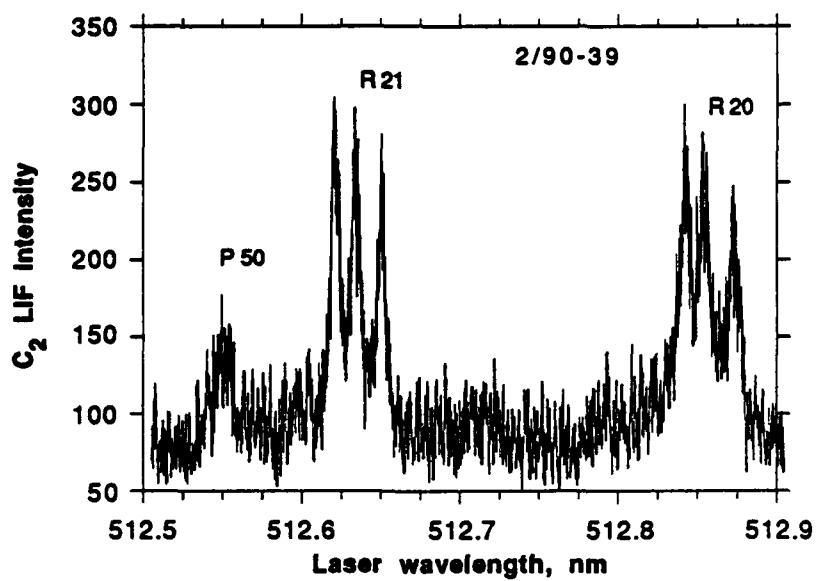
Figure 27. C$_2$ LIF excitation scan.
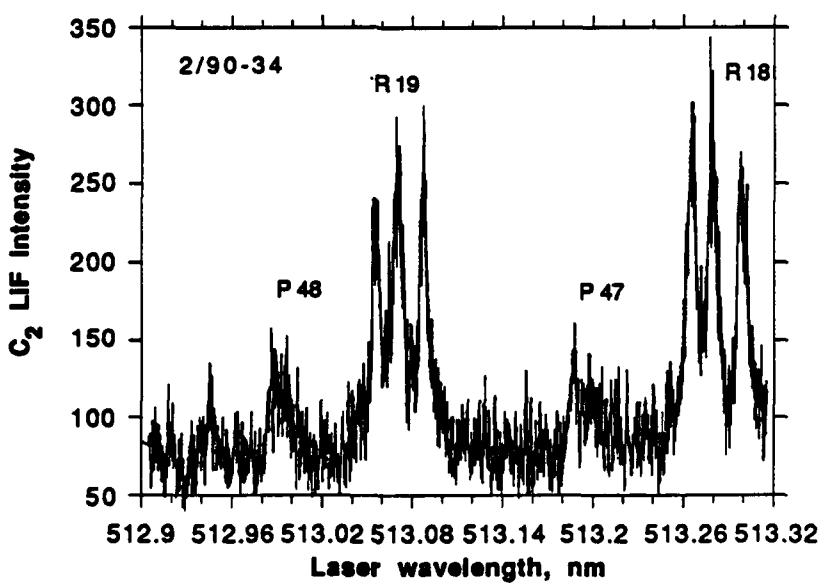
Figure 28. C$_2$ LIF excitation scan.
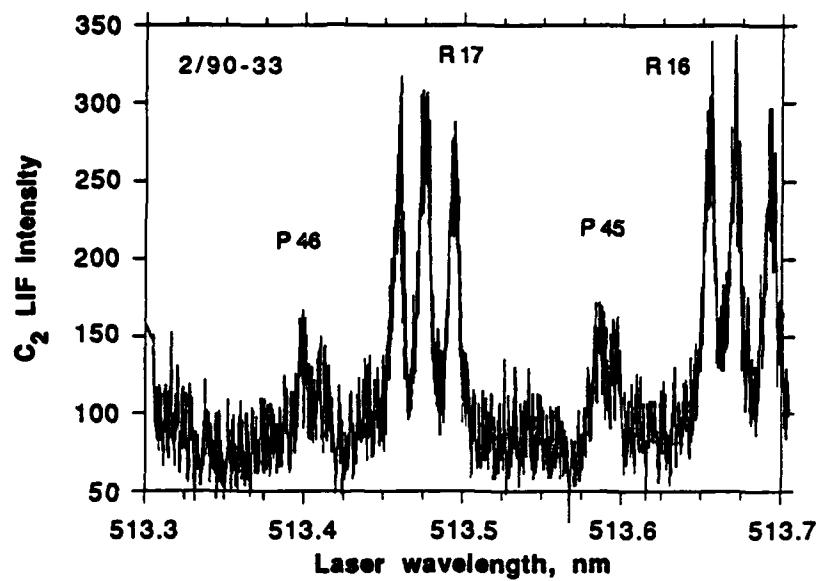
Figure 29. C₂ LIF excitation scan.
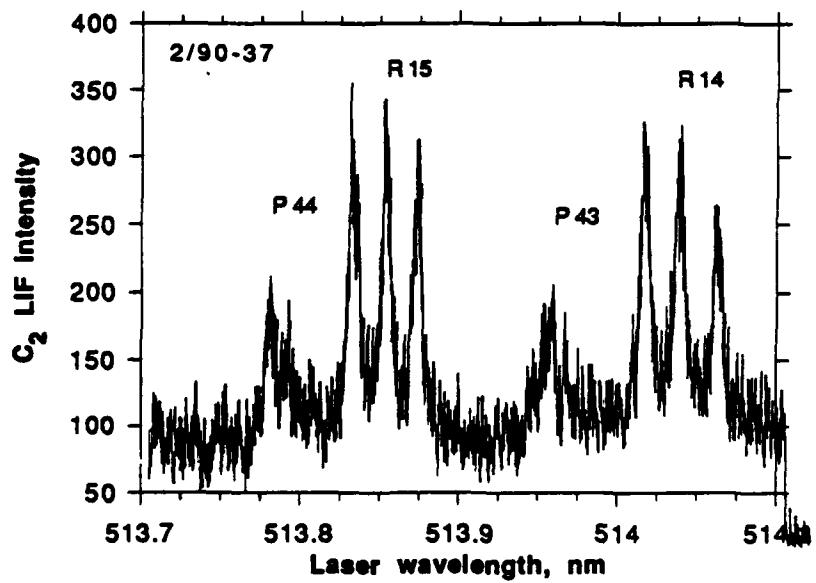
Figure 30. C₂ LIF excitation scan.
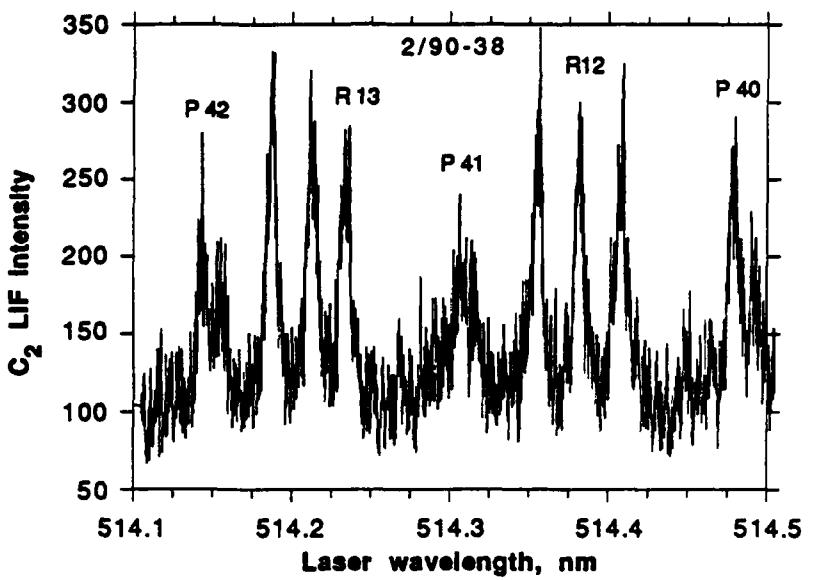
Figure 31. C₂ LIF excitation scan.
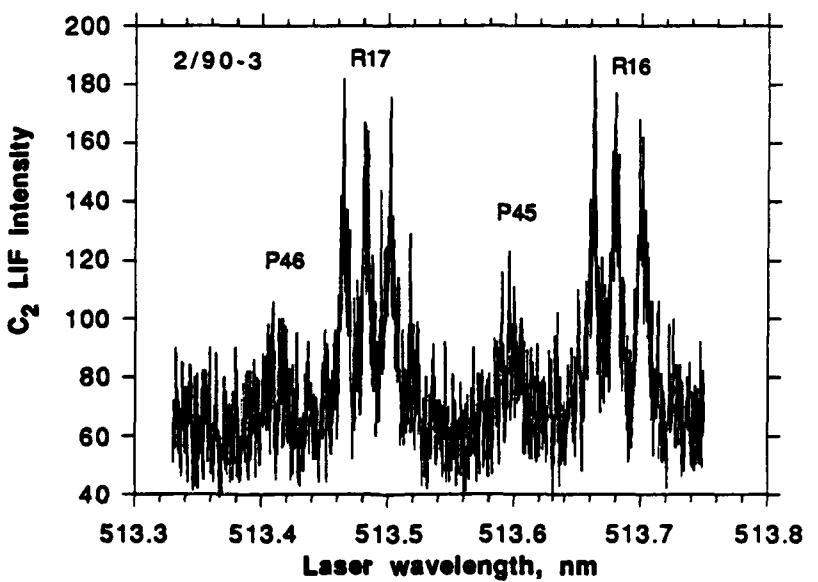
Figure 32. C₂ LIF excitation scan, CH₄/N₂O flame.
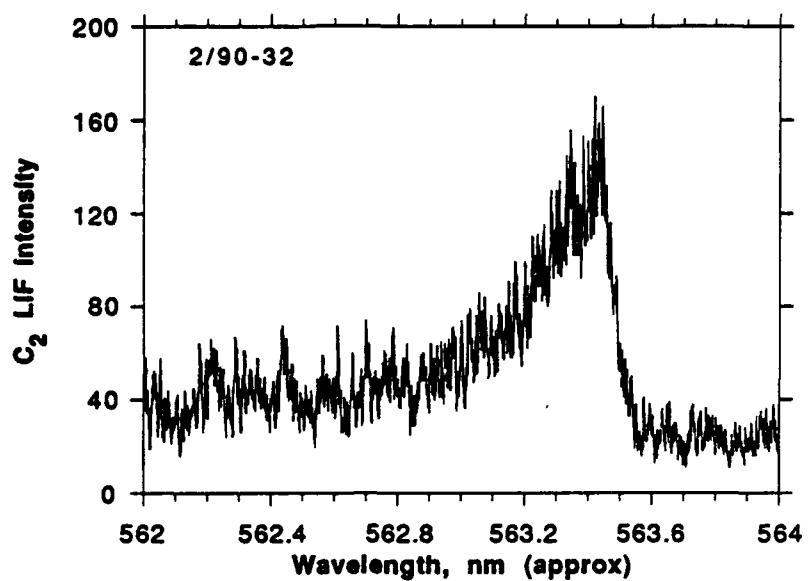
Figure 33. C_2 0,1 LIF spectrum from 0,0 R_1 17 excitation at 513.47 nm, 10 mJ/pulse.
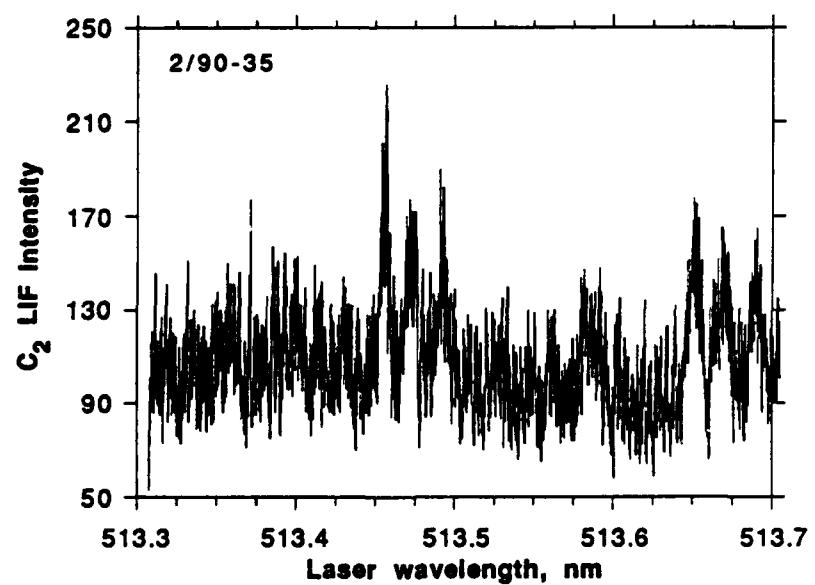
Figure 34. C_2 LIF excitation scan, detection ≈563.4±0.12 nm, 10 mJ/pulse.
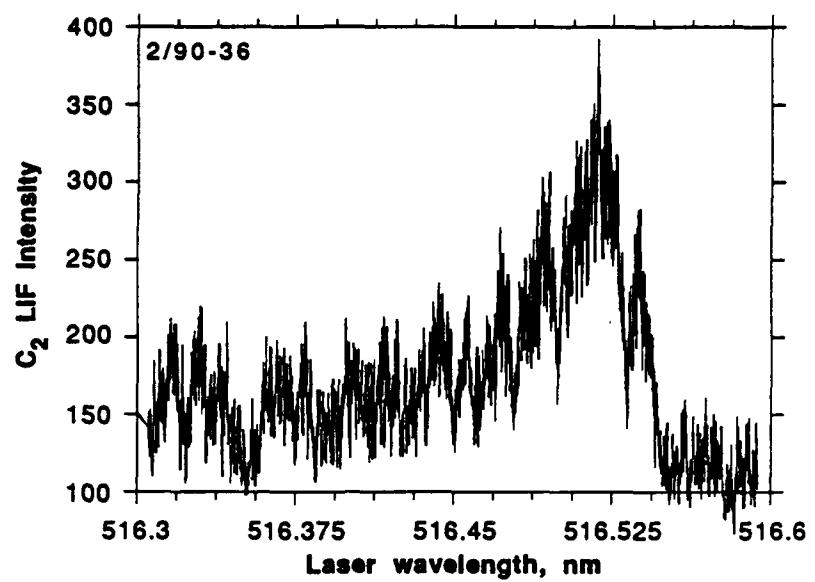
Figure 35. C_2 LIF excitation scan, detection $\approx 563.4 \pm 0.12$ nm, 10 mJ/pulse.
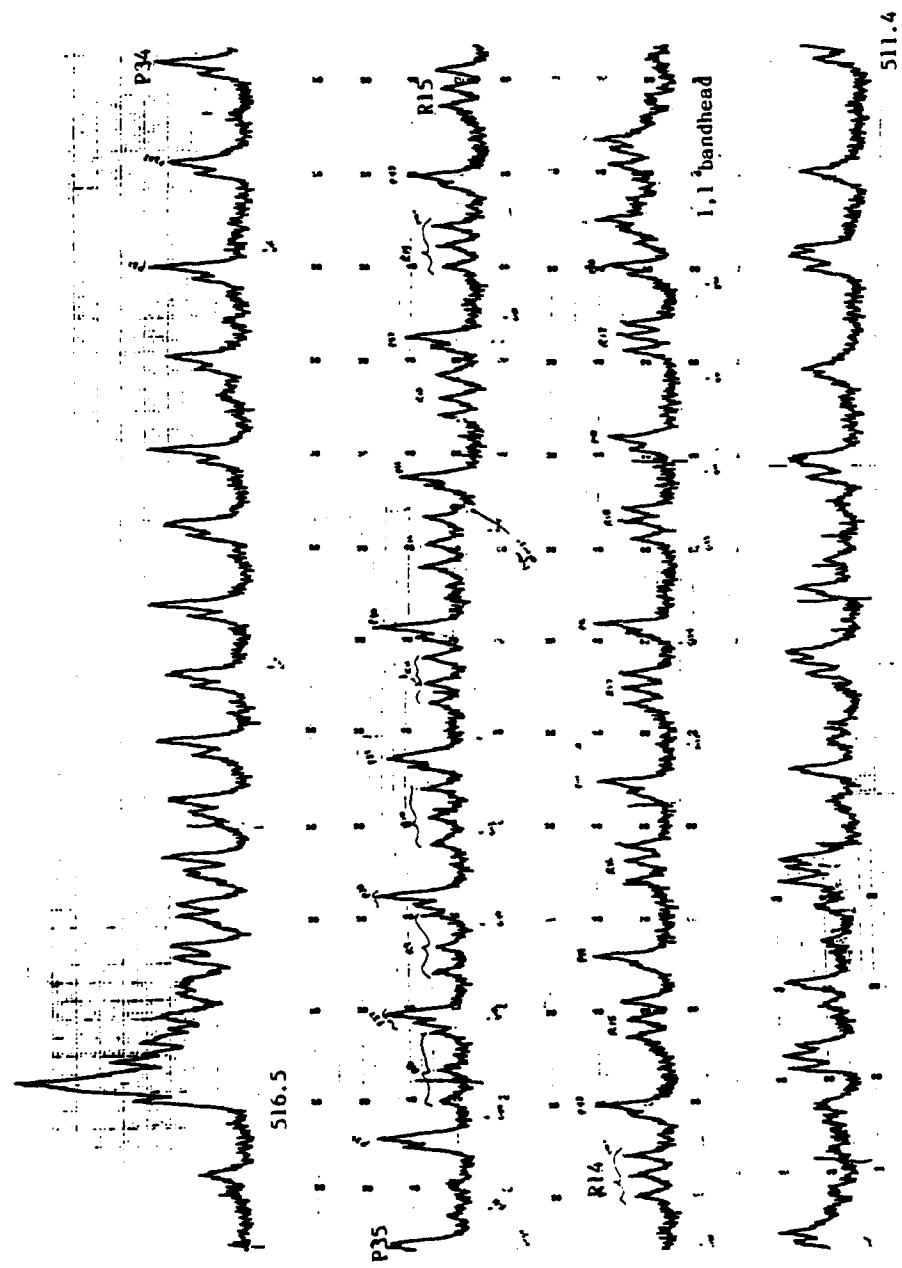
Figure 36. C$_2$ emission spectrum from inner cone of CH$_4$/N$_2$O flame, taken with 0.75 m spectrometer, 2400 gr/mm grating.
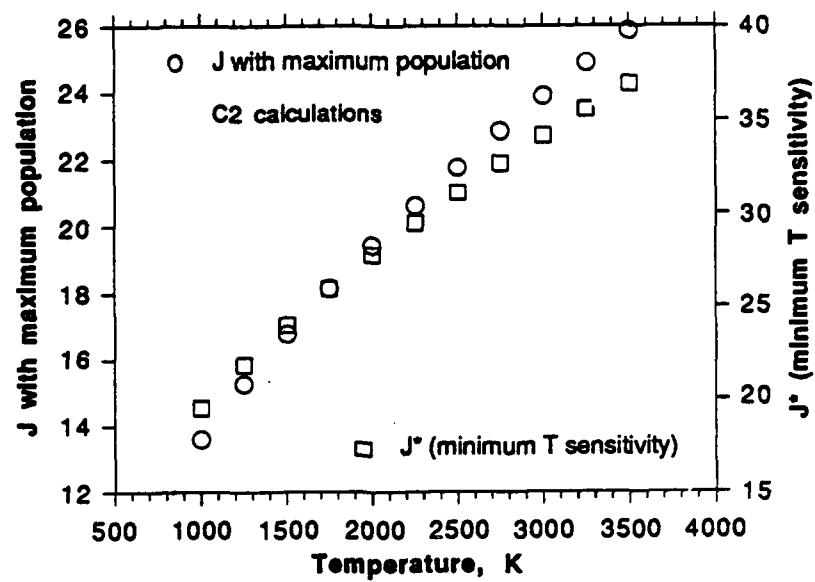
Figure 37. C₂ rotational level calculations.
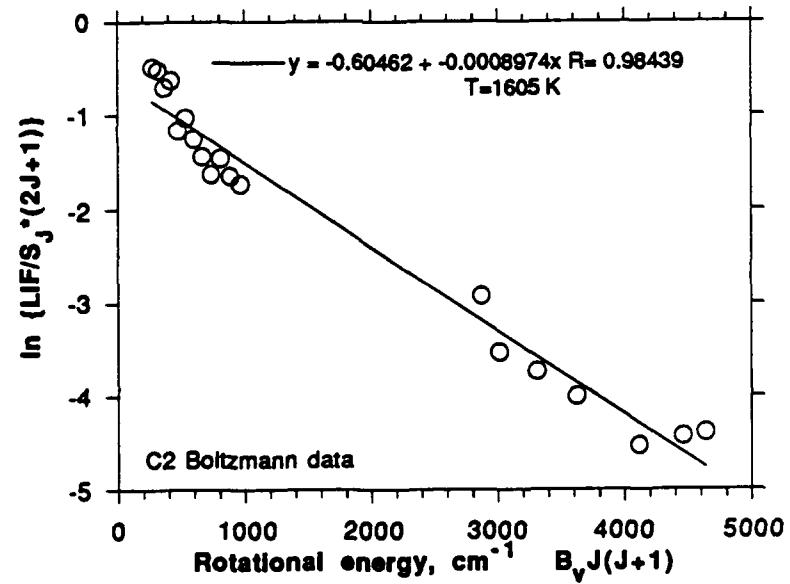
Figure 38. C₂ rotational temperature calculations.

NO LIF MEASUREMENTS

Current SHG crystal limitations in the FL2002 limits UV dye laser output to wavelengths greater than 270 nm. The most likely candidate for NO LIF excitation within this limitation is the NO 0,4 band (Table 7, Figure 39). NO LIF from the NO 0,4 band was observed in a $CH_4/N_2O/NO$ flame, although the LIF signal was relatively weak ($\approx$1000 X weaker than OH 1,1 LIF observed via OH 1,0 excitation). NO LIF was observed in the 0,2 band (246$\pm$2.25 nm) while probing the 0,4 band from 271-272 nm. Detecting NO LIF in the 0,0 band at 226 nm was not very successful, probably due to detector response limitations. An example of the NO LIF spectrum resulting from excitation of a NO 0,4 transition is shown in Figure 41. Examples of NO LIF excitation scans are shown in Figures 42-48. Excitation scan lines were identified by comparison with synthetic spectra created from the equations in Tables 8 and 9. The synthetic spectra were created by scanning a delta function (the laser line) over the NO 0,4 band lines (N=1-80), with the lines approximated as a Gaussian function with a bandwidth (FWHM) of 0.4 cm^{-1} (0.003 nm). A more accurate representation would be to scan a Gaussian laser beam (0.1 cm^{-1} bandwidth) over a Voigt profile (combination of a Gaussian and a Lorentzian profile), but this wasn't necessary for line ID purposes. The experimental NO lines matched well with the calculated lines, as shown in Figure 49. The match would be even better if more care was taken in correcting the FL2002 counter reading. Sample calculated spectra are shown in Figures 50-53. Note the interesting coincidence that the NO γ bands have the same electronic transition as OH ($A^2\Sigma$-$X^2\Pi$). The rotational constants for NO are much smaller than those for OH, so the NO rotational energy levels are much closer together and thus more levels are populated at a given temperature than is the case for OH. The nomenclature for the NO lines is inconsistent, so the lines were labeled by the same criteria as OH. This differed from Reference 26, with R_{12}, Q_{21}, Q_{12}, P_{21}, $P_{12}$, R_{21} [26] = R_{21}, Q_{12}, Q_{21}, P_{12}, O_{12}, S_{21} (this paper). The line intensity in the model spectra was calculated as the product of the line strength (or Honl-London factor, Table 9) and a temperature-dependent Boltzmann factor (exp-$\{hcG(v)/kT\}$).

Once the lines were identified, a Boltzmann plot could be created and an NO rotational temperature could be calculated. The data used in this calculation is given in Tables 8 and 9 and uses identified lines in Figures 45-48 (listed in Table 10). Boltzmann plots are shown in Figure 54 (assuming zero saturation) and in Figure 55 (assuming complete saturation). As can be seen from Figures 54 and 55, the rotational temperature of NO was apparently well below 1000 K, although the data scatter is large. The temperatures would be better fit by assuming partial saturation [11], although the temperatures would still be low.

To improve light rejection for propellant LIF measurements, a Spex 1404 0.85-m double spectrometer (w/ an 1800 gr/mm grating) was used to reproduce the measurements. The maximum bandpass of this spectrometer was measured to be $\approx$1 nm (vs $\approx$4.5 for the 0.5 m/1200 gr/mm grating and $\approx$20 nm for the 0.5 m/300 gr/mm grating). Thus the NO LIF signals were correspondingly lower than those found with the 0.5-m spectrometer, as can be seen by comparing Figure 56 (0.85-m spectrometer) to Figure 44 (0.5 m spectrometer). The NO LIF signals were so small that NO LIF measurements in solid propellant flames were not attempted with this technique.

An OH LIF excitation scan was performed at the same flame location as Figure 18. The results are shown in Figure 57. Note that the 1-nm bandpass contributes to considerable nonlinearity in the Boltzmann plots. Also, the OH signal was so large compared to the NO signal that detector saturation is a possibility. In any case, the OH rotational temperature is substantially higher than the NO rotational temperature. This seems unreasonable, so the low NO rotational temperatures must be considered suspect for now. Zabarnick [11] has observed both NO 0,4 and NO 0,0 in a $CH_4/NO_2/O_2$ flame at 50 torr and found the profiles to be similar, but not identical.

A better scheme might be excite 0,2 - observe 0,1 or 0,0. The relative population of the various levels is shown in Figure 58, demonstrating that the concentration of NO molecules in V"=2 can be significant at higher temperatures, with the corresponding increase in LIF signal. The relative populations in the various vibrational levels can be used to calculate a vibrational temperature in emission, as shown in Figure 59. The Boltzmann plot is not very linear, but the v"=2-4 bands form a linear region with a slope that corresponds to about 5000 K. Information of this type is used to identify the reactions leading to the electronically excited species (see next section). Note that this type of data analysis is not appropriate for Figure 41, where a laser is used to populate v'=0. In this case, the intensity of the emitted bands should be proportional to hvA [18], where v is the frequency of the band and A is the Einstein coefficient of spontaneous emission. In other words, band intensity/vA ~ constant. The data for the bands in Figure 41 is shown in Table 11 and Figure 60. The band intensity/vA is not constant (≈exponential with v" from Figure 60), for reasons that are not clear at this time.

Table 7. Strong NO γ bandheads (O_{12}, P_2) [22]

λ, nm	Intensity	v', v"
300.88, 299.76	4	0, 6
285.95, 284.98	7	0, 5
272.22, 271.32	8	0, 4
259.57, 258.75	9	0, 3
247.87, 247.11	10	0, 2
237.02, 236.33	10	0, 1
226.94, 226.28	8	0, 0
215.49, 214.91	7	1, 0

Table 8. Energy level formulas for NO [26]

$^2\Pi_s$

$T''=G(v'')+F_i(v'',J'')$

$F_{2,1}=B(v'')[(J''+0.5)^2-1\pm0.5(\lambda(v'')^2-4\lambda(v'')+4(J''+0.5)^2)^{0.5}]$

$\lambda(v'')=A(v'')/B(v''); \quad S''=0.5, 1.5$

$G(v'')=1904.405(v''+0.5)-14.187(v''+0.5)^2+0.0240(v''+0.5)^3$

$A(v'')=123.26-0.1906(v''+0.5)-0.0108(v''+0.5)^2$

$B(v'')=1.70427-0.01728(v''+0.5)-0.000037(v''+0.5)^2$

$^2\Sigma^+$

$T'=T_e+G(v')+F_i(v',J')$

$F_1(v',J')=B(v')(J'-0.5)(J'+0.5)$

$F_2(v',J')=B(v')(J'+0.5)(J'+1.5)$

$T_e=43906.37$

$G(v')=2374.307(v'+0.5)-16.106(v'+0.5)^2-0.04645(v'+0.5)^3$

$B(v')=1.99478-0.018328(v'+0.5)$

Table 9. Honl-London (line strength) factors (H) [26]

$\begin{matrix} R_2(+) \\ R_{21}(-) \end{matrix} \qquad \dfrac{(2J''+1)^2\pm(2J''+1)U(4J''^2+4J''+1-2\lambda)}{32(J''+1)}$

$\begin{matrix} R_{12}(-) \\ R_1(+) \end{matrix} \qquad \dfrac{(2J''+1)^2\pm(2J''+1)U(4J''^2+4J''-7+2\lambda)}{32(J''+1)}$

$\begin{matrix} P_2(+) \\ P_{21}(-) \end{matrix} \qquad \dfrac{(2J''+1)^2\pm(2J''+1)U(4J''^2+4J''-7+2\lambda)}{32J''}$

$\begin{matrix} P_{12}(-) \\ P_1(+) \end{matrix} \qquad \dfrac{(2J''+1)^2\pm(2J''+1)U(4J''^2+4J''+1-2\lambda)}{32J''}$

$\begin{matrix} Q_2(+) \\ Q_{21}(-) \end{matrix} \qquad \dfrac{(2J''+1)[(4J''^2+4J''-1)\pm U(8J''^3+12J''^2-2J''+1-2\lambda)]}{32J''(J''+1)}$

$\begin{matrix} Q_{12}(-) \\ Q_1(+) \end{matrix} \qquad \dfrac{(2J''+1)[(4J''^2+4J''-1)\pm U(8J''^3+12J''^2-2J''-7+2\lambda)]}{32J''(J''+1)}$

$U=[\lambda^2(v'')-4\lambda(v'')+(2J''+1)^2]^{-0.5}$, $\lambda(v'')$ as in Table 8

Table 10. NO 0,4 band data (nonresolved lines: R_2 9 + P_2 19 @ 271.425 nm, R_2 7 + Q_2 11 @ 271.588 nm, P_2 12 + R_2 3 @ 271.868 nm)

ID	N	Line Strength	g"	g'	Rot. Ener., F2"	Calc. λ, nm
Q_2 14	·14	4.73620	28	28	428.30560	271.35999
O_{12} 27	27	1.49840	54	52	1347.73999	271.37961
Q_2 13	13	4.32210	26	26	380.56000	271.43869
O_{12} 26	26	1.49740	52	50	1257.34998	271.46921
P_2 18	18	3.45040	36	34	652.15002	271.50470
R_2 8	8	1.02460	16	18	191.16000	271.51041
Q_2 12	12	3.91730	24	24	336.10001	271.51581
P_2 17	17	3.22760	34	32	591.26001	271.57779
O_{12} 24	24	1.48970	48	46	1086.38000	271.63321
P_2 16	16	3.00860	32	30	533.65997	271.64581
Q_2 10	10	3.13750	20	20	257.04999	271.65500
R_2 6	6	0.68760	12	14	138.44000	271.66821
O_{12} 23	23	1.48280 ·	46	44	1005.81000	271.70761
P_2 15	15	2.79350	30	28	479.34000	271.70880
Q_2 9	9	2.76330	18	18	222.46001	271.71710
R_2 5	5	0.52960	10	12	117.02000	271.73959
P_2 14	14	2.58270	28	26	428.31000	271.76682
O_{12} 22	22	1.47350	44	42	928.52002	271.77689
Q_2 8	8	2.40010	16	16	191.16000	271.77429
R_2 4	4	0.37940	8	10 ·	98.89000	271.80600
P_2 13	13	2.37640	26	24	380.56000	271.81970
Q_2 7	7	2.04800	14	14	163.14999	271.82639
O12 21	21	1.46170	42	40	854.51001	271.84119
Q_2 6	6	1.70710	12	12	138.44000	271.87360
O_{12} 20	20	1.44720	40	38	783.78003	271.90030
P_2 11	11	1.97830	22	20	294.92999	271.91061
Q_2 5	5	1.05630	10	10	117.02000	271.91571
P_2 10?	10	1.78710	20	18	257.04999	271.94849
O_{12} 2	2	0.48610	4	2	72.52430	272.10049
O_{12} 15	15	1.35690	30	28	479.33981	272.12000
O_{12} 3	3	0.56680	6	4	84.05980	272.13199
O_{12} 14	14	1.28910	28	26	428.30560	272.14871
O_{12} 4	4	0.65510	8	6	98.89060	272.15869
O_{12} 13	13	1.24860	26	24	380.55820	272.17239
O_{12} 5	5	0.74160	10	8	117.01630	272.18030
O_{12} 12	12	1.20350	24	22	336.09851	272.19101
O_{12} 6	6	0.82370	12	10	138.43629	272.19690
O_{12} 11	11	1.15350	22	20	294.92761	272.20459
O_{12} 7	7	0.90060	14	12	163.14999	272.20850
O_{12} 10	10	1.09840	20	18	257.04639	272.21310
O_{12} 8	8	0.97210	16	14	191.15680	272.21509
O_{12} 9	9	1.03800	18	16	222.45590	272.21661

37
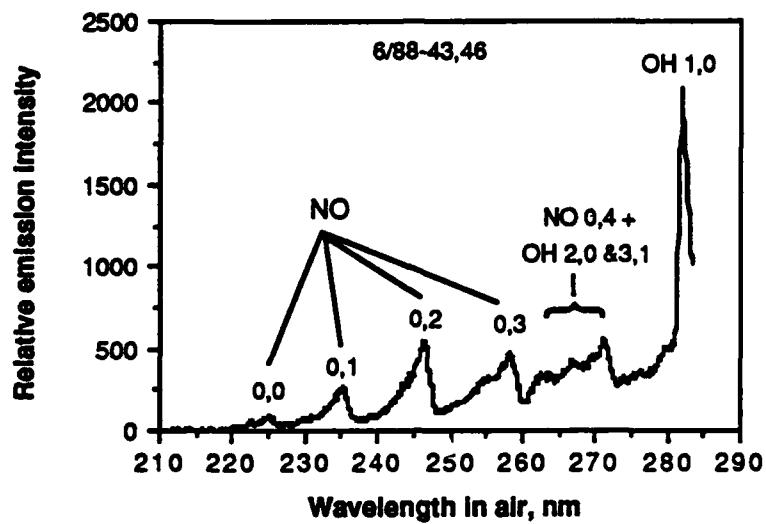
Figure 39. NO emission spectrum. $CH_4/N_2O/NO$ flame, 1 atm air, Reticon detector, 1000 data points (composite of 2 700 pixel spectra), 0.07 nm/pixel dispersion, 500/200 µm slits, 0.5 s exp. time.
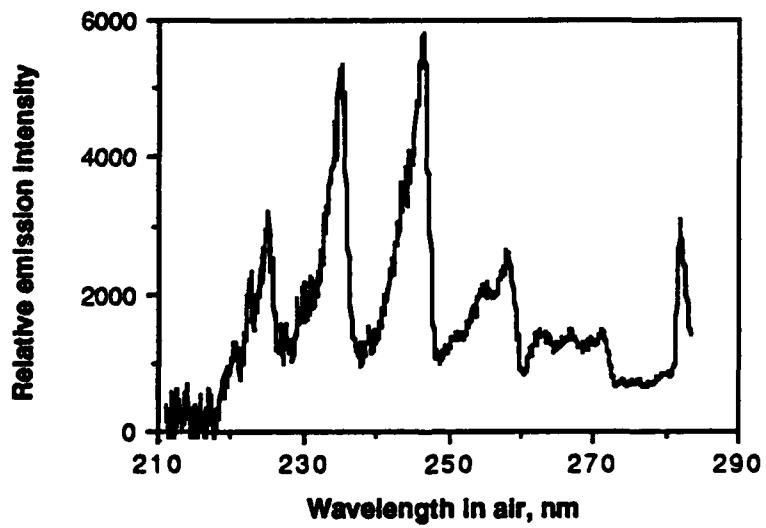
Figure 40. Same as Figure 39, corrected for Reticon wavelength response (Figure 76).

38
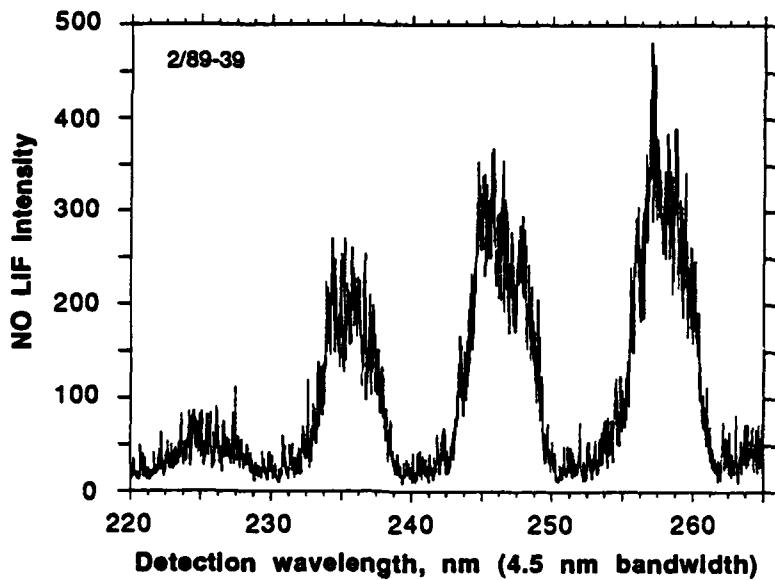
Figure 41. **NO LIF spectrum.** 0.1 mJ/pulse in flame, 271.19 nm excitation, spectrometer scanned at 0.05 nm/s, S1=200 μm, S2=3 mm, 10 ns gate width. S2=rear slit of 0.5 m spectrometer.
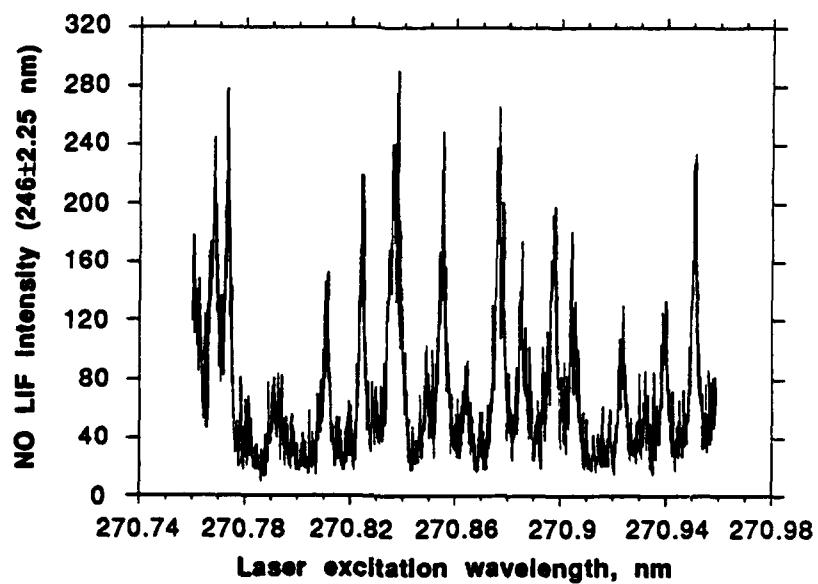
Figure 42. **NO LIF excitation scan.** 0.1 mJ/pulse, 10 ns gate width, 246±2.25 nm detection, S1=200 μm, S2=3 mm. Same conditions in Figures 43-48 except as noted.
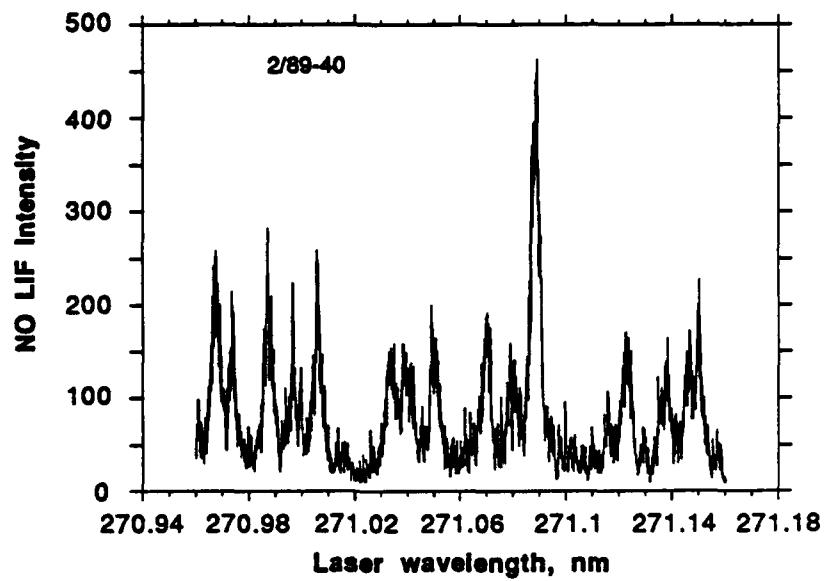
Figure 43. NO LIF excitation scan
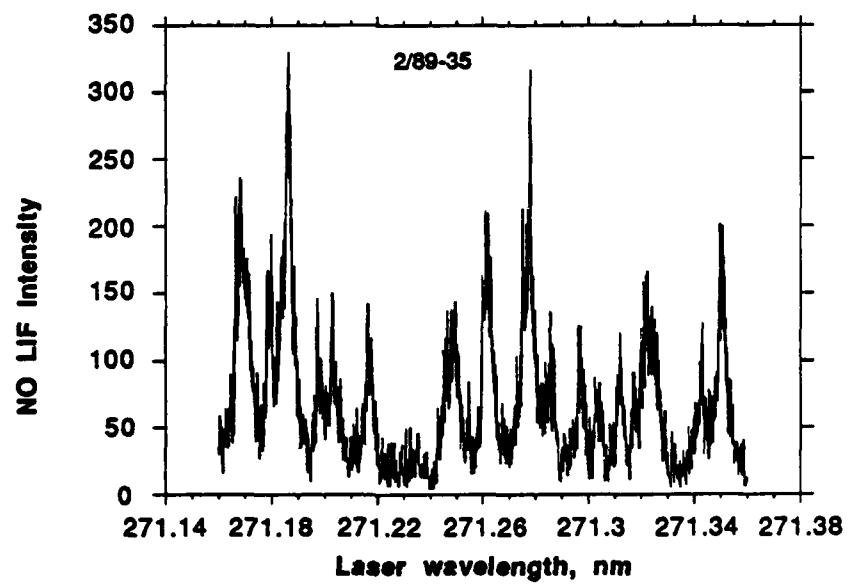
Figure 42. NO LIF excitation scan.
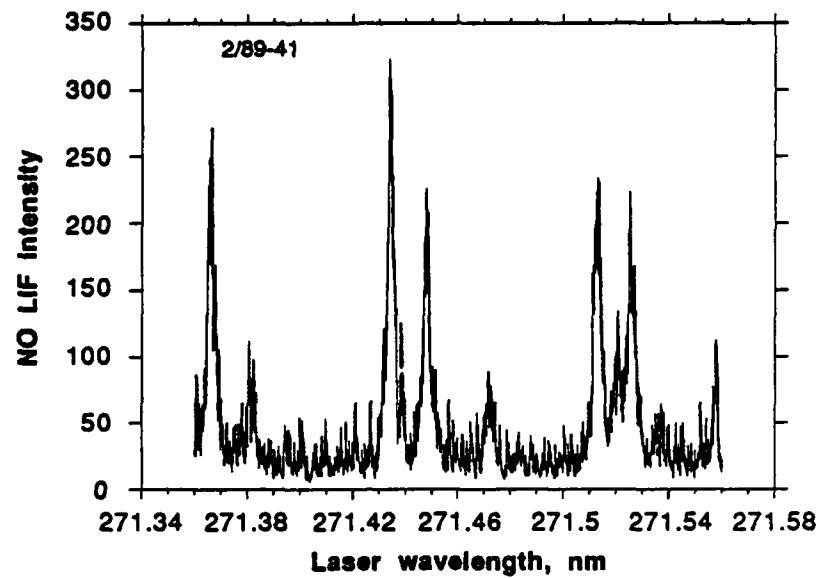
Figure 45. NO LIF excitation scan.
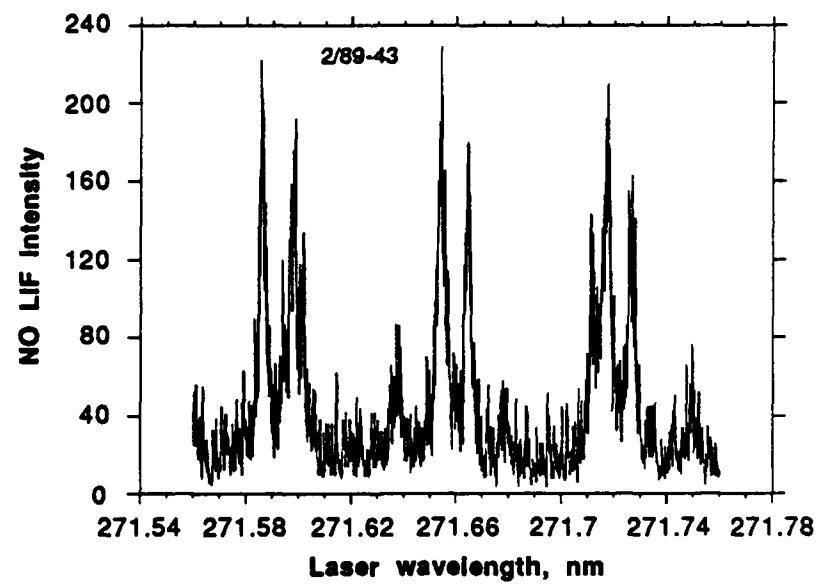
Figure 46. NO LIF excitation scan.

41
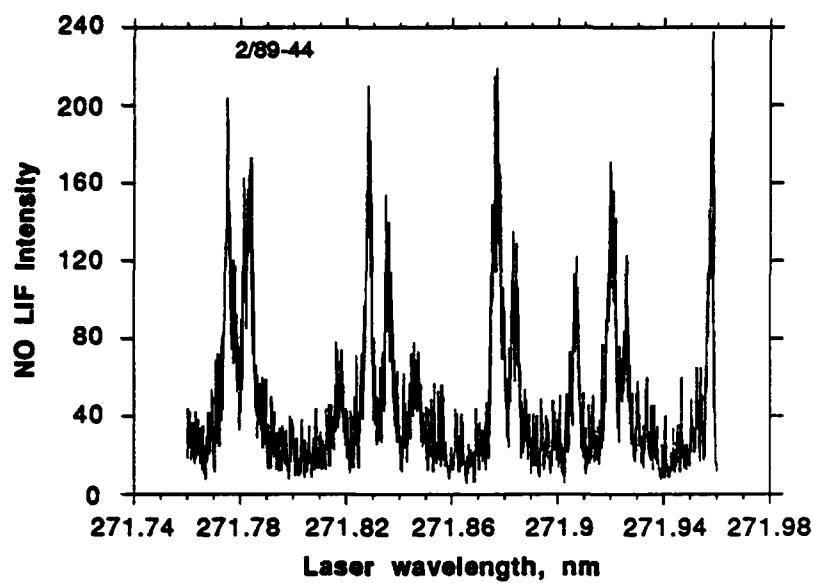
Figure 47. NO LIF excitation scan.
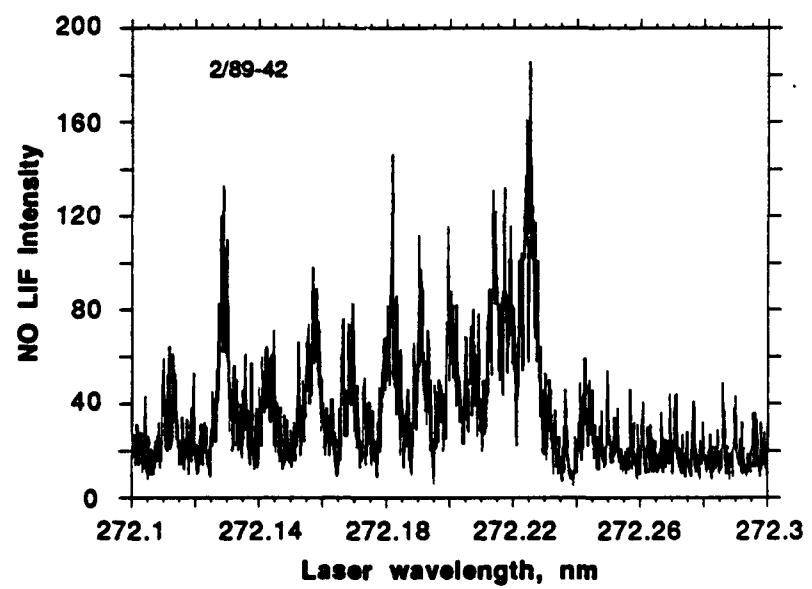
Figure 48. NO LIF excitation scan.

42
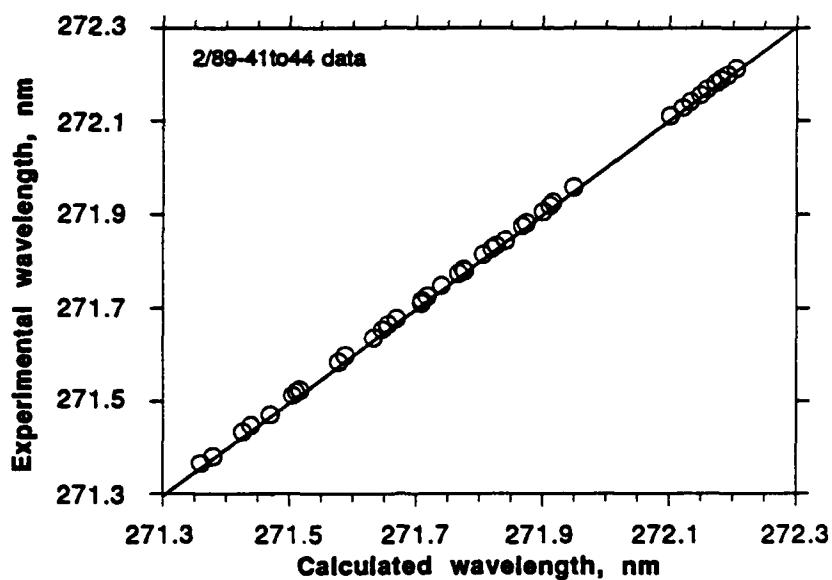
Figure 49. Comparison of experimental and calculated NO line locations.
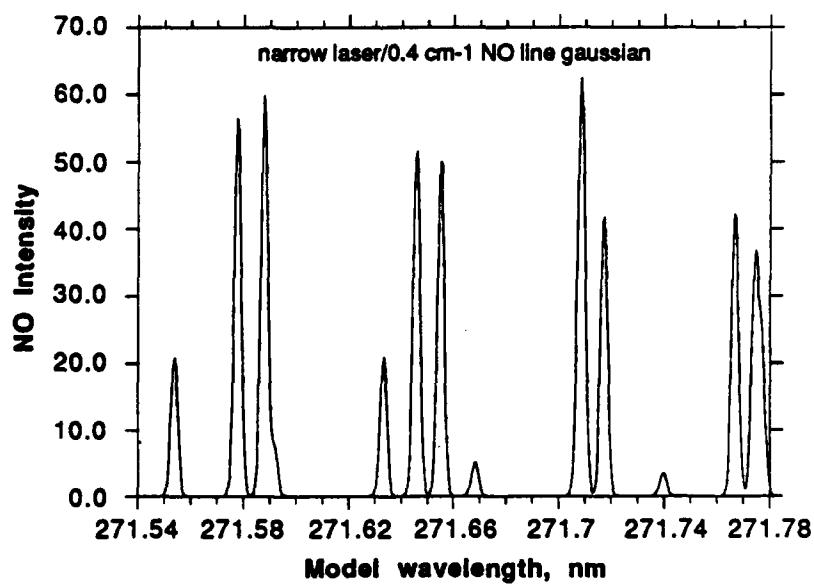
Figure 50. Calculated NO spectrum (compare with Figure 46).
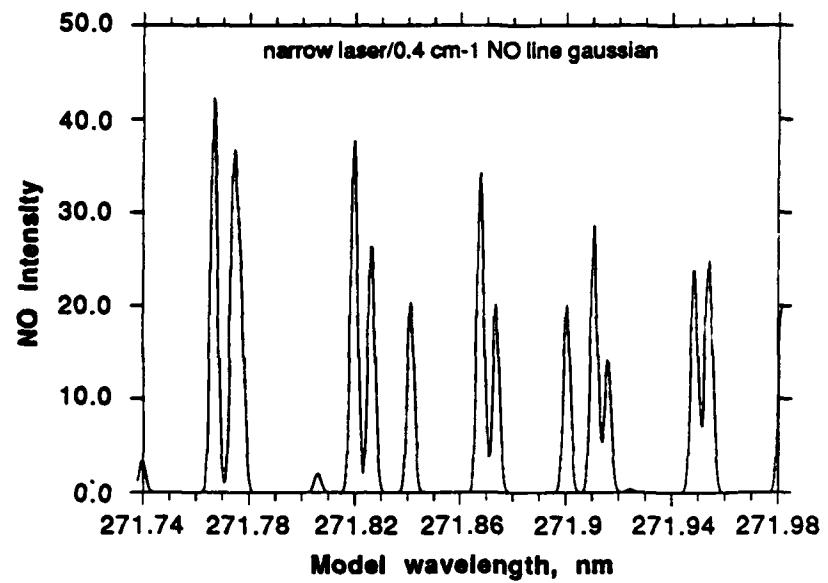
Figure 51. Calculated NO spectrum (compare with Figure 47).
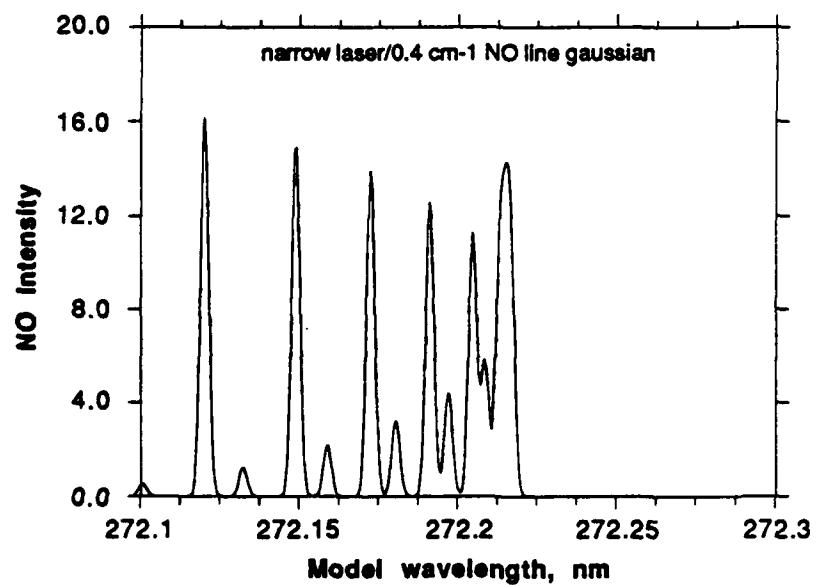
Figure 52. Calculated NO spectrum (compare with Figure 48).
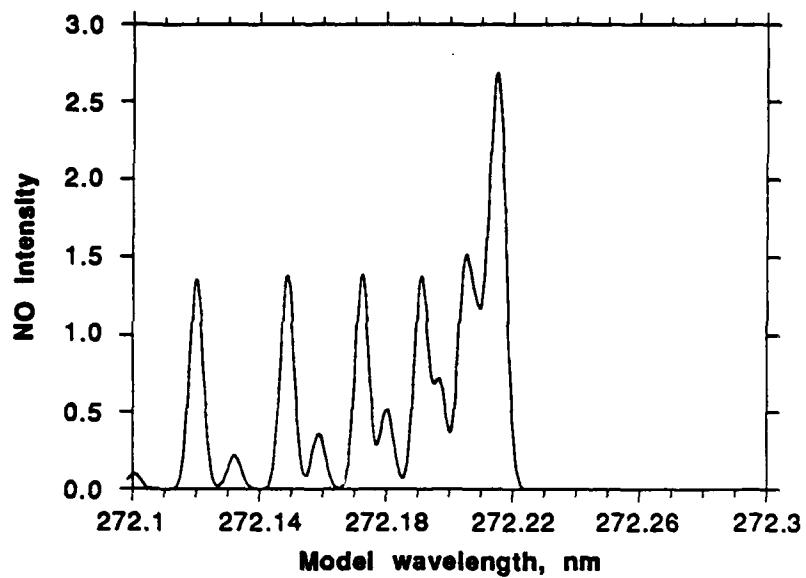
Figure 53. Calculated NO spectrum, same as Figure 52 but T_r=750 K (vs 3000 in Figure 52).
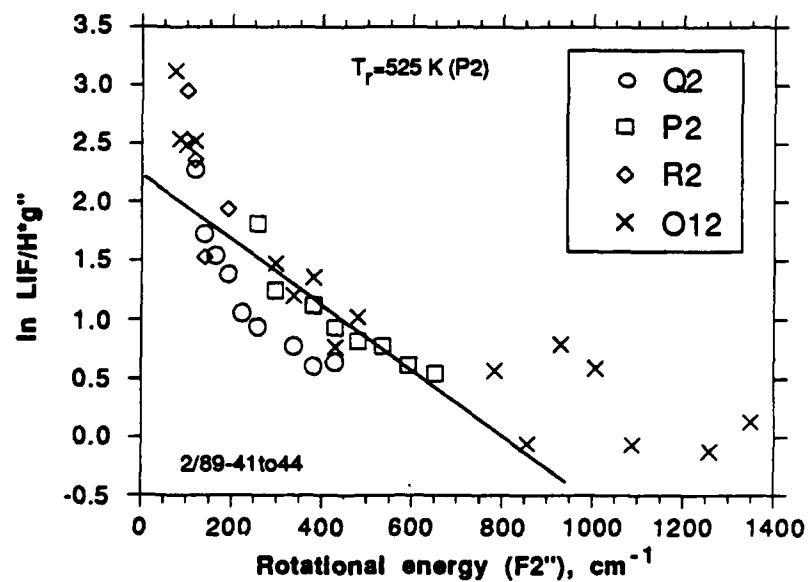
Figure 54. Boltzmann plot for NO lines in Figures 46-49, assuming no saturation. Rotational temperatures: P_2=520 K, O_{12}=680 K

45
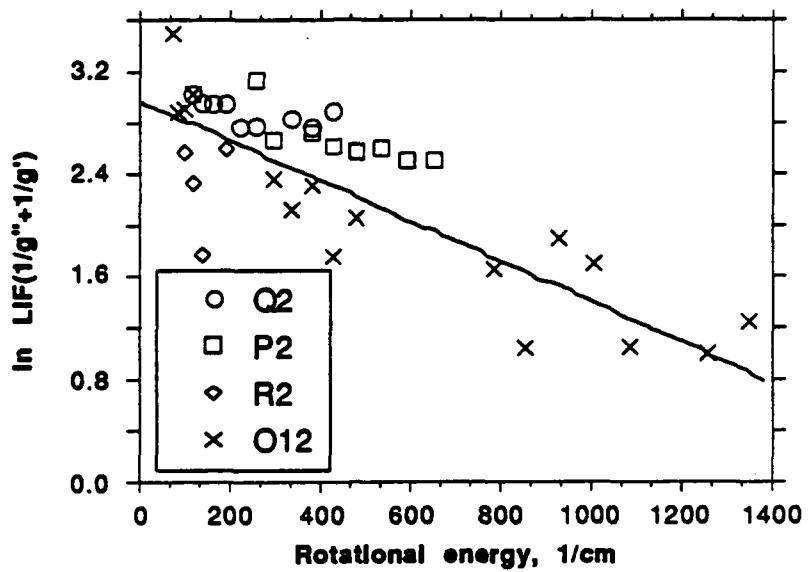
Figure 55. Same as Figure 54, but saturation assumed. Rotational temperatures: P_2=1238 K, O_{12}=916 K.
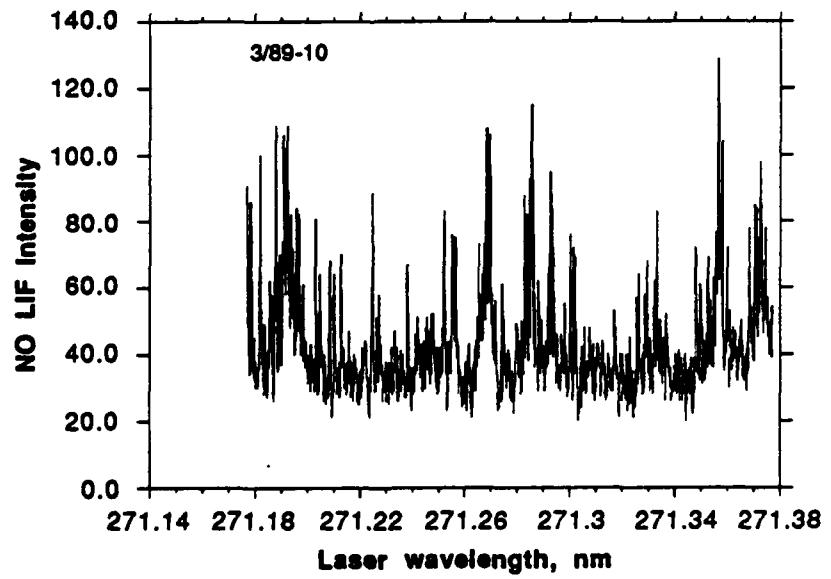
Figure 56. Same as Figure 45, but 0.35 mJ/pulse, S1=400 μm, and 0.85 m spectrometer (1 nm bandpass).
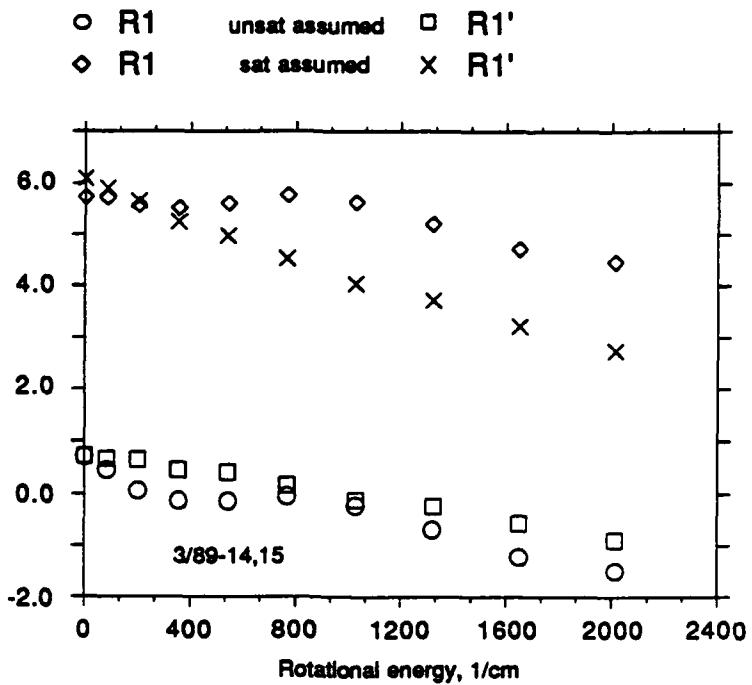
Figure 57. OH LIF excitation scan results from same flame position as Figures 54 and 55. Same conditions, except 0.15 mJ/pulse, 314.8±0.5 nm detection). Rotational temperatures: R_1=1515 K, R_1'=1785 K (unsat); R_1=2505 K, R_1'=865 K (sat).
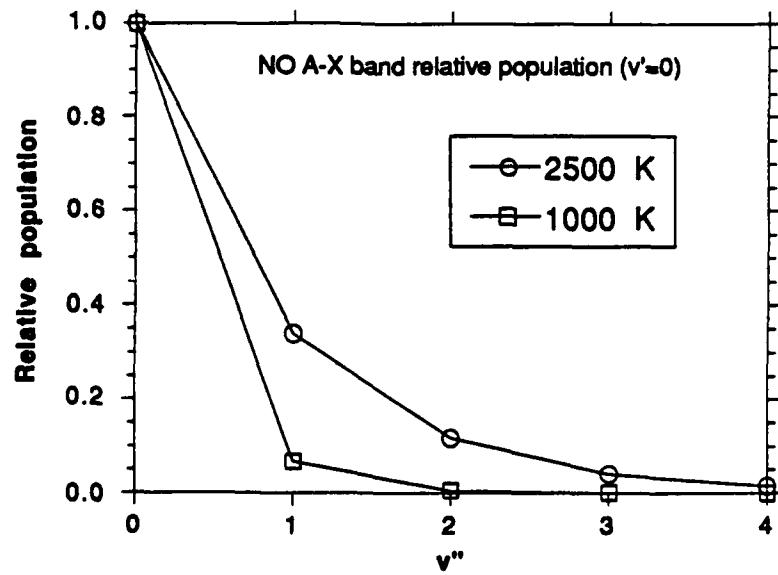
Figure 58. Boltzmann distribution of vibrational population for NO.

47
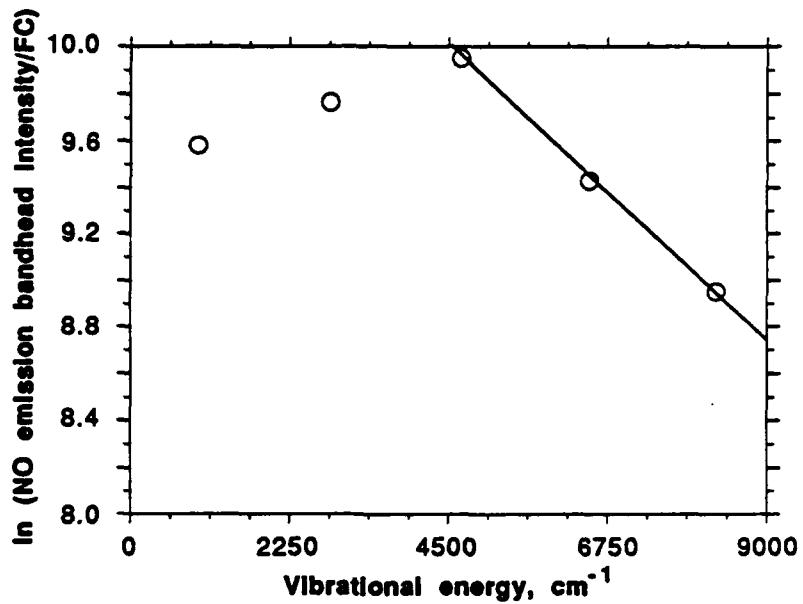
Figure 59. Vibrational Boltzmann plot of vibrational band intensities in emission from Figure 40. The line through the last three points gives a temperature of 5000 K. FC = Franck-Condon factor.

Table 11. LIF calculations for Figure 42. A=Einstein coefficient, ν=frequency of bandhead.

	v"=0	v"=1	v"=2	v"=3
LIF intensity	40	180	280	315
detector sens	2.2	3.0	3.3	3.5
ν, cm^{-1}	44050	42190	40320	38460
A (rel) [37]	1.000	1.372	1.121	0.713
LIF/ν*A (rel)	1.00	2.51	4.55	7.95
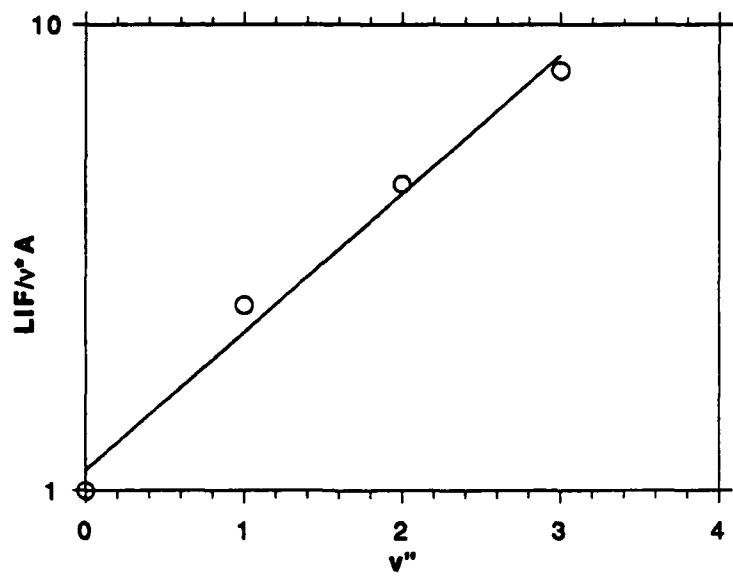
Figure 60. Relationship of LIF intensity and vibrational level in Figure 42.

HYDRAZINE DIFFUSION FLAME EXPERIMENTS

INTRODUCTION

An ongoing project in the Combustion Research Laboratory involves the development of a low pressure hydrazine burner for the study of hydrazine combustion phenomena. There are several aspects of hydrazine flames of interest. The characteristics of the emission or chemiluminescence from low pressure hydrazine flames (especially the UV emission) is of interest for plume detection and tracking. An improved understanding of the physics and chemistry of hydrazine/nitrogen dioxide diffusion flames is also of interest, with the goal of improving the performance of storable liquid propellant systems. For these reasons, a combined theoretical/experimental project was undertaken to study hydrazine combustion.

This section summarizes some of the experimental progress to date. Jeff Amfahr constructed the hydrazine burner and its associated feed systems for fuels and oxidizers and tested the burner. He also constructed the optical collection system for performing emission spectroscopy measurements, and he wrote the computerized data collection program for the detector controller. This section summarizes results the author collected with the hydrazine burner. The results involve emission spectroscopy of low pressure CH_4/O_2, $CH_4/O_2/NO_2$, and $CH_4/O_2/N_2H_4$ diffusion flames. Improvements in the hydrazine feed system SSgt Tracy Christensen suggested are also discussed.

The UV and visible emission in plumes is due to electronic transitions between chemically produced excited states of molecules and the ground states. The species producing this emission or chemiluminescence are known, although the reactions producing the excited state species and the rates of those reactions are much less well known. One reason for this is that the reaction pathways producing the emission are often not the major pathways for the production or consumption of the species in question. Thus, the chemiluminescent reactions may not be that important in the overall combustion behavior of the system, and thus need not be understood for predicting the combustion performance, for example. The chemiluminescent emission from flames has been studied fairly extensively [27,28], and results will be cited as appropriate. The emission from the plumes of hydrazine fueled rockets has also been studied [33]. In Reference 33, the low pressure plume from a monomethylhydrazine/NO_2 rocket was studied, with CO, NO, OH, NH, and CN emission identified. The resolution was insufficient to determine rotational temperatures, however. The present work has sufficient resolution to calculate rotational temperatures.

EQUIPMENT AND PROCEDURES

The hydrazine burner is a concentric annular (Burke-Schumann) diffusion flame. Hydrazine is hypergolic with oxidizers such as NO_2, so only diffusion flames can be studied. The burner is illustrated in Figure 61, the fuel/oxidizer feed system in Figure 62, and the overall system in Figure 63. Emission spectroscopy is a line-of-sight measurement, with several possible locations for measurements shown in Figure 61 ("Region 1", etc.). For these preliminary measurements, the emission was collected from Region 1, 2 cm above the burner surface. The inner and outer tube diameters of the burner were 1 and 2.2 cm. The flame was generally of the

same shape for fuel/oxidizer flows near stoichiometric or oxidizer rich. Fuel rich flames were unusual, as shown in Figure 61.

The flame is created by igniting a CH_4/O_2 diffusion flame at atmospheric pressure and then evacuating the chamber to the desired pressure, usually about 50 mm Hg absolute pressure. Then, the various other fuels/oxidizers are gradually added to or substituted for the CH_4 and the O_2. Some difficulties were encountered with the use of NO_2 and N_2H_4, which will be discussed in the Results.

The flame emission was collected with approximately 1:1 magnification by a collection lens system and focussed onto the entrance slit to a Spex 1870 Triplemate Spectrometer equipped with a EG&G/PAR 1420 Reticon diode array with 700 active elements (pixels). The emission could be dispersed onto the diode array with either a 600, 1200, or 2400 groove/mm grating (turret-mounted), with resulting dispersions of 0.07, 0.035, and 0.0175 nm/pixel respectively. This system has been extensively used in emission spectroscopic studies of high pressure solid propellant flames [2,5]. For these measurements, the entrance slit of the spectrometer (which defines the spatial resolution of the mission measurements in the flame) was fixed at 500 μm wide by 1 cm high. The flame image is rotated by the collection system, so the collection volume in the diffusion flame is approximately 1 cm wide, 500 μm wide and 1 cm in depth (the depth in a line-of-sight measurement is the depth of the flame).

CH_4/O_2 FLAME RESULTS

The CH_4/O_2 diffusion flame was studied as a baseline. At 1 atm, the flame is very white-orange (sooty), with the only detected emission being that from OH. As the pressure is lowered, the flame gradually begins to assume the conical shape illustrated in Figure 61. The orange disappears completely at pressures below about 200 mm Hg. At 40 mm Hg, the emission from Region 1 in the flame consists only of OH, CH, and C_2 emission. In preliminary measurements in Region 2, it appears that Region 2 is a more diffuse version of Region 1, with the same emission characteristics. The emission from Region 1 is illustrated in Figures 64-69. In the figure captions, the notations following the molecule (such as the $A^2\Sigma$-$X^2\Pi$ following OH) refer to the transition creating the emission, with the chemically excited (upper) state listed first and the ground state following. The pressure dependence of the flame structure is due to the differing pressure dependencies of diffusion and reaction kinetics. Diffusion is inversely proportional to pressure, with the diffusion rate increasing with decreasing pressure. The reaction rate is proportional to the concentration of reactants, and thus the reaction rate is proportional to pressure. Thus, at atmospheric pressure where reaction is fast and diffusion is slow, the fuel is significantly reacted (pyrolyzed) before the fuel and oxidizer can mix through diffusion. Hence, large amounts of soot are formed. At low pressure diffusion is fast, so the fuel and oxidizer can mix before reacting, thus the reaction zone looks like a premixed flame with emission from species such as CH and C_2 seen in the reaction zone of premixed flames [20,27,28]. The emission from Region 1 is proportional to the O_2/CH_4 flow ratio, as shown in Figure 70. This trend is possibly partially due to changes in flame shape and partially due to other factors.

52

CH4/O2/NO2 FLAME RESULTS

In premixed flames, NO_2 is a weaker oxidizer than O_2 [11]. In the low pressure diffusion flame, it was discovered that an CH_4/NO_2 diffusion flame would not burn. When NO_2 was added to CH_4/O_2 flame in large excess, relatively weak emission from CN and NH indicated that a relatively small amount of NO_2 was reacting in the flame. This emission is illustrated in Figures 71-73. No emission was seen in the 220-280 nm region, where NO γ band emission is seen [5]. For NO_2 to react in a low pressure diffusion flame, a hypergolic reaction such as $N_2H_4+NO_2$ is probably required. Problems were encountered with the NO_2 flow controller, but discussions with other lab personnel indicated that these problems were due to the low vapor pressure of NO_2 and could be overcome.

CH4/O2/N2H4 FLAME RESULTS

When an attempt was made to add N_2H_4 to the CH_4/O_2 flame, it was found that the feed system illustrated in Figure 62 was inadequate. The system was designed to supply gaseous N_2H_4 to the burner, but at the conditions of the experiment, the N_2H_4 flowing through the control valve was liquid (~298 K, 45 mm Hg pressure). With liquid flowing through the lines, there was negligible flow control of the hydrazine. What appeared to be happening was that N_2H_4 was entering the chamber as a liquid and forming a pool, where it was then flashing into a gas. As it turned out, this allowed the formation of a relatively stable $CH_4/O_2/N_2H_4$ flame of unknown stoichiometry, illustrated in Figure 74. The problems with the feed system are being studied, with one possible design improvement illustrated in Figure 75. Additional problems with a leaking N_2H_4 valve were also encountered and led to an early termination of the experiments with N_2H_4.

The relatively stable $CH_4/O_2/N_2H_4$ flame was studied with emission spectroscopy over the entire sensitivity range of the Reticon (shown in Figure 76). In addition to the OH, CH, and C_2 emission from the CH_4/O_2 flame, strong CN and NH emission was also seen. The emission from the $CH_4/O_2/N_2H_4$ flame is illustrated in Figures 77-82. No emission was detected from 220-280 nm, although several attempts with varying exposure times and dispersions were made. The signal in Figure 78 at 220 nm is noise amplified by the detector sensitivity correction. The apparent signal at 580-600 nm may be NH_2 emission [22], although it may again be amplified detector noise. The OH, CH, and C_2 emission are essentially unchanged from the CH_4/O_2 flame, so only the CN and NH emission are due to the presence of the N_2H_4. The presence of NH in the ground state is reasonable, with the combustion of N_2H_4 proceeding among several competing paths [29,30]:

$$N_2H_4 \rightarrow NH_2 \rightarrow NH \rightarrow NO \rightarrow N_2 \quad \text{or} \quad N_2H_4 \rightarrow N_2H_i \rightarrow NNH \rightarrow N_2$$

The presence of CN indicates that the two fuels are interacting, since the C comes from the CH_4 and the N from the N_2H_4. From the structure of the flame as shown in Figure 74, it appears that the reactions involving CN are occurring after the CH/C_2 reactions. One possibility is that CH and C_2 from the CH_4/O_2 reaction zone are forming excited state CN and NH through reactions such as those with NO and OH [28]:

$$C_2(a^3\Pi) + NO \rightarrow CN(B^2\Sigma) + CO \qquad\qquad R1$$
$$CH + NO \rightarrow CN(A^2\Pi) + OH \qquad\qquad R2$$
$$CN(A^2\Pi) + OH \rightarrow NH(A^3\Pi) + CO \qquad\qquad R3$$

53
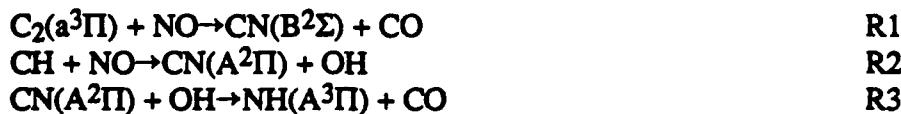
CH₄/N₂O FLAME RESULTS

For comparison, an emission survey was made of a CH_4/N_2O diffusion flame. There is existing emission data taken with the Reticon detection system for a premixed, 1 atm CH_4/N_2O flame [5], showing emission from OH, NH, CN, CH, and C_2 (weak). The premixed flame emission is illustrated in Figure 83 [5]. No NO emission was seen in this flame. NO emission was seen in an NO-seeded CH_4/N_2O flame, as shown in Figures 40 and 41.

The diffusion flame of CH_4/N_2O has slightly different burning characteristics from the CH_4/O_2 diffusion flame. The CH_4/N_2O diffusion flame was unstable below about 50-60 mm Hg pressure, so the emission data was collected at 80 mm Hg pressure. The stoichiometry of the CH_4/N_2O flame is different from that of the CH_4/O_2 flame, with a diffusion flame similar to Figure 61 (left drawing) occurring at flow rates of 0.4/2.5 slpm for CH_4/N_2O. The emission from Region 1 of this flame is illustrated in Figures 84 and 85. Note the similarity between the CN emission shown in Figures 85 and 81. Comparing the CH_4/N_2O premixed and diffusion flames, OH emission is relatively stronger in the premixed flame, while CH and C_2 emission is relatively more intense in the diffusion flame.

ROTATIONAL AND VIBRATIONAL TEMPERATURES

The rotational and vibrational temperatures of the CN, NH, OH, CH, and C_2 can be calculated using relatively standard procedures previously employed in the Combustion Research Laboratory for analysis of solid propellant emission spectra [5]. These temperatures may give some clues as to the reactions producing the electronically excited CN and NH. For this report, the main species of interest are the CN and NH present because of the hydrazine. The rotational/vibrational temperature of experimental spectra can be calculated by comparison with synthetic spectra, an example of which is shown in Figure 86b [5]. In Figure 87, a corrected CN emission spectrum from the $CH_4/O_2/N_2H_4$ diffusion flame is shown. Examples of atmospheric pressure premixed CH_4/N_2O flame CN spectra and high pressure propellant flame CN spectra are shown in Figures 86a and 88. By comparison with synthetic spectra, the CN vibrational and rotational temperatures (assumed to be equal) for 1 atm flames (both CH_4/N_2O and AP propellant) were found to be about 5000 K. The high pressure HMX propellant flame CN spectra yielded vibrational/rotational temperatures of about 2500 K [5].

By comparison with synthetic spectra, the vibrational/rotational temperatures in the $CH_4/O_2/N_2H_4$ diffusion flame were approximately 10500/7000 K at 45 mm Hg pressure (0.06 atm). The synthetic spectrum is shown in Figure 89. It was necessary to choose different rotational and vibrational temperatures to fit the experimental data (Figure 87). These values of rotational and vibrational temperatures for CN($B^2\Sigma$) are very close to those fou ⸱₁ in a study of the $C_2(a^3\Pi) + NO-->CN(B^2\Sigma) + CO$ reaction by Reisler, Mangir, and Wittig [31] and the rotational temperature of CN($B^2\Sigma$) found in C_2H_2/N_2O flames by Guillaume and Van Tiggelen [28] . Thus, the diffusion flame data at low pressures appears to indicate that the CN emission in these flames is due to the C_2+NO reaction, as it was in C_2H_2/N_2O flames [28].

The NH vibrational temperature in the $CH_4/O_2/N_2H_4$ diffusion flame at 45 mm Hg (Figure 79) is about 2750 K, similar to the temperature found in CH_4/N_2O premixed flames at 1 atm and

propellant flames at pressures from 1-35 atm [5]. A sample NH synthetic spectrum is shown in Figure 90, with the vibrational temperature calculated from the ratio of the 0,0 and 1,1 Q branch bandheads.

With the addition of this low pressure diffusion flame data, a database of CN and NH vibrational temperatures now exists over a wide range of pressures. When the CN vibrational temperature is plotted as a function of pressures for these different flames, a strong correlation is seen, as shown in Figure 91. This correlation probably indicates that the reactions forming the excited-state CN (CN*) are similar in all these flames, with the temperature difference due to pressure. What is apparently happening is that the reactions are forming CN* in a highly-vibrationally-excited state. At low pressures with relatively few collisions, this excited state radiates with a temperature similar to that at which it was produced. At high pressures, the CN* is involved in many collisions before radiating, with these collisions tending to "thermalize" or reduce the temperature of the CN* to the flame temperature (the adiabatic flame temperature of all these flames is in the 2500-3000 K range). This seems to also explain the variation of CN* temperature with height seen in AP propellant flames [5], where the temperature fell as distance above the surface (and thus time) increased. This trend is not seen with NH, mainly because NH is not produced with high vibrational excitation. This is shown in Figure 92.

The high vibrational/rotational excitation of the CN and the more "thermal" distribution of the NH is due to the energetics of the reactions forming the two species. The amount of energy liberated or consumed in a reaction determines the final state of the species created. Using the heat of formation and excitation data from Table 9, the energetics of reactions R1 and R3 have been calculated:

$$C_2(a^3\Pi) + NO \rightarrow CN(B^2\Sigma) + CO \qquad \Delta H = -74.5 \text{ kcal/mole (exothermic)}$$
$$CN(A^2\Pi) + OH \rightarrow NH(A^3\Pi) + CO \qquad \Delta H = 12.2 \text{ kcal/mole}$$
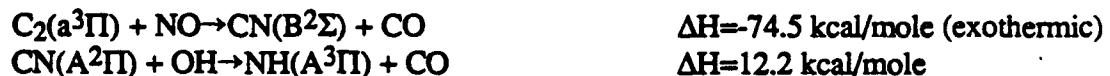
The heat of reaction of R1 has been calculated as -70.5 kcal/mole by Guillaume and Van Tiggelen [28], fairly good agreement considering the uncertainties in the heats of formation of the radical species. Note that R1 produces excess energy over and above the energy required to create the excited state CN. This excess energy appears in the products as excess rotational and vibrational energy. The energy difference between vibrational levels in $CN(B^2\Sigma)$ is approximately 2000 cm^{-1}, so 70-75 kcal/mole (equivalent to 24,500-26,250 cm^{-1}) is easily enough energy to explain the vibrational excitation observed in Figures 81 and 86. In contrast, R3 does not liberate excess energy in forming $NH(A^3\Pi)$, so that the "thermal" vibrational distribution of NH is consistent with R3 being the main channel forming $NH(A^3\Pi)$.

BURKE-SCHUMANN CALCULATIONS

The "classic" analysis of diffusion flame shape is that of Burke and Schumann [35]. In their analysis of diffusion flames in concentric tubes, they obtained the following result for over-ventilated (fuel-lean) flames:

$$\Sigma \left\{ (\phi_n)^{-1} \left\{ J_1(\phi_1 L) J_0(\phi_n x)/[J_0(\phi_n R)]^2 \right\} \exp[-D\phi_n^2 y/v] \right\} = (R^2 C_2/2LiC_0) - 0.5L \tag{1}$$

where J_0, J_1 = Bessel functions
R=radius of outer tube
L=radius of inner tube
x=radial distance of flame sheet
v=gas velocity
y=vertical distance above orifice of inner tube
D=fuel-oxidizer diffusion coefficient
C_1=initial concentration of fuel
C_2=inital concentration of oxidizer
$C_0 = C_1 + (C_2/i)$
i=Stoichiometry coefficient, moles oxidizer/moles fuel
ϕ_n=root of $J_1(\phi)=0$ (ϕ_1=3.83)

The flame height is calculated by setting $x=0$ and solving for y in Equation (1). A rough estimate can be obtained using only $n=1$ in the summation [35].

Data for CH_4/O_2 flame:
L=0.5 cm
R=1.1 cm
$C_1 = C_2 = 1$ (no diluent)
i=2 ($CH_4 + 2O_2 \rightarrow CO_2 + 2H_2O$)
CH_4=0.8 slpm=251.7 cm^3/s @ 40 torr=80.1 cm/s
O_2 flow=2.5 slpm=786.3 cm^3/s @ 40 torr=65.2 cm/s
D=4.2 cm^2/s @ 40 torr, 298 K [36], with $D/v \sim \rho D$=constant in flame

The end result is y=7.9 cm, compared with experimental value of 3-3.5 cm. The agreement is not as good as that reported by Burke and Schumann for 1 atm flames [35]. However, some indication has recently surfaced that the flow meters were reading inaccurately, so this calculation needs to be repeated with carefully calibrated flow meters.

Table 12. Energetics data for species involved in reactions R1, R2, and R3.

Molecule	Heat of formation, kcal/mole [32]	Heat of formation, kcal/mole [34]
CO	-26.42	-29.4
NO	21.6	20.8
C_2	199	198.4
CN	101	100.5
OH	9.4	9.5
NH	90	86.9
CH	142	140.9

Excited electronic state energies [21]*:

Molecule	State	Energy, cm^{-1}
C_2	d $^3\Pi_r$	20022.5
C_2	a $^3\Pi_u$	716.2
C_2	X $^1\Sigma_g^+$	0
NH	A $^3\Pi_i$	29807
NH	X $^3\Sigma^-$	0
CO	a $^3\Pi_r$	48686.7
CO	X $^1\Sigma^+$	0
CN	B $^2\Sigma^+$	25752
CN	A $^2\Pi_i$	9245.3
CN	X $^2\Sigma^+$	0
OH	A $^2\Sigma^+$	32684.1
OH	X $^2\Pi_i$	0
NO	A $^2\Sigma^+$	43965.7
NO	X $^2\Pi_r$	0
CH	B $^2\Sigma^-$	(26044)
CH	A $^2\Delta$	23189.8
CH	X $^2\Pi_r$	0
N_2	A $^3\Sigma^+$	50203.6
N_2	X $^1\Sigma^+$	0

Common names for transitions: C_2 d→a "Swan bands", CO a→X "Cameron bands", CN A→X "CN red system", CN B→X "CN violet system", NO A→X "γ bands"
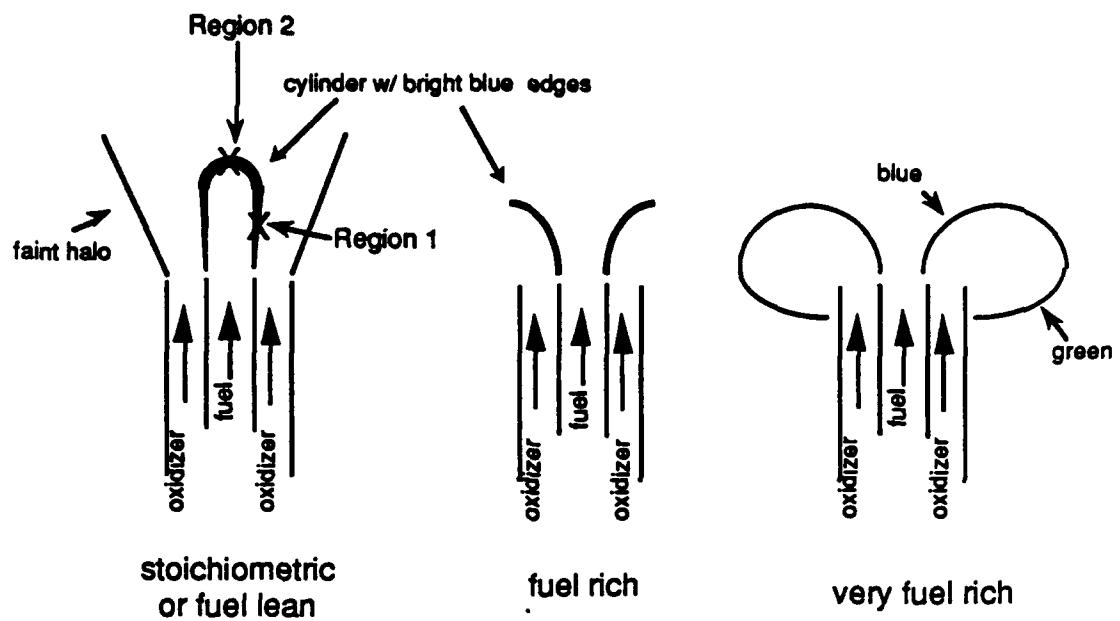
Figure 61. CH4/O2 diffusion flame structure at 40 mm Hg pressure.
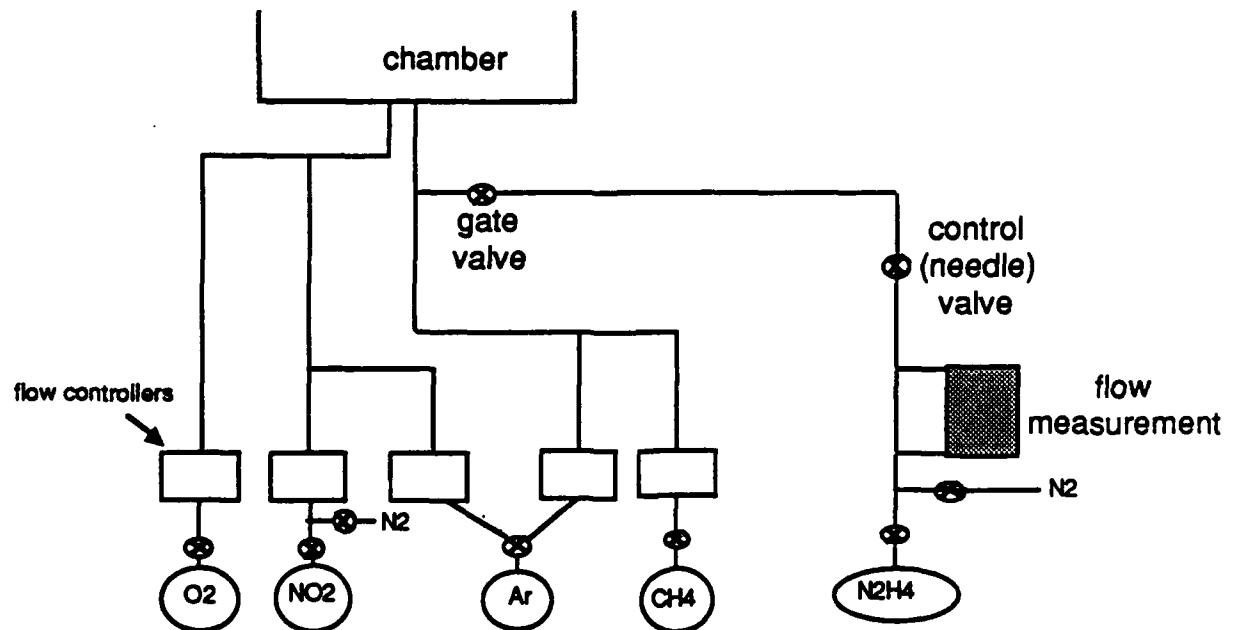
Figure 62. Fuel/oxidizer feed schematic.
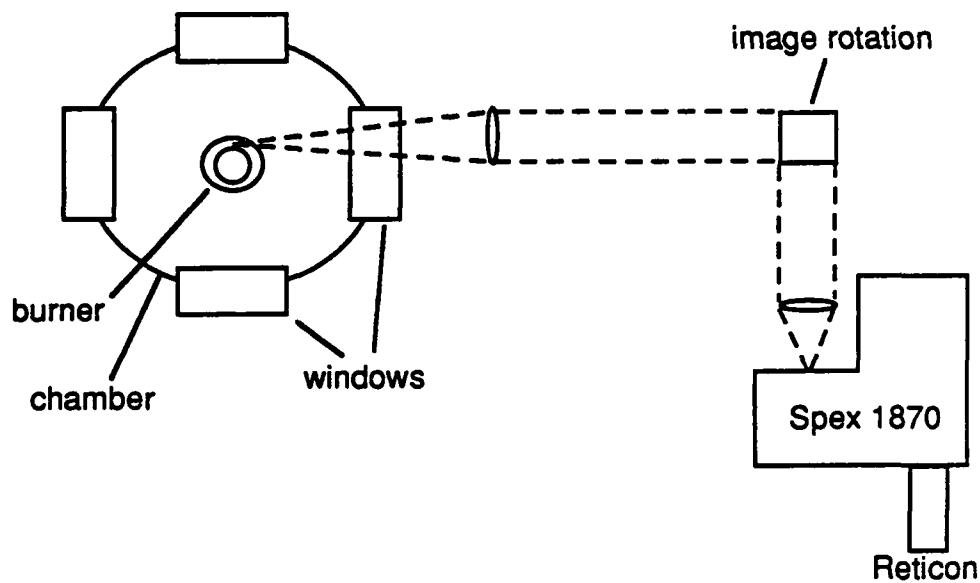
Figure 63. Schematic (top view) of apparatus showing optical collection path.
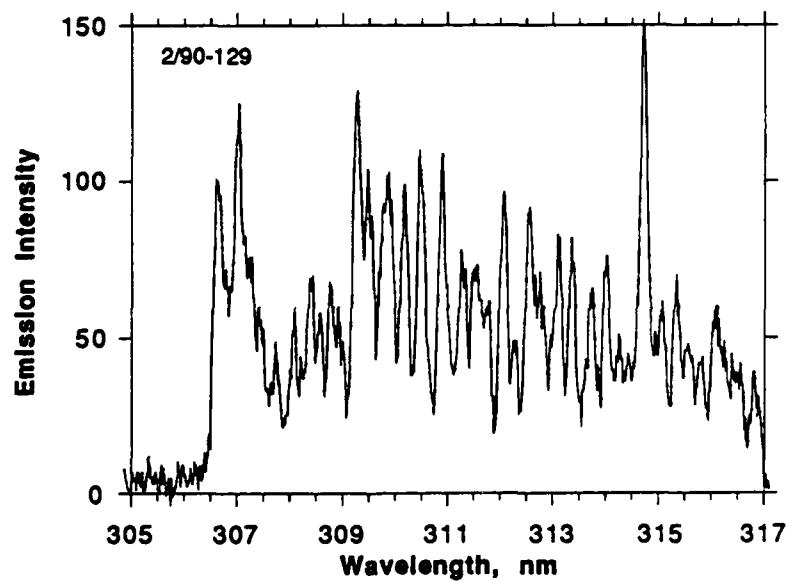
Figure 64. OH ($A^2\Sigma$-$X^2\Pi$) emission spectrum, CH_4/O_2 diffusion flame (0.8/2.5 slpm), 40 mm Hg pressure, 0.5 s exposure time, 0.0175 nm/pixel dispersion.
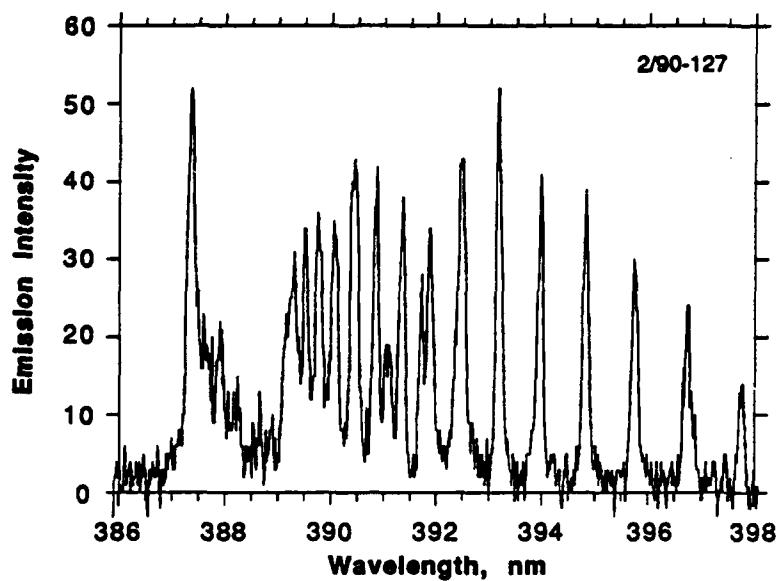
Figure 65. CH ($B^2\Sigma$-$X^2\Pi$) emission spectrum, CH_4/O_2 diffusion flame (0.8/2.5 slpm), 40 mm Hg pressure, 0.2 s exposure time, 0.0175 nm/pixel dispersion.
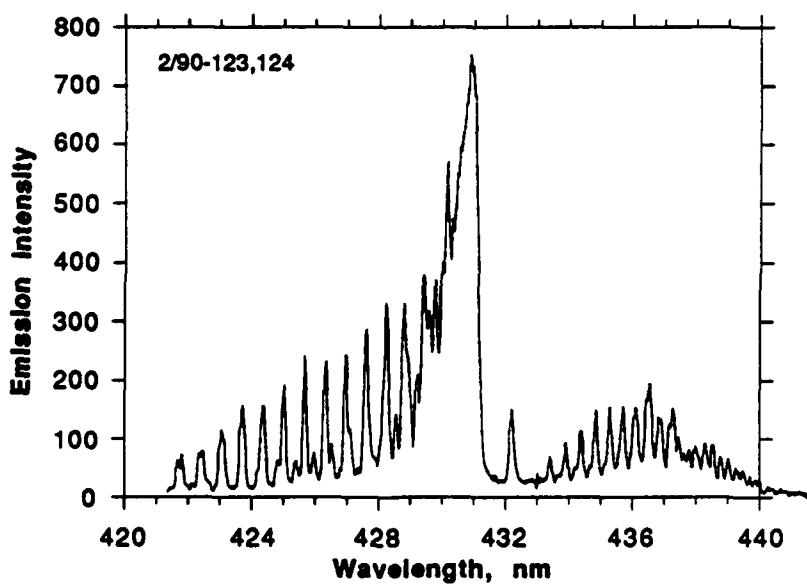
Figure 66. CH ($A^2\Delta$-$X^2\Pi$) emission spectrum, CH_4/O_2 diffusion flame (0.8/2.5 slpm), 0.2 s exposure time, 40 mm Hg pressure, 0.0175 nm/pixel dispersion.
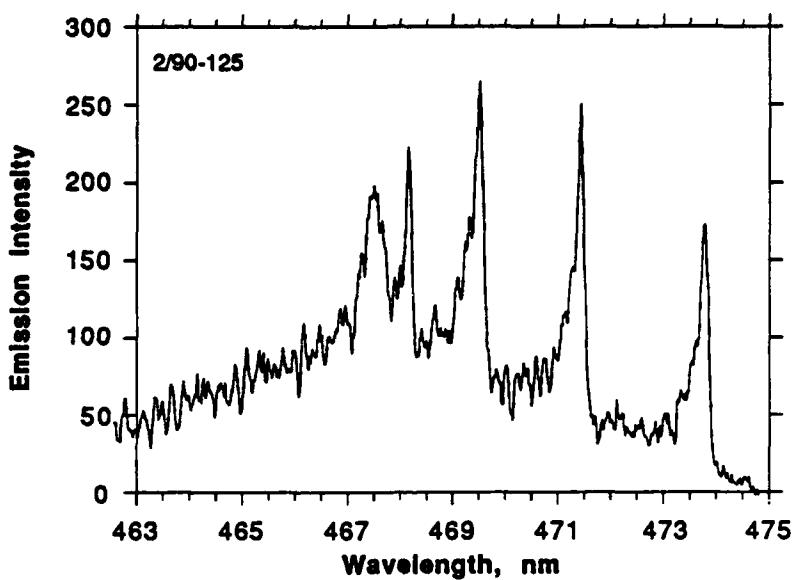
Figure 67. C_2 ($d^3\Pi$-$a^3\Pi$) emission spectrum, CH_4/O_2 diffusion flame (0.8/2.5 slpm), 0.2 s exposure time, 40 mm Hg pressure, 0.0175 nm/pixel dispersion.
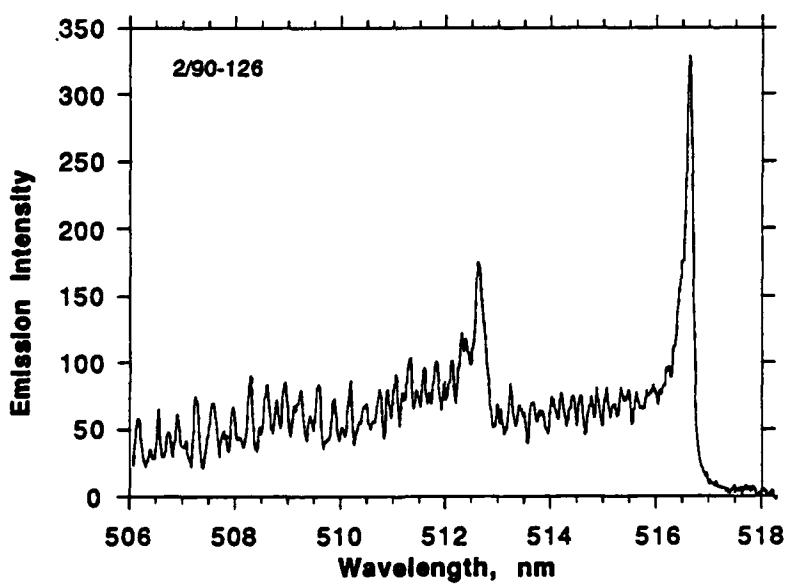
Figure 68. C_2 ($d^3\Pi$-$a^3\Pi$) emission spectrum, CH_4/O_2 diffusion flame (0.8/2.5 slpm), 40 mm Hg pressure, 0.2 s exposure time, 0.0175 nm/pixel dispersion.
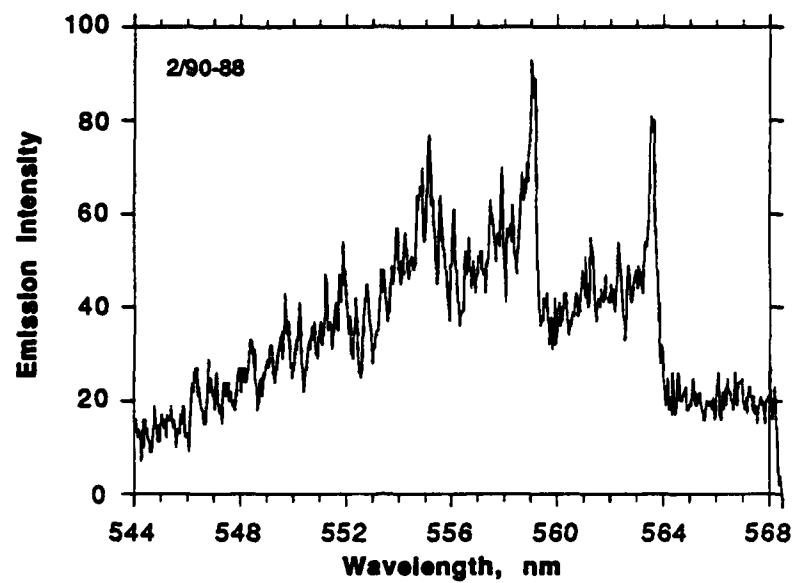
Figure 69. C_2 ($d^3\Pi$-$a^3\Pi$) emission spectrum, CH_4/O_2 diffusion flame (0.8/2.5 slpm), 40 mm Hg pressure, 0.2 s exposure time, 0.035 nm/pixel dispersion.
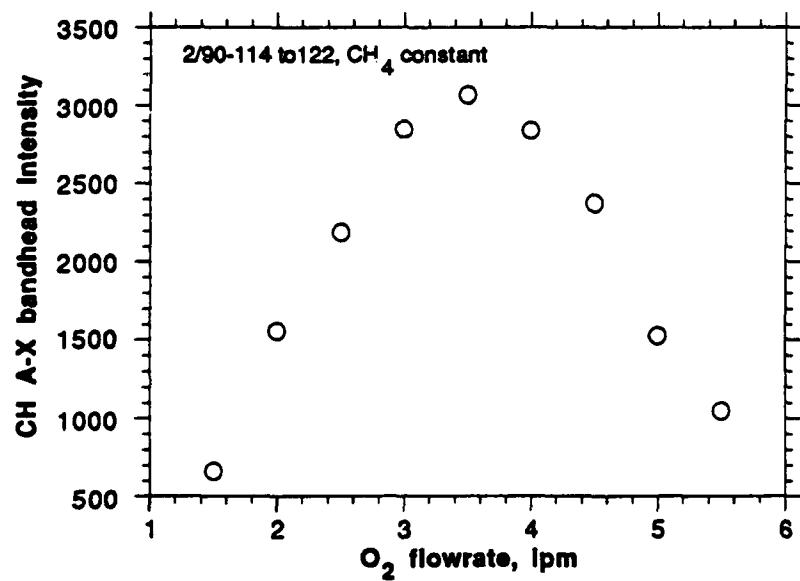
Figure 70. CH emission intensity (A-X bandhead at 431 nm) as a function of O_2 flow rate (CH_4 constant at 0.8 slpm).
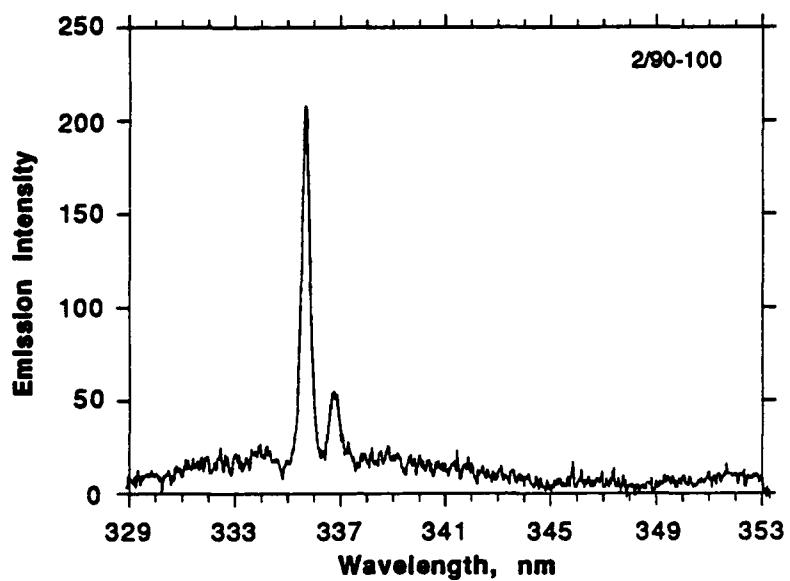
Figure 71. NH ($A^3\Pi$-$X^3\Sigma$) emission spectrum, $CH_4/O_2/NO_2$ diffusion flame (0.8/2.5/25 slpm), 40 mm Hg pressure, 0.2 s exposure time, 0.035 nm/pixel dispersion.
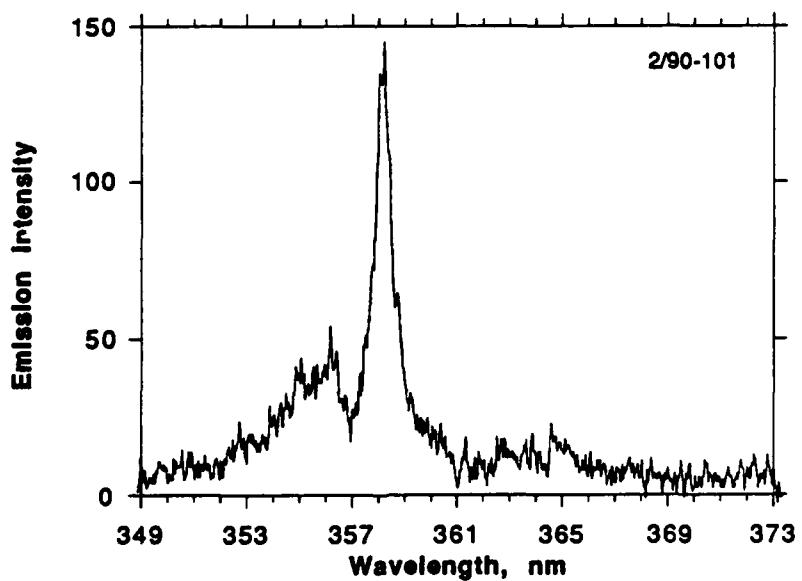
Figure 72. CN ($B^2\Sigma$-$X^2\Sigma$) emission spectrum, $CH_4/O_2/NO_2$ diffusion flame (0.8/2.5/25 slpm), 40 mm Hg pressure, 0.2 s exposure time, 0.035 nm/pixel dispersion.
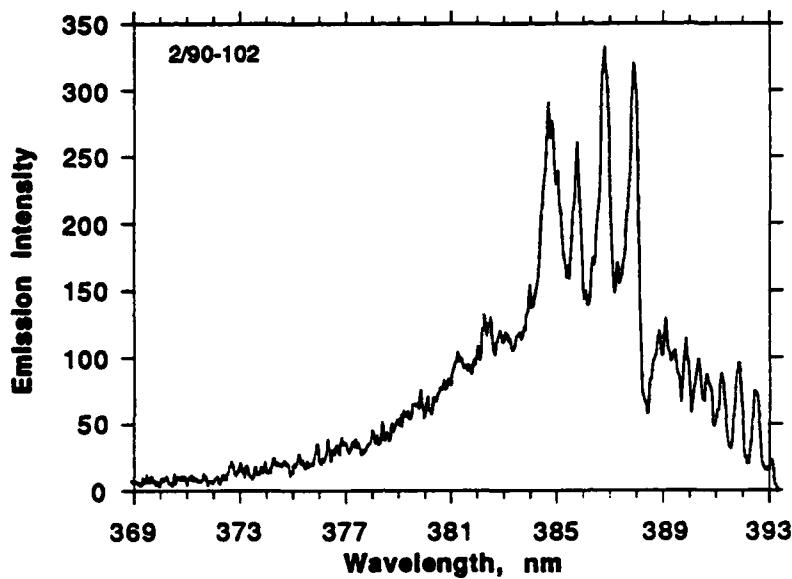
Figure 73. CN ($B^2\Sigma$-$X^2\Sigma$) (+CH) emission spectrum, $CH_4/O_2/NO_2$ diffusion flame (0.8/2.5/25 slpm), 40 mm Hg pressure, 0.2 s exposure time, 0.035 nm/pixel dispersion.
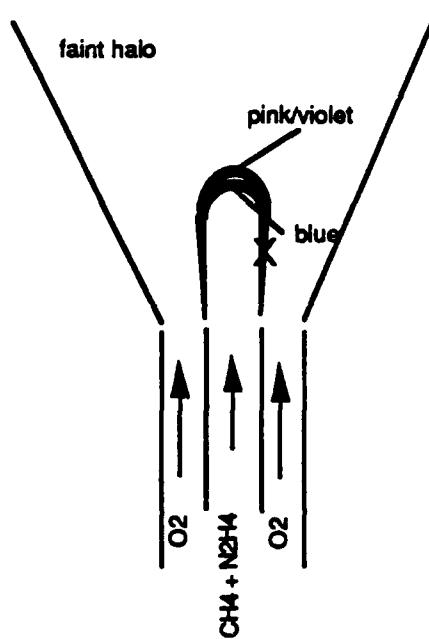
Figure 74. $CH_4/O_2/N_2H_4$ flame schematic (45 mm Hg).

64
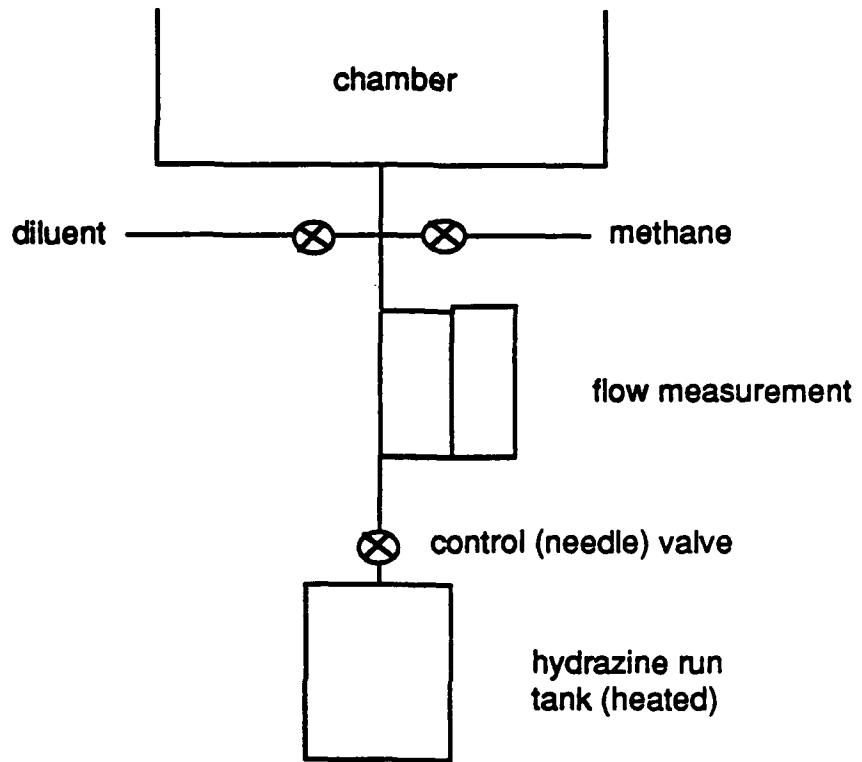
Figure 75. Schematic of new N₂H₄ feed system.
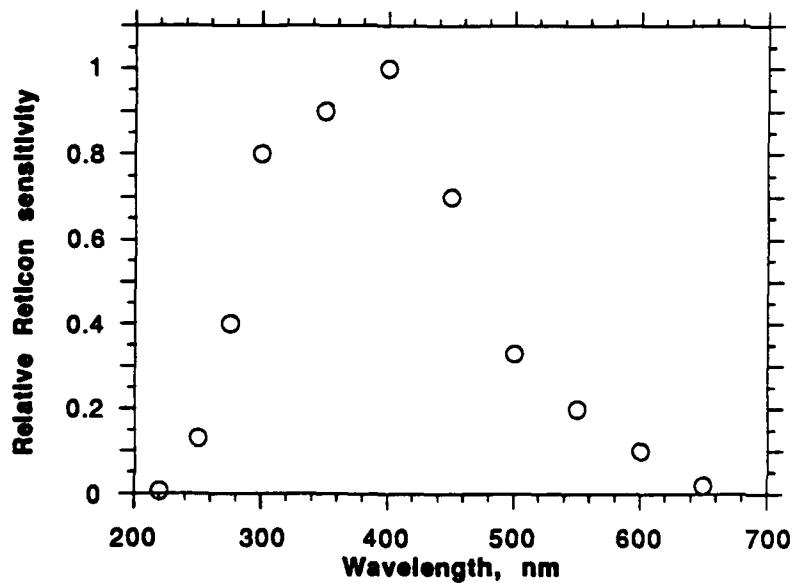
Figure 76. Reticon sensitivity as a function of wavelength.
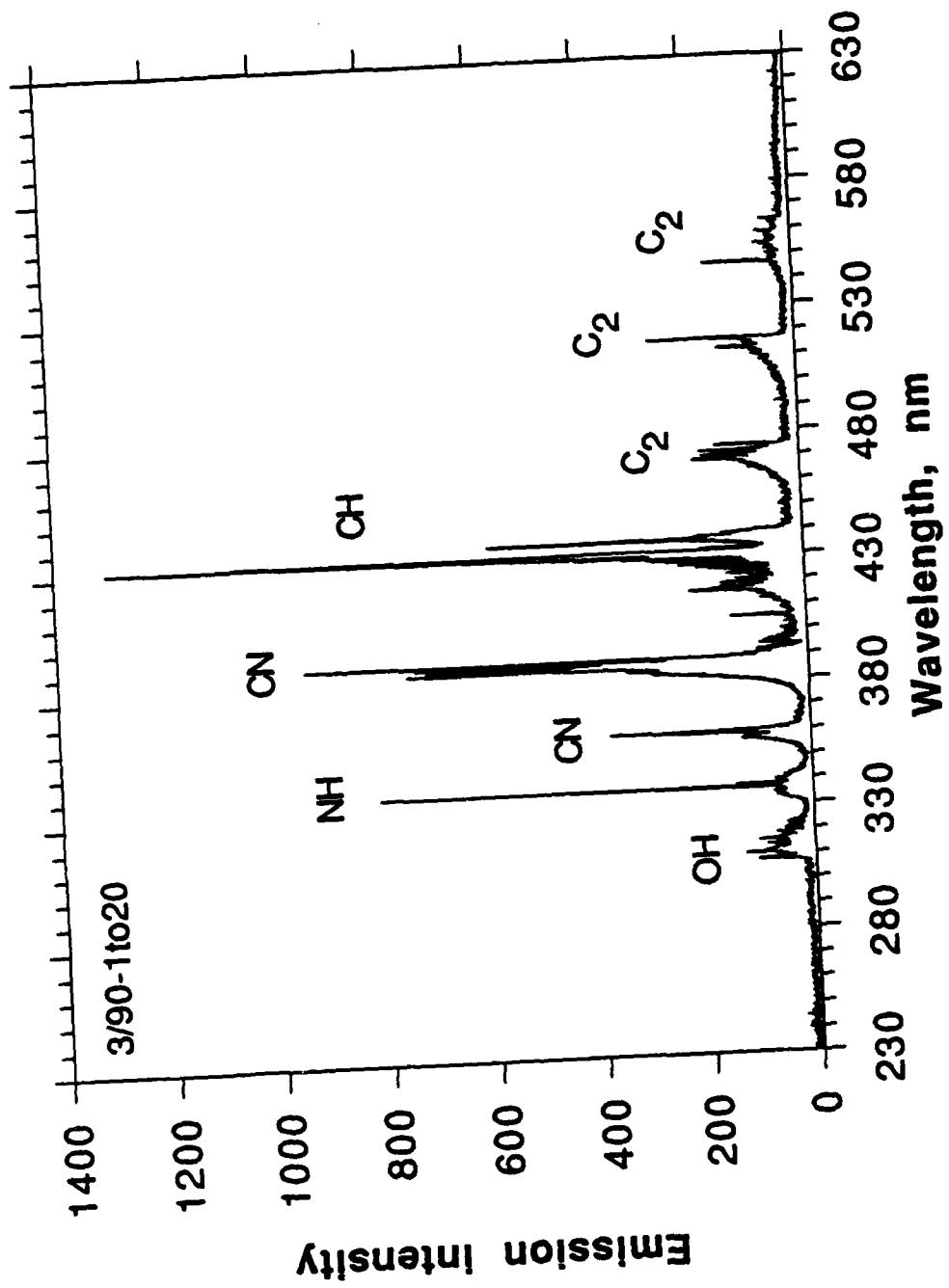
Figure 77. Composite (20 spectra) emission spectrum, $CH_4/N_2H_4/O_2$ diffusion flame (0.8/?/2.5 slpm), 0.2 s exposure time, 0.035 nm/pixel dispersion.

66
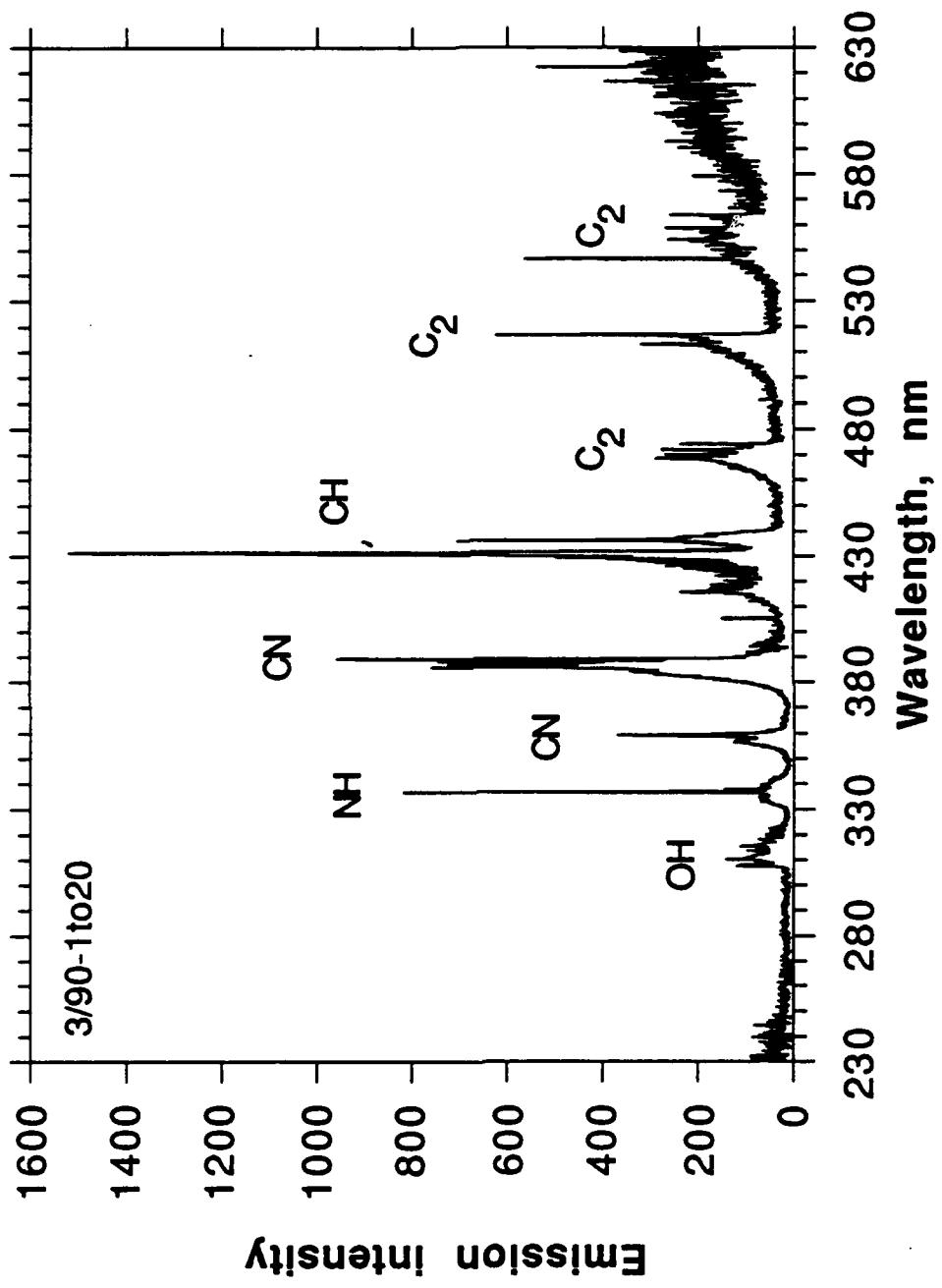
Figure 78. Composite (20 spectra) emission spectrum of Figure 17 corrected for Reticon spectral response (Figure 76).

67
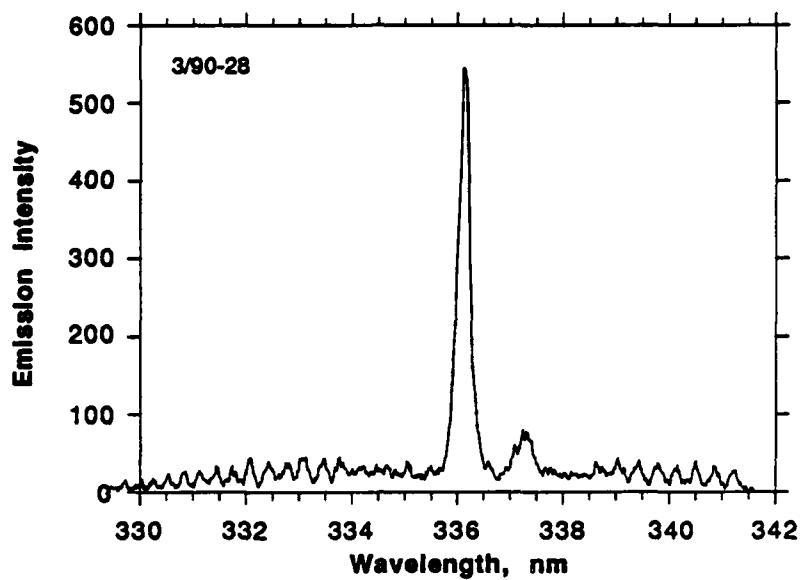
Figure 79. NH (A$^3\Pi$-X$^3\Sigma$) emission spectrum, CH$_4$/N$_2$H$_4$/O$_2$ diffusion flame (0.8/?/2.5 slpm), 45 mm Hg pressure, 0.4 s exposure time, 0.0175 nm/pixel dispersion.
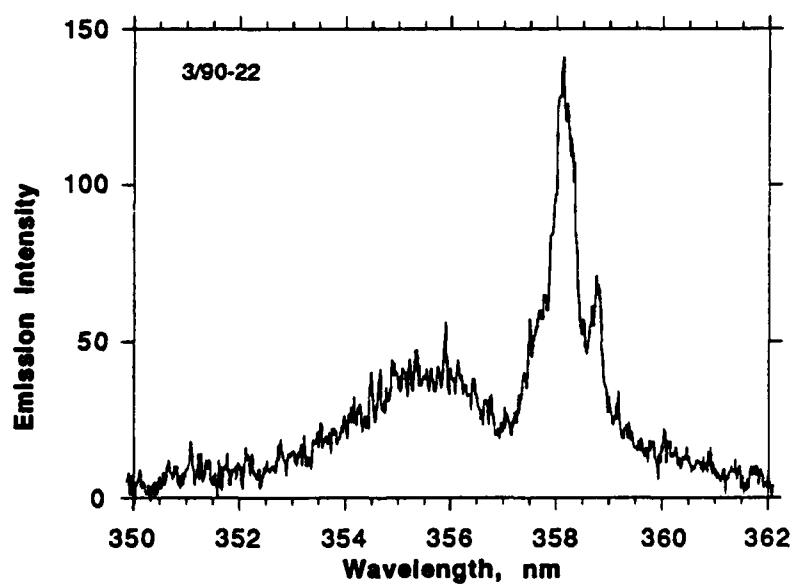
**Figure 80.** CN (B$^2\Sigma$-X$^2\Sigma$) emission spectrum, CH$_4$/N$_2$H$_4$/O$_2$ diffusion flame (0.8/?/2.5 slpm), 45 mm Hg pressure, 0.4 s exposure time, 0.0175 nm/pixel dispersion.
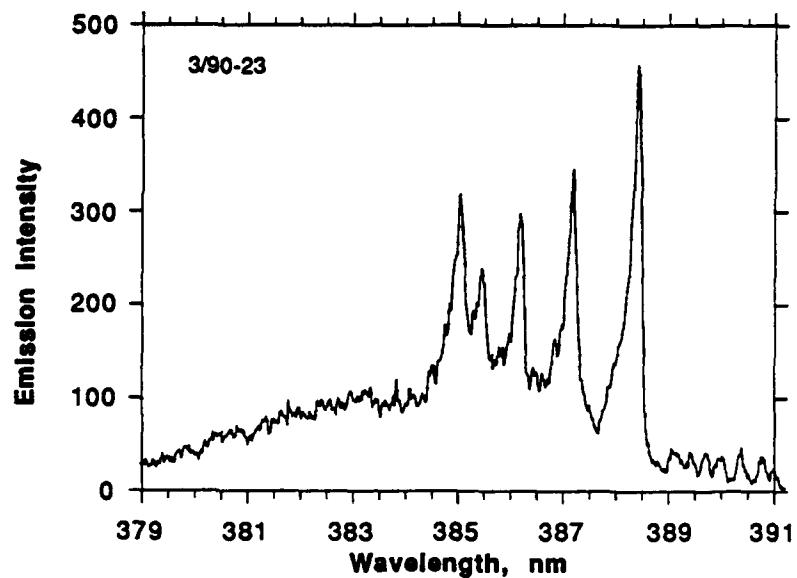
Figure 81. CN ($B^2\Sigma$-$X^2\Sigma$) (+CH) emission spectrum, $CH_4/N_2H_4/O_2$ diffusion flame (0.8/?/2.5 slpm), 45 mm Hg pressure, 0.4 s exposure time, 0.0175 nm/pixel dispersion.
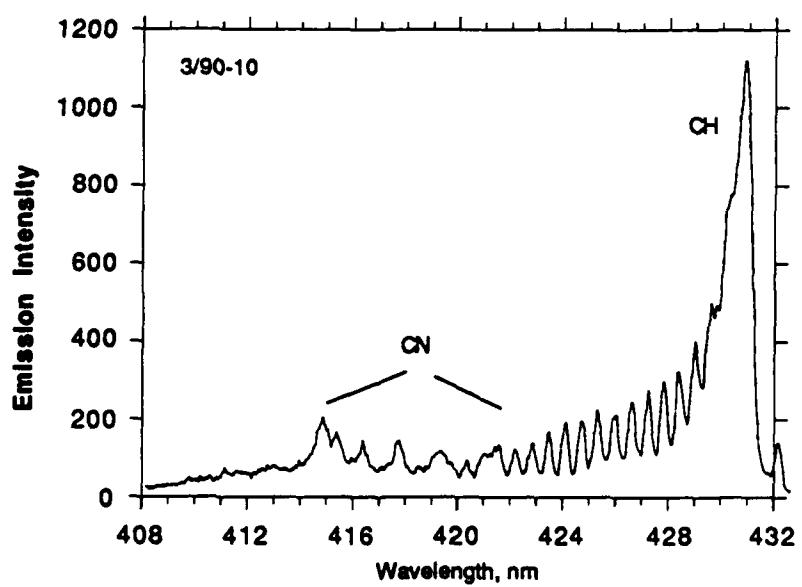
Figure 82. Emission spectrum, $CH_4/N_2H_4/O_2$ diffusion flame (0.8/?/2.5 slpm), 50 mm Hg pressure, 0.2 s exposure time, 0.035 nm/pixel dispersion.

69
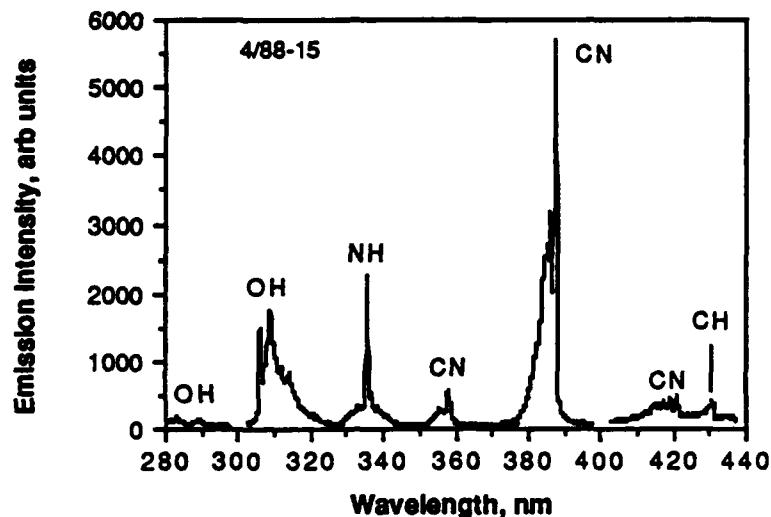
Figure 83. Broadband emission spectrum of inner cone of CH_4/N_2O premixed flame, 1 atm. 500/200 μm slits, 0.07 nm/pixel dispersion, 0.2 s exposure time.
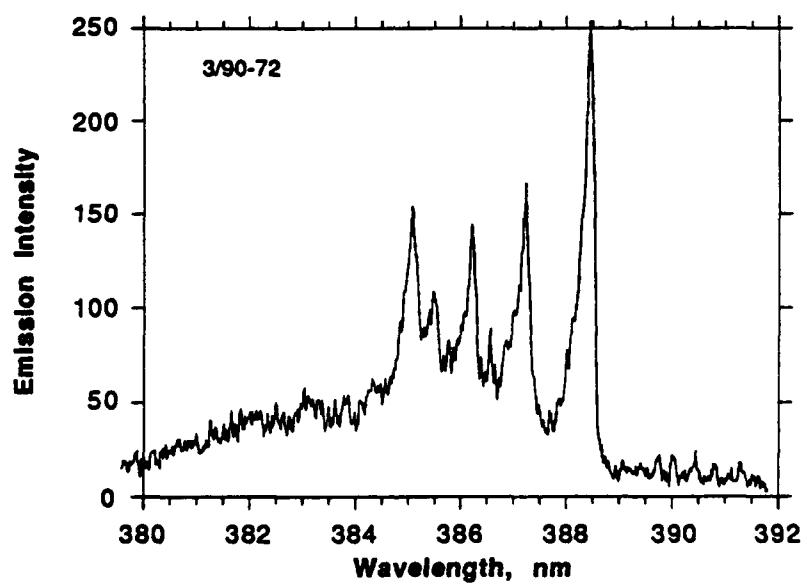
Figure 84. CN ($B^2\Sigma$-$X^2\Sigma$) emission spectrum, CH_4/N_2O diffusion flame (0.4/2.5 slpm), 80 mm Hg pressure, 0.4 s exposure time, 0.0175 nm/pixel dispersion.
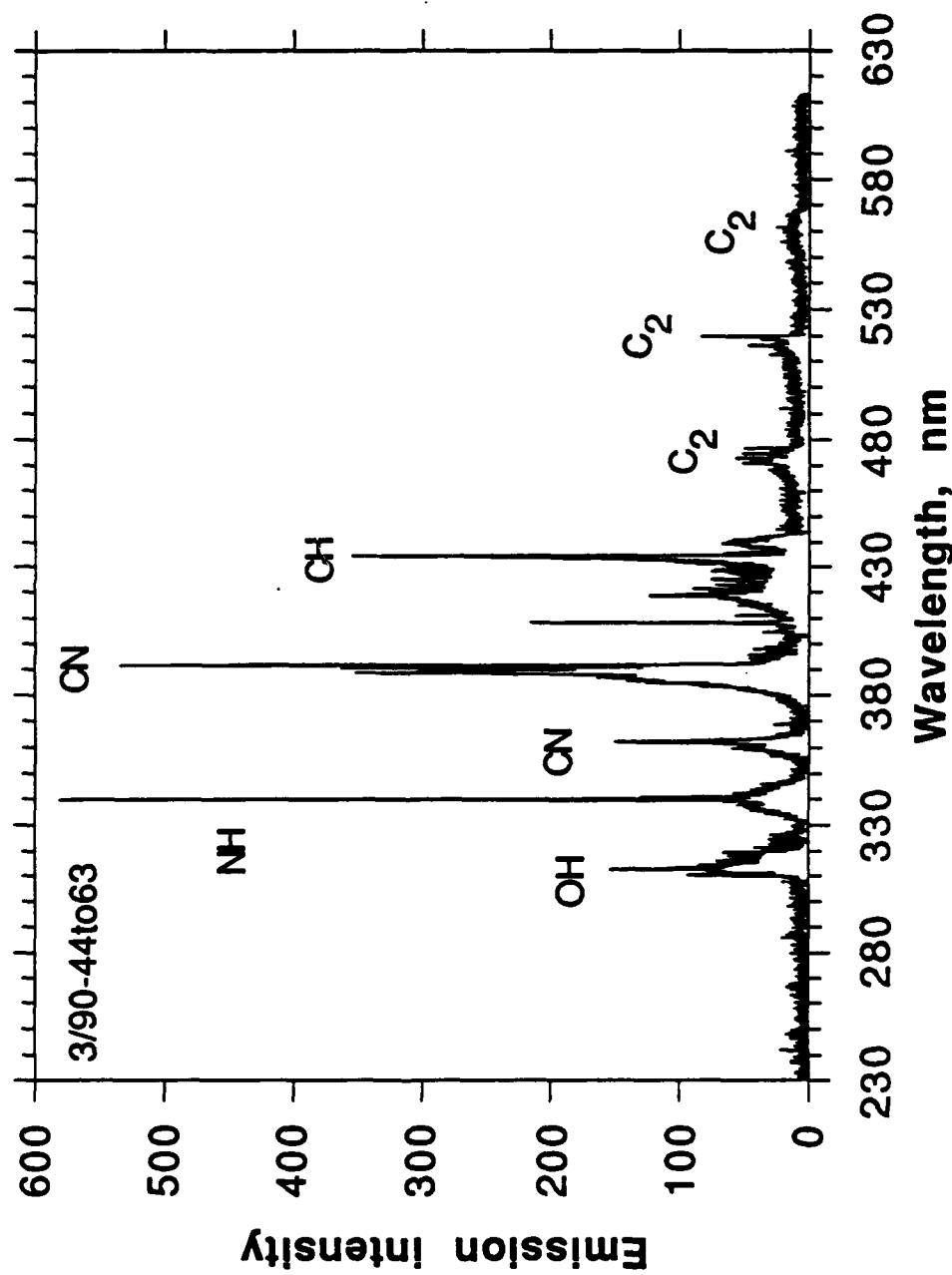
Figure 85. Composite emission spectrum, CH_4/N_2O diffusion flame (0.4/2.5 slpm), 80 mm Hg pressure, 0.4 s exposure time, 0.035 nm/pixel dispersion.

71
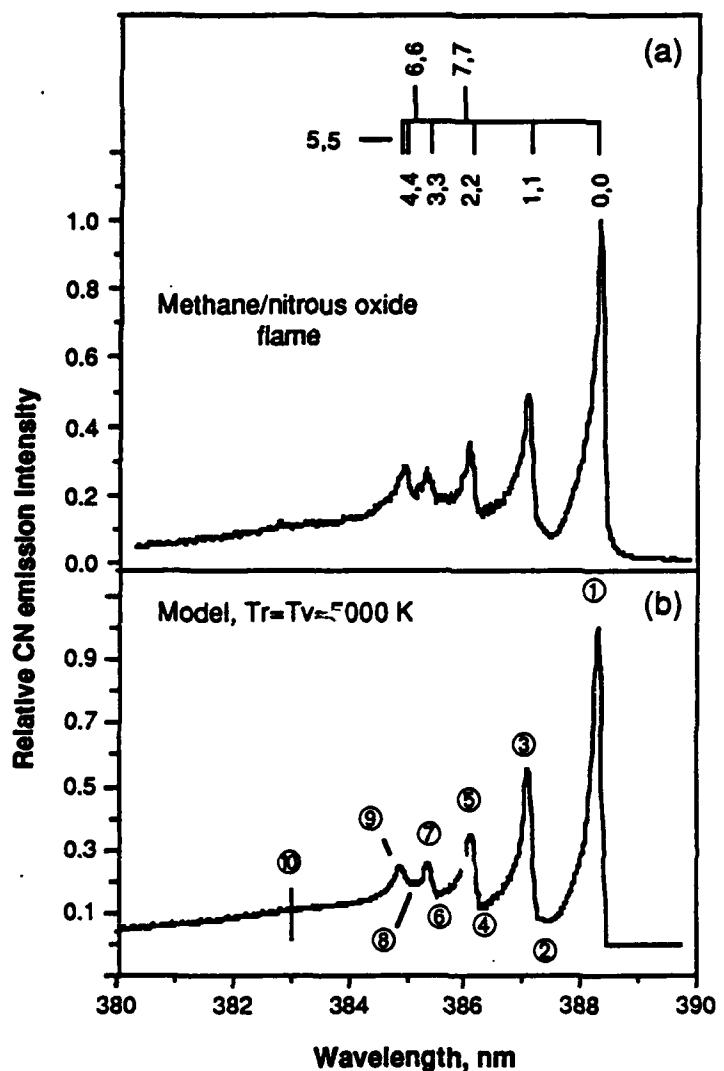
**Figure 86.** Sample CN ($B^2\Sigma$-$X^2\Sigma$) emission spectra. (a) CH_4/N_2O flame, 1 atm. (b) Model spectrum with $T_r=T_v=5000$ K.
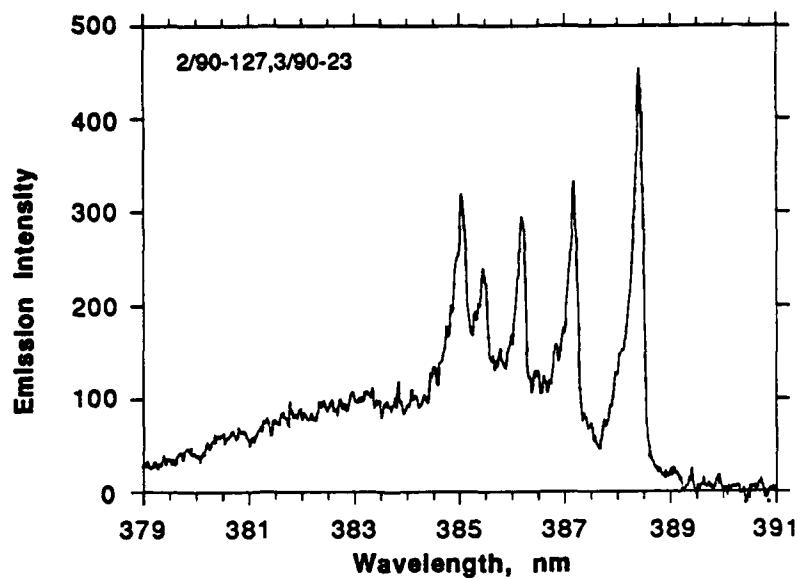
Figure 87. CN $(B^2\Sigma\text{-}X^2\Sigma)$ emission spectrum, $CH_4/N_2H_4/O_2$ diffusion flame, created by subtracting CH emission (Figure 5) from Figure 20.
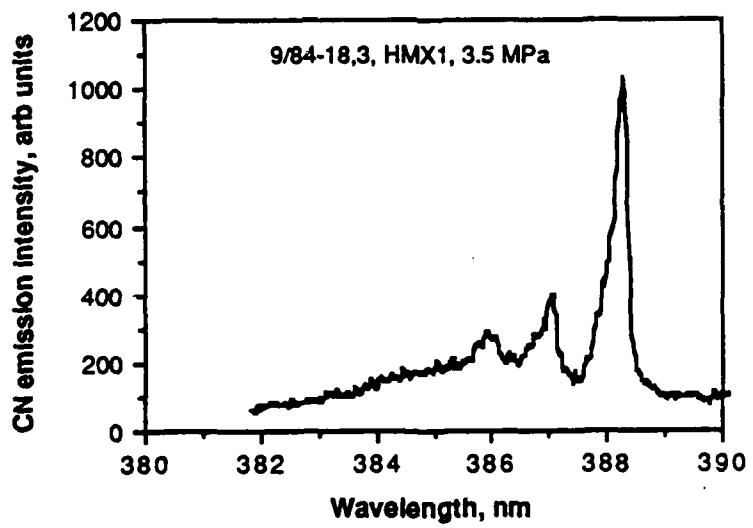
Figure 88. CN $(B^2\Sigma\text{-}X^2\Sigma)$ emission. HMX1 propellant, 3.5 MPa, 0.0175 nm/pixel dispersion, 0.24 s exp. time, 500/100 μm slits, h=1-2mm.
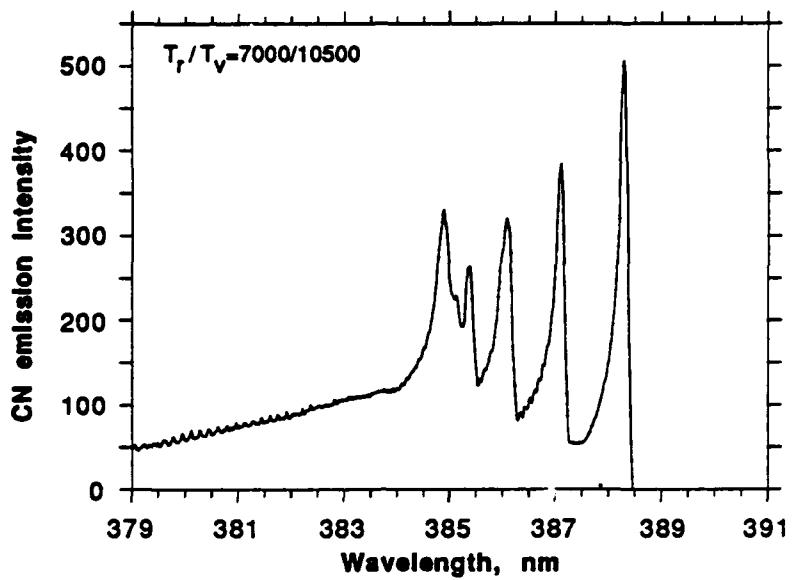
Figure 89. Model CN ($B^2\Sigma$-$X^2\Sigma$) emission spectrum. T_r=7000 K, T_V=10500 K (0,0 band sequence).
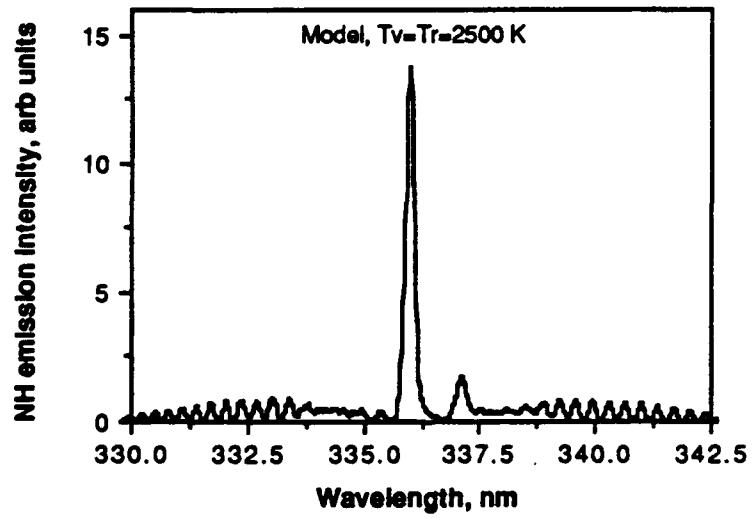
Figure 90. Model NH ($A^3\Pi$-$X^3\Sigma$) emission spectrum (T_V=T_r=2500 K).

74
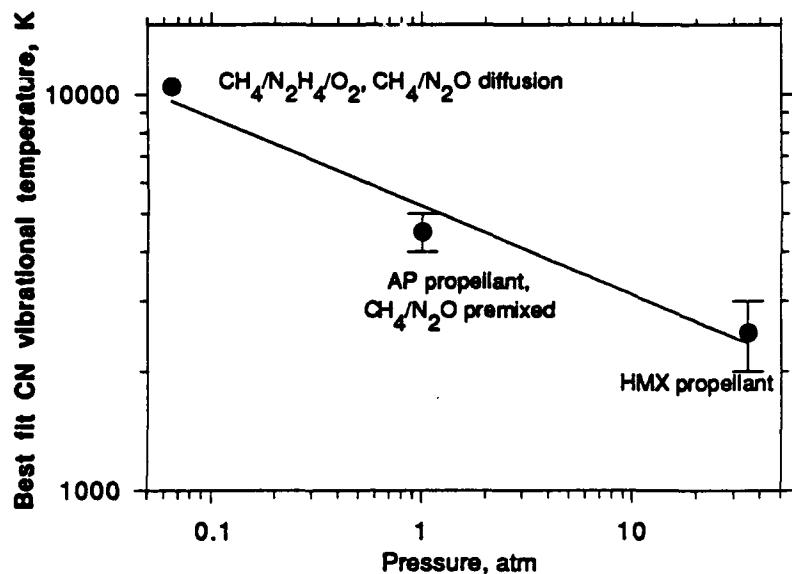
Figure 91. Relationship between pressure and CN emission (upper state) temperature.
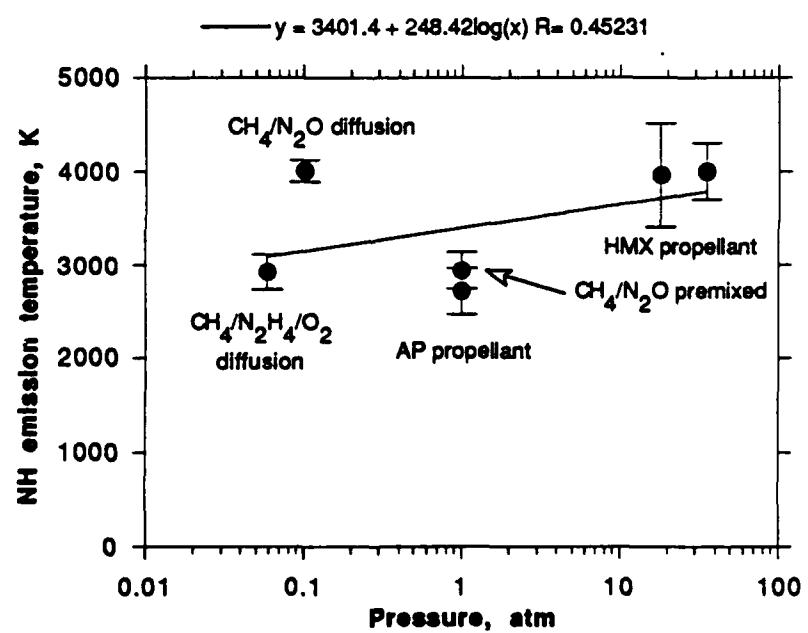
Figure 92. Relationship between pressure and NH emission (upper state) temperature.

CHEMICAL KINETIC MODELING

INTRODUCTION

Current solid propellant combustion models treat the propellant flame chemistry in a relatively limited way, defining the chemistry in terms of several global reactions, and determining the combustion behavior mainly via a heat transfer analysis [38,39]. In some cases, the lack of chemical detail has limited the predictive capability of these type of models. Conversely, the general lack of understanding of the propellant flame chemistry has limited the development of global reaction combustion models, since it is not clear which global reactions should be used. To improve the knowledge of propellant flame chemistry more research needs to be done.

Validation of detailed models of propellant combustion requires comparison of model predictions with experimental data collected in the propellant flame under combustion conditions of interest. The needed data are the temperature profile and species profiles in the propellant flame under combustion conditions. Such data is relatively sparse and difficult to obtain, compared with (for example) the amount of information available for methane/air flames. Kubota's group in Japan has measured temperature profiles in propellants using microthermocouples [40,41]. Other microthermocouple measurements in propellant flames have been performed in Italy [42], France [43], the Soviet Union [44] and the United States [45,64]. Probe sampling of species has been done in propellant flames in Japan [40] and the Soviet Union [46]. Both microthermocouple temperature measurements and probe sampling are intrusive measurements, with the possibility of disturbing the flame chemistry and structure during measurement. Nonintrusive optical measurements have been made in propellant flames, by such methods as emission [2], absorption [12], CARS [13], and laser-induced fluorescence (LIF) [4,5,10]. IR spectroscopy has been used to detect product species in high rate thermolysis of propellant ingredients [47]. It is this detailed data to which model predictions need to be compared, rather than just comparing experimental and theoretical burn rates, for example.

Detailed kinetic modeling of propellant flames is not a new development [48,49], although chemical kinetic modeling in general has only recently become "routine" with production codes such as the Sandia premixed flame code [50] often used to model various types of flames [30]. Propellant-related experimental/modeling efforts are underway, such as CH_2O/NO_2 and CH_2O/N_2O [51,52], C_2N_2/NO_2 and HCN/NO_2 [53], and CH_4/NO_2 [11,52]. Research in the Soviet Union has also been active, with kinetic models developed for $NH_3/HClO_4$ (AP) flames [54] and hexogen (RDX) flames [55]. In the 1960's, there was a great deal of research, primarily in Great Britain and France, on ClO_x-oxidized flames [56]. The recent increases in computer capabilities have allowed detailed kinetic models of nitramine combustion to be developed which include the solid $\rightarrow$ gas transition, thus allowing the determination of the propellant burn rate. Hatch developed complete models for nitrate ester and HMX combustion [57], the latter utilizing 77 reactions involving 26 species. Melius developed a detailed chemical kinetic model of RDX ignition and RDX/HMX combustion [58], with a recommended set of 131 reactions involving 32 species (including the nitramine molecule). One of Melius' most interesting conclusions was that the higher vapor pressure of

77

RDX led to very little condensed phase reaction, while over 50% of the higher boiling HMX reacted in the condensed phase prior to vaporization. The condensed phase decomposition of HMX is generally thought to produce $CH_2O + N_2O$, while the gas phase decomposition produces NO_2 and H_2CN through a concerted ring degradation mechanism after an NO_2 group is removed from the parent nitramine [47,59]. This picture is not universally agreed upon, with some HMX combustion models neglecting the H_2CN/NO_2 path altogether, focussing on the CH_2O/N_2O pathway [60].

In this section, available experimental species data from solid propellant flames is compared with chemical kinetic models for propellants HMX1, HMX2, and AN1 (see Table 1). HMX2 is similar to a propellant studied by Kubota [40], while HMX1 has been studied by a variety of diagnostic techniques by several groups [4,5,10,12,13,61]. AN propellants are of current interest because of the desire to minimize toxic exhaust products, such as the HCl found in the exhaust of rockets burning ammonium perchlorate-based propellants. Two chemical kinetic mechanisms are used. The first is the mechanism of Hatch [57] with the reaction $H_2CN+M-->H+HCN$ added. This mechanism is listed in Appendix 1. The second mechanism is the Miller-Bowman mechanism for nitrogen chemistry in flames [30], as extended by Zabarnick [11]. This mechanism is listed in Appendix 2. The Hatch mechanism doesn't include hydrocarbons, so binder decomposition products were limited to CH_2O. This will be discussed further in the next subsection. The propellants are modeled as premixed, burner-stabilized flames, an approximation discussed in the following subsections This type of model requires a temperature profile as an input. The codes were run on a Macintosh II computer with 4 megabytes of RAM (Hatch mechanism) and a VAX 8650 (extended Miller-Bowman mechanism).

HMX1 PROPELLANT

For the modeling portion of this work, the decision was made to narrow the focus of the model to the changes in flame structure created by adding binder decomposition species to a "baseline" HMX reaction scheme. To avoid solving the coupled gas/solid problem with the wide swings in burn rate possible depending on the species added, a simpler situation was solved. An experimental temperature profile was used with the Sandia premixed flame code to solve a burner-stabilized flame of the same mass burning rate as that of the propellant (which was known [5]). Thus the temperature profile and burn rate are inputs (and assumed to be correct), and the starting species are varied to determine the effect of adding binder decomposition products to the flame. One of the main drivers behind this work was that experimental propellant species profiles (such as CN) seemed to be more extended than respective CN profiles in HMX monopropellant models [58]. One of the goals of this work is to determine if this could be due to the presence of the binder. Burn rate prediction was not a goal of this work. In this model, the gases from the HMX and the binder are assumed to be premixed instantaneously, although the propellant is heterogeneous (200 and 20 μm HMX particles in the binder). Since the stoichiometries of the binder/plasticizer and the HMX are similar, important diffusion flames are not formed as in AP propellants although there will be some diffusional mixing. Diffusion flame modeling incorporating detailed kinetics is being performed [65], but is outside the scope of this work.

78

The first results described here involve the reaction scheme of Hatch [57] for HMX combustion which includes 77 gas phase reactions involving HCN, CN, N, H, NH_3, NH_2, N_2, NH, HNO, HNCO, NCO, NO_2, N_2O, NO, CH_2O, HCO, CO, CO_2, O, O_2, OH, H_2O, H_2, H_2O_2, N_2H, and HO_2. This can be compared to Melius' 131 reaction set which adds reactions involving HMX, HMX radical (HMX minus NO_2), H_2CNNO_2, C_2N_2, H_2CN, HONO, and HOCN. The reaction $H_2CN + M \rightarrow H + HCN + M$ from Melius was added to Hatch's reaction set. The second reaction mechanism used is the Miller Bowman mechanism for nitrogen chemistry in flames [30], as extended by Zabarnick [11]. This mechanism includes 252 reactions involving 54 species. In addition to the species included in the Hatch mechanism, the mechanism includes hydrocarbon species as well as HCNO, HOCN, HONO, HNO_3, and C_2N_2.

The HMX decomposition was modeled as occurring by one of two pathways:

HMX ($C_4H_8N_8O_8$) $\rightarrow$ 2 CH_2O + 2 H_2CN + 2 N_2O + 2 NO_2
HMX $\rightarrow$ 4 CH_2O + 2 N_2 + 4/3 N_2O + 4/3 NO_2
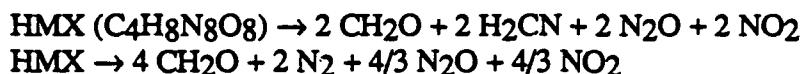
The first pathway assumes equality between the gas and liquid phase decomposition reactions (described above). The second pathway is from Kubota [40]. Relative equality between the H_2CN/NO_2 (gas phase decomposition) and CH_2O/N_2O (liquid phase decomposition) pathways has been found experimentally [47] and predicted theoretically [58] for HMX. The "branching ratio" between the two pathways is probably dependent on pressure and heating rate. RDX is found to break down mostly through the H_2CN/NO_2 pathway because of its higher vapor pressure and consequently greater tendency to vaporize before decomposition [47,58]. The TMETN in propellant HMX1 was assumed to immediately break up via:

TMETN ($C_5H_9N_2O_9$) $\rightarrow$ 3 CH_2O + 3 NO_2 (Hatch mechanism)
TMETN $\rightarrow$ 3 CH_2O + 3 NO_2 + C_2H_4
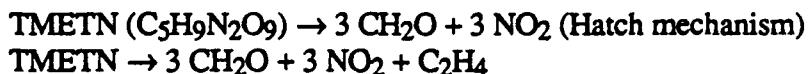
Note that neither scheme is stoichiometrically balanced. These two reactions appear to be reasonable assumptions [39,57,62], although to be completely correct stoichiometrically, the reaction should show some NO/CO/hydrocarbon/aldehyde formation (seen experimentally in Reference 62), e.g.: TMETN ($C_5H_9N_3O_9$) $\rightarrow$ 2 CH_2O + 2 NO_2 + NO + CH_2CHO. Two decomposition schemes were used for the binder (R-18, -[(-CH_2-CH_2-O-(C=O)-(CH_2)$_4$-(C=O)-O-]$_n$):

binder ($C_8H_{12}O_4$) $\rightarrow$ 3 C_2H_4 + 2 CO_2.
binder $\rightarrow$ 4 CH_2O (Hatch mechanism)
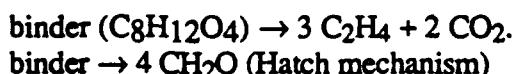
Again, one of the reactions is not stoichiometrically balanced because of the lack of hydrocarbons in the Hatch mechanism. The flame combustion mechanisms of species such as C_2H_4 are relatively well understood, at least in flames with O_2 as the oxidizer [63]. The formation (and incomplete combustion) of solid carbon (soot) may also be important [68] and is not included. In total then, there are four sets of modeling results, the two HMX paths with the Hatch mechanism, and the two HMX paths with the Miller-Bowman mechanism. The major species results for these four sets are shown in Figures 93-96.

79
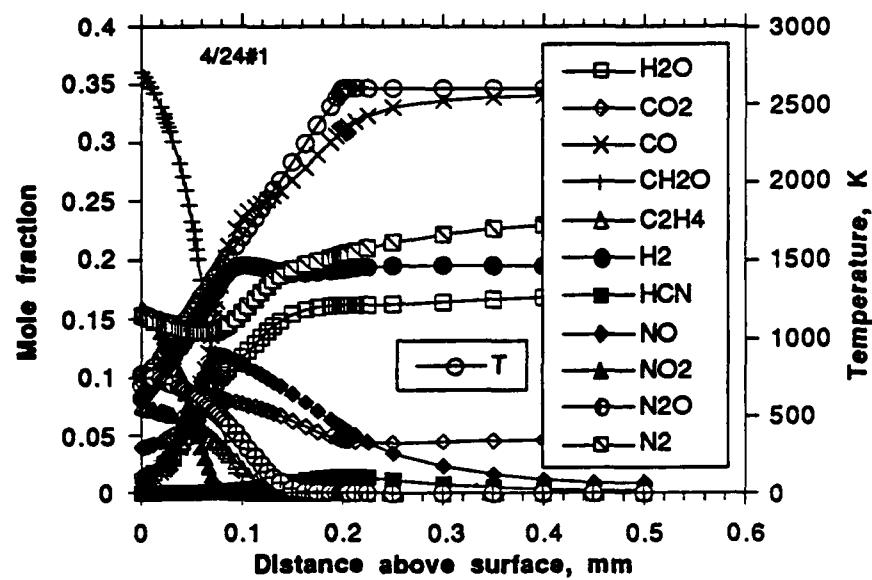
Figure 93. **Results of model for propellant HMX1, 15 atm.** Miller-Bowman mechanism; HMX → 4 CH_2O + 2 N_2 + 4/3 N_2O + 4/3 NO_2.
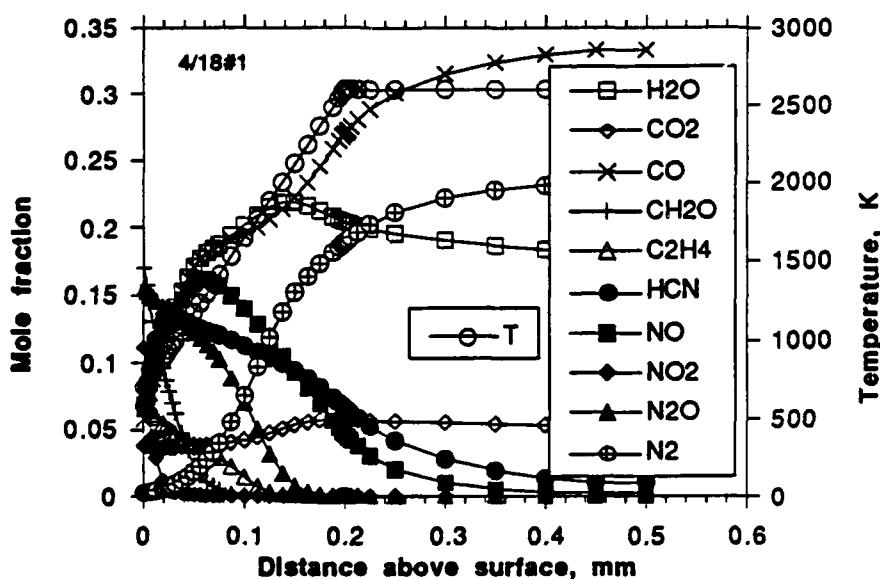
Figure 94. **Results of model for propellant HMX1, 15 atm.** Miller-Bowman mechanism; HMX → 2 CH_2O + 2 H_2CN + 2 N_2O + 2 NO_2.
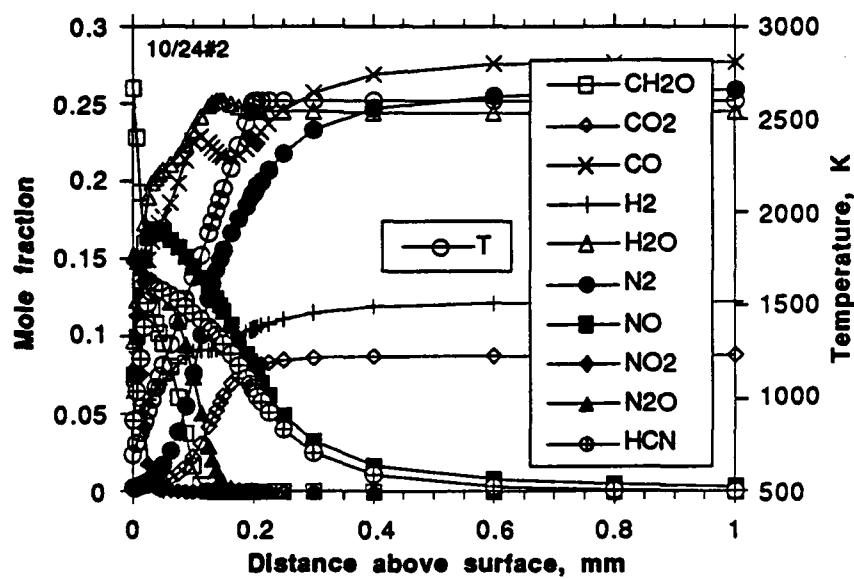
Figure 95. Results of model for propellant HMX1, 15 atm. Hatch mechanism;
HMX → 2 CH_2O + 2 H_2CN + 2 N_2O + 2 NO_2.
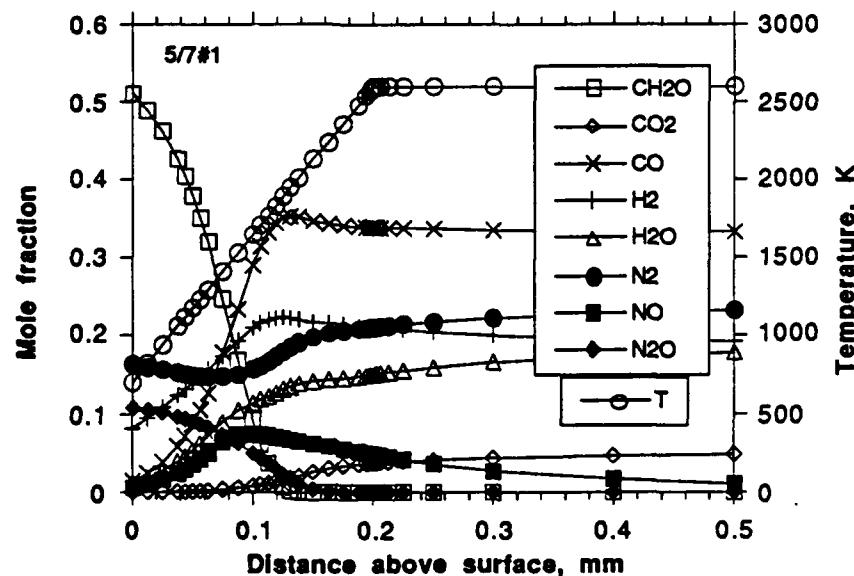
Figure 96. Results of model for propellant HMX1, 15 atm. Hatch mechanism;
HMX → 4 CH_2O + 2 N_2 + 4/3 N_2O + 4/3 NO_2.

To assess the utility of the model predictions, they must be compared to experimental data. For propellant HMX1, the absorption data of Vanderhoff [12], the CARS data of Stufflebeam [13], and the CN LIF profile [4,5] can be compared with the model predictions. As mentioned previously, the temperature profile used in the modeling comes from the absorption data of Vanderhoff [12]. In CARS experiments at 23 atm, Stufflebeam measured the concentration of N_2, CO, H_2 and temperature in an HMX1 propellant flame at distances about 1 mm and greater above the surface [13]. In absorption experiments at 20 atm, Vanderhoff measured the concentration profiles of CN, NH, and OH [12]. Compared to LIF experiments, the absorption experiments have the advantage of yielding absolute concentrations, rather than relative concentration profiles. The spatial and temporal resolution and sensitivity of LIF is potentially greater than that of absorption, however. The experimental work at the Astronautics Laboratory has focussed on measurements of species and temperature profiles using LIF. Laser-Raman scattering with a 308 nm laser was attempted for major species and temperature measurements, but was unsuccessful due to large LIF interferences. Previous work has demonstrated fairly successful CN and OH profile measurements in several propellants at pressures up to 3.5 MPa (500 psi) [4,5]. OH LIF temperature measurements were generally unsuccessful because of the conflicting requirements of wide detection bandpass and high scattered light rejection (see earlier section), although wide bandpass OH LIF temperature measurements were successfully made at NWC in atmospheric pressure laser-supported propellant flames even in metallized propellants [10]. One common aspect to all these measurements is that successful data collection below about 0.2 mm above the surface is rare, due to surface attenuation of laser and absorption beams.

The published CARS measurements are of major species above about 1 mm. These measurements should agree with the model since they reflect the equilibrium flame conditions. Any differences are due to problems with the stoichiometry when using the Hatch mechanism [7,8]. However, the radical measurements should be sensitive to the model assumptions. For example, the CN measurements are compared with the four modeling cases in Figures 97 and 98. In Figure 97, it can be seen that the Kubota HMX stoichiometry appears to be totally inconsistent with the experimental data [7,8]. However, in Figure 98, where the binder is allowed to form C_2H_4, it can be seen that the Kubota stoichiometry actually gives closer agreement to the experimental data than the other case. This is because of the interaction of the CH_x species with the NO_x species in the Miller-Bowman mechanism to form CN (Appendix 2). This demonstrates that CN formation requires either the presence of CH_x species (not found in a flame where the only fuel is CH_2O [52]) or the presence of HCN. From the measurements of Parr [10], it is apparent that CN is present in pure HMX flames, so it still seems unlikely that Kubota's stoichiometry is correct. However, the presence of CN in CH_2O/NO_2 flames has led to speculations about CN formation through the reaction of HCO with NO and N_2O [52], so this is still an area of uncertainty. Another interesting point that is seen in Figures 93-96 is that the Hatch mechanism consistently predicts slower conversion of species to final products.

Comparisons of the NH absorption data with the model are found in Figures 99 and 100. The NH data is less informative than the CN data because the predictions of the various models are similar. OH comparisons are shown in Figures 101 and 102, and are also less interesting than the CN data because OH acts as an equilibrium (product) species, rather than a

"reaction zone" species as do NH and CN. The behavior of other species in this flame is quite interesting, as shown in Figures 103 (Hatch mechanism) and 104 (Miller-Bowman mechanism).
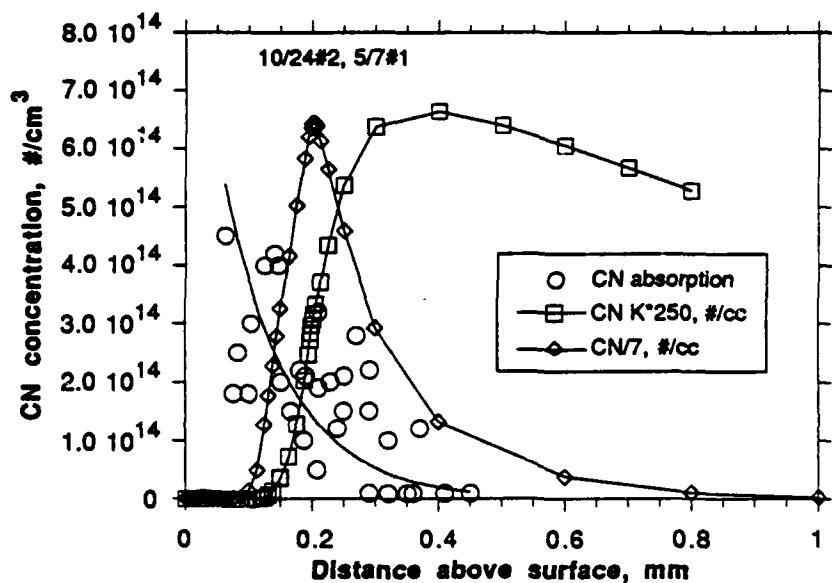
Figure 97. Comparison of experimental data and model results for CN in HMX1, 15 atm. Hatch mechanism; "CN"=HMX → 2 CH_2O + 2 H_2CN + 2 N_2O + 2 NO_2, "CN K"=HMX → 4 CH_2O + 2 N_2 + 4/3 N_2O + 4/3 NO_2.
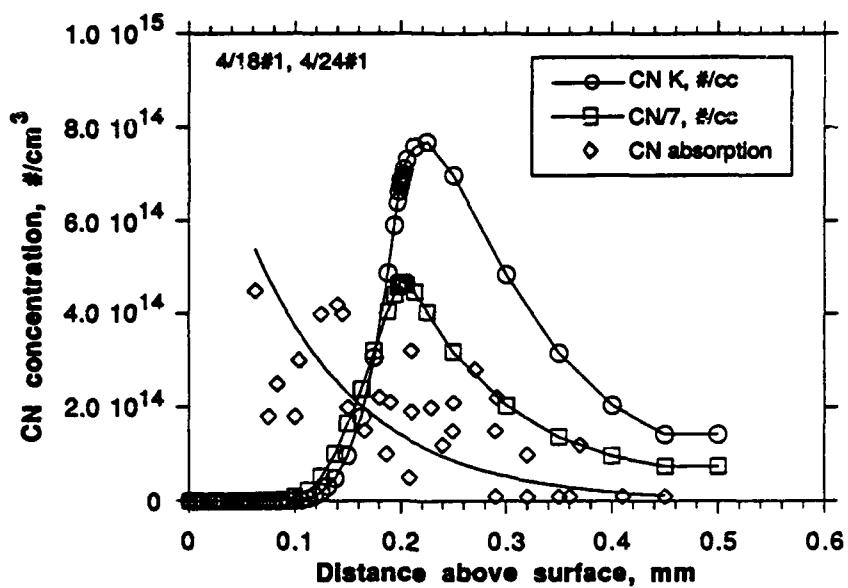
Figure 98. Comparison of experimental data and model results for CN in HMX1, 15 atm. Miller-Bowman mechanism; "CN"=HMX $\rightarrow$ 2 CH_2O + 2 H_2CN + 2 N_2O + 2 NO_2, "CN K"=HMX $\rightarrow$ 4 CH_2O + 2 N_2 + 4/3 N_2O + 4/3 NO_2.
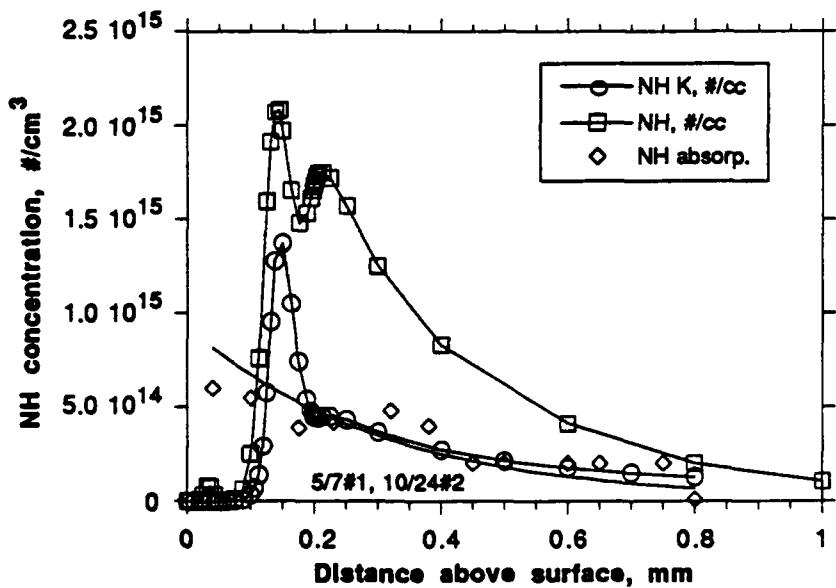
Figure 99. Comparison of experimental data and model results for NH in HMX1, 15 atm. Hatch mechanism; "NH"=HMX $\rightarrow$ 2 CH_2O + 2 H_2CN + 2 N_2O + 2 NO_2, "NH K"=HMX $\rightarrow$ 4 CH_2O + 2 N_2 + 4/3 N_2O + 4/3 NO_2.
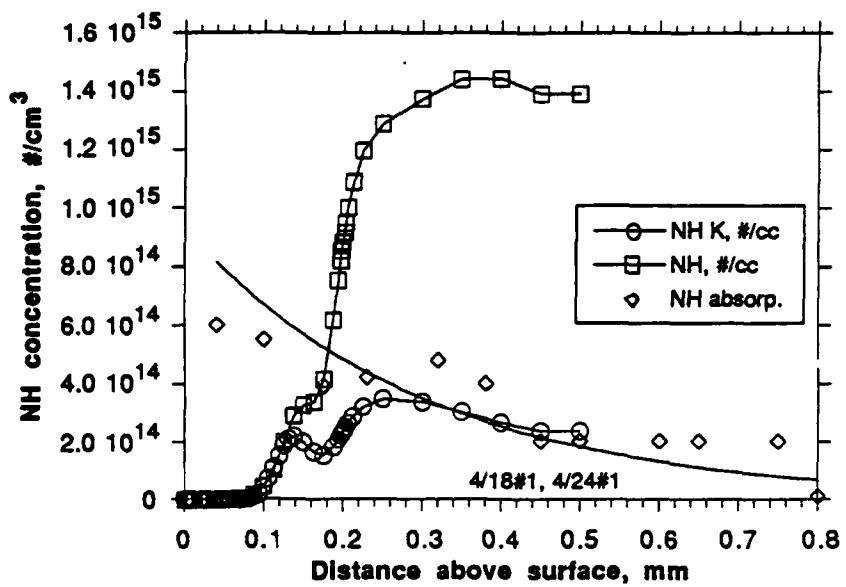
Figure 100. Comparison of experimental data and model results for NH in HMX1, 15 atm. Miller-Bowman mechanism; "NH"=HMX $\rightarrow$ 2 CH_2O + 2 H_2CN + 2 N_2O + 2 NO_2, "NH K"=HMX $\rightarrow$ 4 CH_2O + 2 N_2 + 4/3 N_2O + 4/3 NO_2.
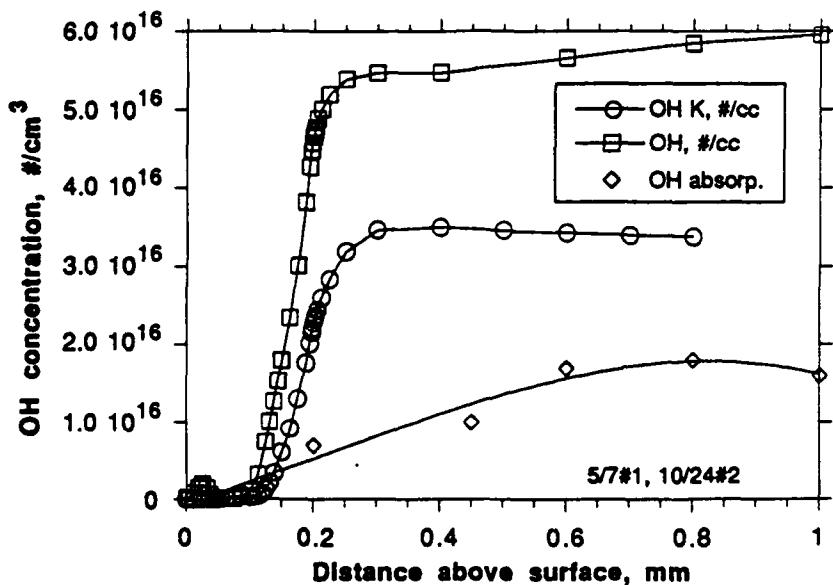
Figure 101. Comparison of experimental data and model results for OH in HMX1, 15 atm. Hatch mechanism; "OH"=HMX $\rightarrow$ 2 CH_2O + 2 H_2CN + 2 N_2O + 2 NO_2, "OH K"=HMX $\rightarrow$ 4 CH_2O + 2 N_2 + 4/3 N_2O + 4/3 NO_2.

85
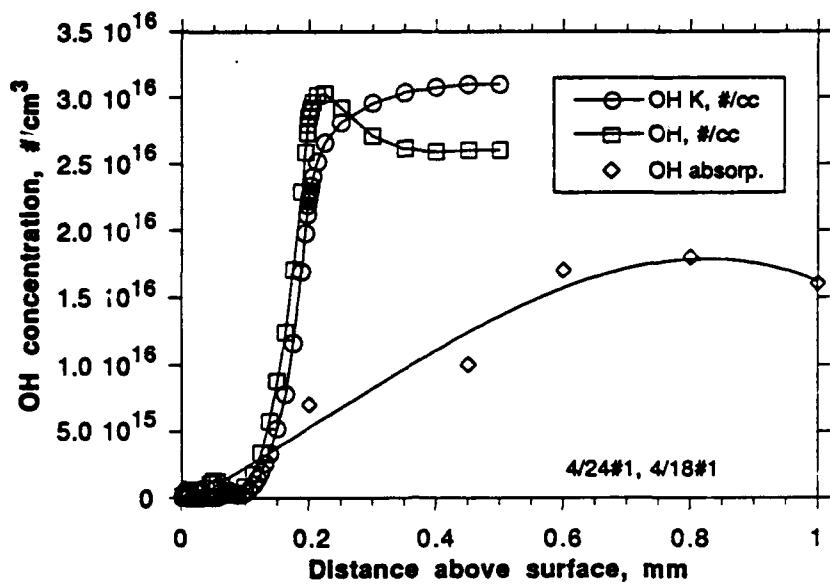
Figure 102. Comparison of experimental data and model results for OH in HMX1, 15 atm. Miller-Bowman mechanism; "OH"=HMX $\rightarrow$ 2 CH_2O + 2 H_2CN + 2 N_2O + 2 NO_2, "OH K"=HMX $\rightarrow$ 4 CH_2O + 2 N_2 + 4/3 N_2O + 4/3 NO_2.
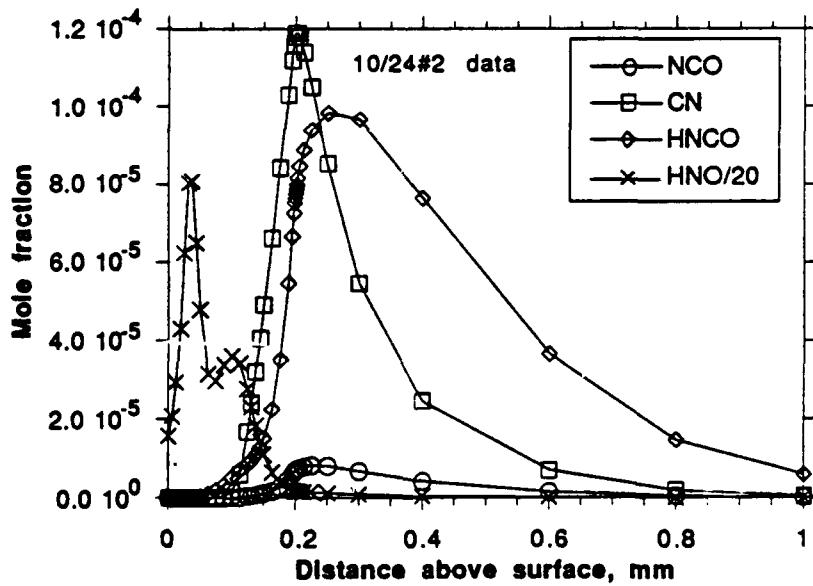
Figure 103. Radical profiles for HMX1, 15 atm. Hatch mechanism; HMX $\rightarrow$ 2 CH_2O + 2 H_2CN + 2 N_2O + 2 NO_2.
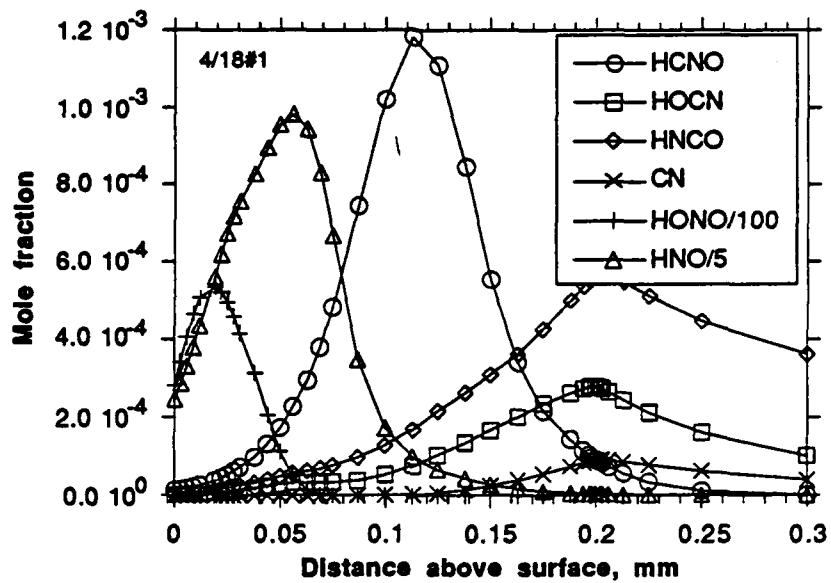
Figure 104. Radical profiles for HMX1, 15 atm. Miller-Bowman mechanism; HMX → 2 CH_2O + 2 H_2CN + 2 N_2O + 2 NO_2.

HMX2 PROPELLANT

For propellant HMX2, the probe sampling measurements of Kubota [40] and the CN profile (using LIF) of Edwards [4,5] can be compared to model predictions. Kubota's probe sampling measurements were taken in two zones of the HMX2 flame at 20 atm, the "preparation zone" and the luminous flame [40]. Products were apparently analyzed by GC. This type of analysis precludes the measurement of reactive species such as NO_2, showing NO, N_2, N_2O, CO, CO_2, H_2, and "hydrocarbons." It is not clear that HCN would be seen by such a detection system.

The results for the four cases for propellant HMX2 are illustrated in Figures 105-108. The model temperature profile is taken from Kubota [40]. Kubota defined the relatively constant temperature region from 0.5 to 1 mm as the preparation zone, with the luminous flame beginning at the rapid temperature increase at about 1 mm above the surface. The complexity of the propellant chemistry is apparent, with several "reaction zones" definable. Near the surface, H_2CN (not shown, profile indistinguishable from NO_2 profile) and NO_2 rapidly react, forming HCN and NO. CH_2O reacts less rapidly, persisting out to 0.5 mm with the Hatch mechanism. The most striking feature is the lack of HCN reaction predicted in Figures 105 and 107 for the HMX → 2 CH_2O + 2 H_2CN + 2 N_2O + 2 NO_2 pathway, even at the

87

adiabatic flame temperature. Under these flame conditions, HCN is less reactive than NO, which is consumed in the luminous flame. It has generally been found that HCN is less reactive than CH_2O in NO_2 oxidized environments [66]. If correct, this large (in both spatial and absolute concentration) HCN level should be accessible with CARS [13].

There are two data sets for propellant HMX2 that can be used for model testing. The first set is the probe results of Kubota [40]; the second data set is the CN LIF profile [4,5]. In Kubota's experiment, GC (?) samples were extracted from the luminous flame and the "preparation zone" (the nonluminous zone between the surface and the luminous flame) of an HMX flame at 20 atm. The two zones can be seen in the temperature profile as the flat regions at about 0.5 mm above the surface (preparation zone) and above 1.5 mm above the surface (luminous flame) at 30 atm. The probe data are at 20 atm and the temperature profile was measured at 30 atm. For comparison, I assumed probe measurements at 30 atm would be the same as those at 20 atm. Kubota's results are shown in Table 13. The luminous flame results are very close to the predicted equilibrium species concentrations, as is the temperature measured by microthermocouples. In the preparation zone, Kubota found large amounts of NO and N_2O, as well as "hydrocarbon fragments and solid carbon generated at the burning surface" [40]. Since the Hatch mechanism described in this paper doesn't include hydrocarbons (CH_2O is not a "hydrocarbon" in the strict sense of the word), matching this last observation is impossible for this mechanism. However, it was also found that the model could not match several of the other observations for either mechanism. The only adjustable parameters in the model are the starting species. Two inconsistencies were found. First, when significant amounts of HCN were formed by assuming the $H_2CN/CHO_2/NO_2/N_2O$ pathway in the model, the HCN persisted even through the luminous flame. Second, if the $CH_2O/N_2O/NO_2/N_2$ (Kubota) pathway was assumed, then very little NO was predicted in the preparation zone since the $CH_2O/N_2O/NO_2/N_2$ pathway doesn't form large amounts of NO compared to the other pathway. Several explanations for these discrepancies are possible. First, the slow reaction of HCN at this propellant's relatively low flame temperature may be due to missing HCN-consuming reactions in the mechanism (although both mechanisms show the lack of HCN reaction). At the higher temperatures found in propellant HMX1, HCN is not predicted to survive the luminous flame (as shown in the previous section). Second, Kubota's temperature profile may be wrong. Microthermocouple measurements in propellant flames are not trivial, although it seems likely that the the observation of two zones in these slow-burning, fuel-rich propellants is correct. Third, it is conceivable that the gas sampling system may have destroyed HCN and NO_2 present in the sample, thus incorrectly implying their absence. Fourth, the initial species assumptions may be wrong.

One problem with the Kubota stoichiometry is that the mechanism forming the products is not clear. The H_2CN/NO_2 mechanism (gas phase HMX decomposition) is supported by quantum mechanical calculations [59] and experiments [47], while the condensed phase CH_2O/N_2O pathway is supported by many slow heating rate, condensed phase experiments [67] and the presence of CH_2O and N_2O in high thermolysis experiments [47]. HCN has been detected in HMX propellant combustion with CARS, although the amount has not yet been quantified [13]. Thus it seems unlikely that CH_2O is the only fuel molecule formed. It also seems likely that the high pressures of the propellant combustion involve extrapolating the known rate constants well beyond their validated range. Thus the lack of agreement between

88

the experimental data and the model is not necessarily an indication that the model is wrong, but rather indicates where improvements in understanding the model and experiments are needed. One partial confirmation of the model is found in CN LIF profiles in propellant HMX2. As shown in Figures 109 and 110, the experimental data shows a broad (but weak) CN peak at a relatively large distance from the propellant surface [4,5]. The models show that even though large amounts of HCN are present in the model flame, the CN concentration is very low because of the low temperature. The CN that is present is "equilibrium" CN in the luminous flame, rather than "reaction zone" CN as is normally seen in flames. The experimental data appears to confirm this, both in the low intensity (concentration) and lack of a peak near the surface. However, the data has a very low signal-to-noise ratio, so this is only a partial confirmation until better data is collected.
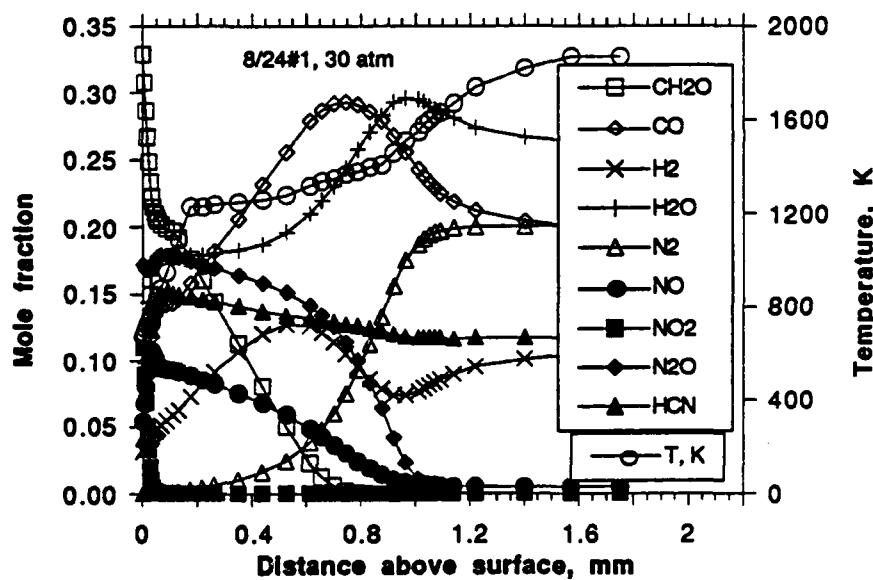
Figure 105. Results of model for propellant HMX2, 30 atm. Hatch mechanism; HMX → 2 CH₂O + 2 H₂CN + 2 N₂O + 2 NO₂ (case #1).

HMX $\rightarrow$ 2 CH$_2$O + 2 H$_2$CN + 2 N$_2$O + 2 NO$_2$ (case #1).
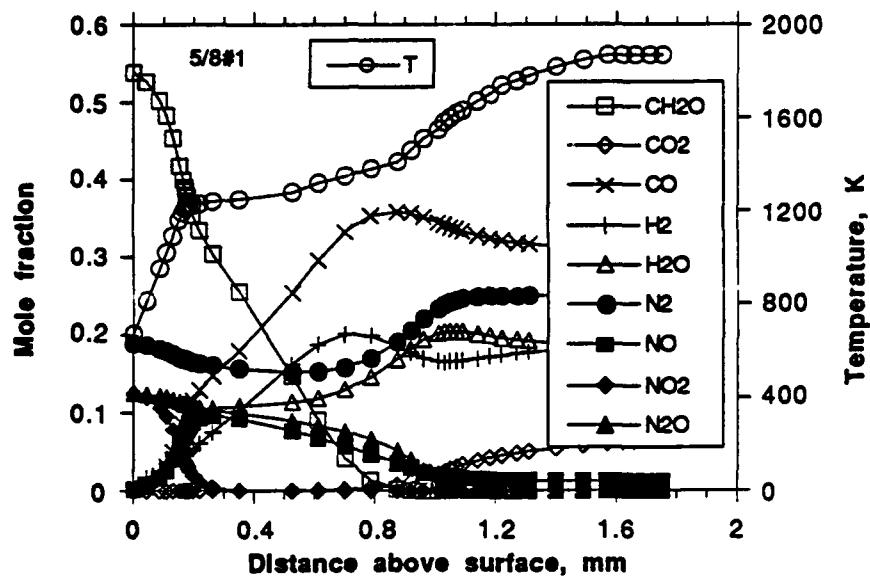
Figure 106. Results of model for propellant HMX2, 30 atm. Hatch mechanism; HMX → 4 CH₂O + 2 N₂ + 4/3 N₂O + 4/3 NO₂ (case #2).
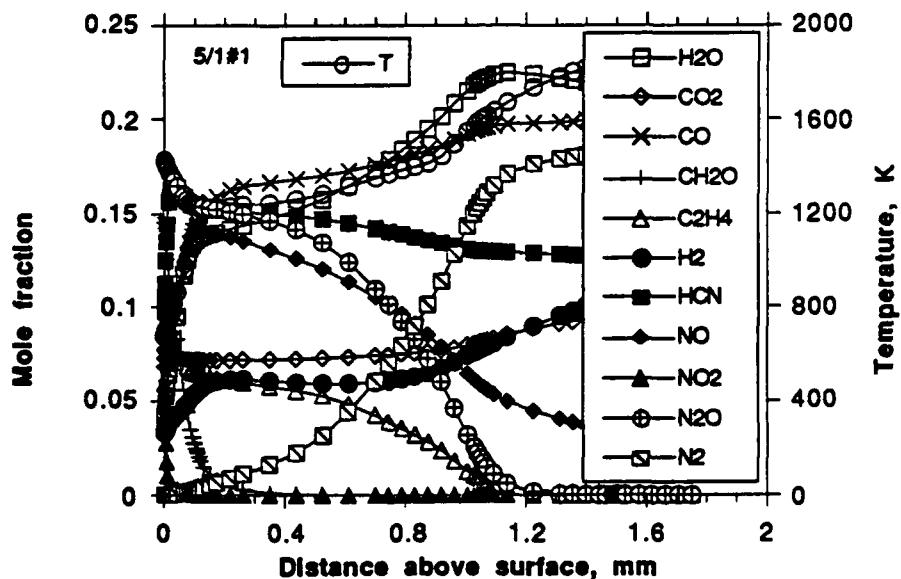
Figure 107. Results of model for propellant HMX2, 30 atm. Miller-Bowman mechanism; HMX → 2 CH₂O + 2 H₂CN + 2 N₂O + 2 NO₂ (case #3).
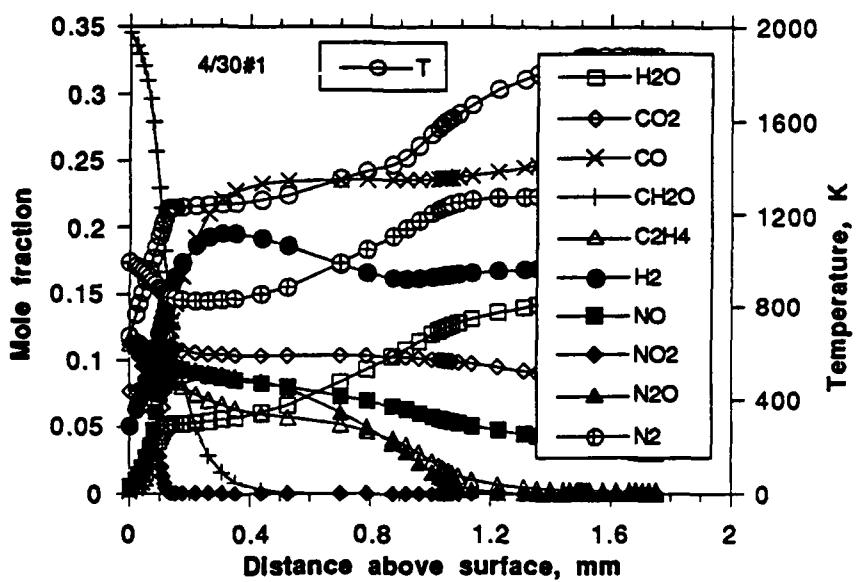
Figure 108. Results of model for propellant HMX2, 30 atm. Miller-Bowman mechanism; $HMX \rightarrow 4\ CH_2O + 2\ N_2 + 4/3\ N_2O + 4/3\ NO_2$ (case #4).

Table 13. Kubota probe results for prop. HMX2 (20 atm) (mole fractions, H_2O-free basis) [40].

SPECIES	"PREP. ZONE" 0.5 mm EXPT	"LUMINOUS FLAME" 1.75 mm EXPT	EQ CODE
NO	0.210	---	---
N_2	0.098	0.228	0.245
N_2O	0.068	---	---
CO	0.180	0.422	0.420
CO_2	0.073	0.041	0.032
H_2	0.067	0.267	0.303
"HC + C_s"	0.304	---	---
T, K	1280	1870	2080

Table 14. Model results at 30 atm for propellant HMX2 (mole fractions, H_2O-free basis). Case #'s listed in legends of Figures 105-108.

Species	Case #1		Case #2		Case #3		Case #4	
	0.5 mm	1.75 mm	0.5 mm	1.75 mm	0.5 mm	1.75 mm	0.5 mm	1.75 mm
NO	0.073	0.006	0.087	0.015	0.143	0.029	0.086	0.036
N_2	0.030	0.273	0.171	0.307	0.038	0.240	0.166	0.265
N_2O	0.188	--	0.100	--	0.160	--	0.085	----
CO	0.318	0.271	0.287	0.373	0.202	0.267	0.252	0.316
CO_2	0.003	0.149	0.001	0.077	0.087	0.122	0.110	0.089
H_2	0.158	0.141	0.184	0.228	0.070	0.141	0.199	0.204
HCN	0.167	0.159	--	--	0.175	0.155	0.0002	0.019
CH_2O	0.062	--	0.167	--	0.0001	--	0.0006	----
HC*	--	--	--	--	0.070	0.028	0.064	0.079

* primarily C_2H_4, C_2H_2
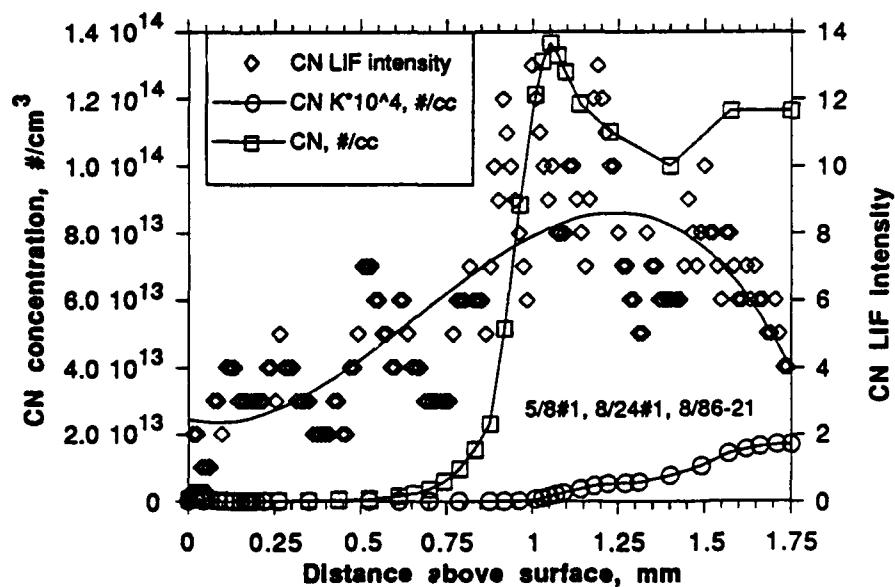
Figure 109. Comparison of CN LIF profile and modeling data. HMX2, 30 atm, Hatch mechanism.
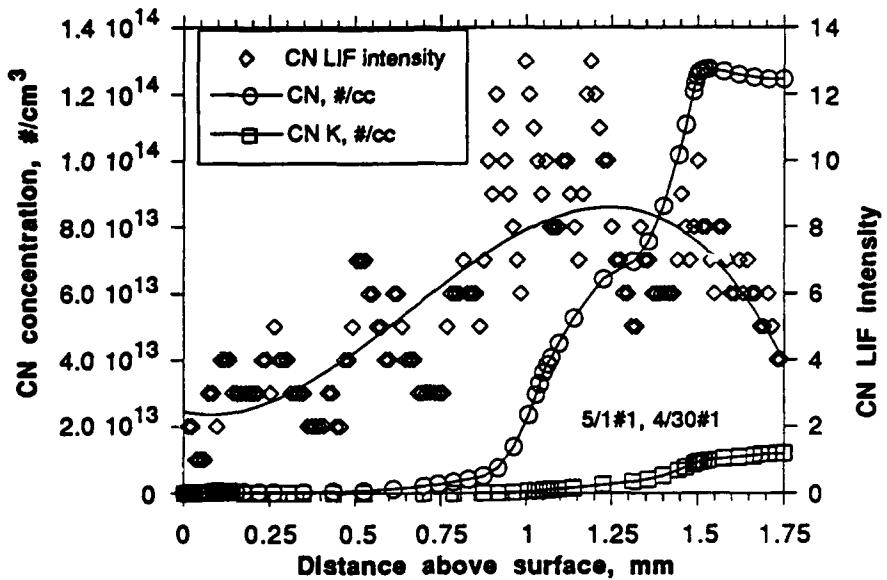
Figure 110. Comparison of CN LIF profile and modeling data. HMX2, 30 atm, Miller-Bowman mechanism.

AN1 PROPELLANT

Recently, temperature profiles for an AN propellant flames have became available [69]. This allows chemical kinetic modeling of the AN propellant flame chemistry, similar to that performed for HMX propellants. There is less experimental data available for AN propellants, due to experimental difficulties. AN propellant flames are very "sooty," and are thus difficult to probe with laser diagnostics [4,5]. Thus, comparing these modeling predictions with experimental data will be difficult.

The temperature profile used was taken from microthermocouple measurements [69]. The experimental data for 15 atm is shown in Figure 111. The data in Figure 111 is from thermocouples made from 75 μm wire (Pt/Pt-13%Rh) with a bead size of approximately 200 μm. Measurements with smaller wire are planned. This is the same size wire as that used by Kubota for his published temperature profiles in HMX propellants [40]. Smaller thermocouples may indicate a more rapid temperature rise above the surface, although the surface temperature and final flame temperature probably will not change significantly. The measured surface temperature of 600 K is in line with other AN burning surface temperature measurements [74].

The first reaction set used was taken from a paper by Hatch [27], which includes 77 reactions involving 26 species. An additional reaction ($HNO_3 \rightarrow NO_2 + OH$) was taken from a paper by Zabarnick [11]. The propellant modeled was an energetic binder AN propellant ("AN1": 67 wt% AN (50% 15 μm, 50% 190 μm), 21 wt% GAP, 12 wt% TMETN), with a burning rate of 0.3 cm/s at 15 atm (0.5 g/cm^{2}s). The following reactions were assumed to happen at the propellant surface for the chemical kinetic calculations:

AN: $NH_4NO_3 \rightarrow NH_3 + HNO_3$

GAP: $C_3H_5N_3O \rightarrow CH_2O + HCN + N_2$

TMETN: $C_5H_9N_3O_9 \rightarrow 3\ CH_2O + 3\ NO_2$
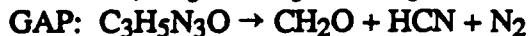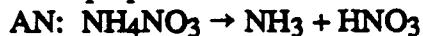
These reactions are the "baseline" case. Note that the Hatch mechanism doesn't include hydrocarbons, so the GAP and TMETN reactions are not stoichiometrically balanced. The baseline stoichiometry for the propellant is then (mole fractions):

AN1 $\rightarrow$ 0.323 NH_3 + 0.323 HNO_3 + 0.082 HCN + 0.082 N_2 + 0.136 CH_2O + 0.054 NO_2. The baseline reactions were postulated based mainly on high rate thermolysis data of Brill [62,70,71]. The model is a premixed model so no diffusion flame effects are currently modeled. Detailed chemical kinetic modeling of diffusion flames is still in its infancy [65].

Species profiles for the baseline stoichiometry with the Hatch mechanism are shown in Figures 112 and 113. The model flame structure is complex, with several "reaction zones" discernable. HNO_3, CH_2O, and part of the NH_3 are seen to react very close to the surface, with the NO_2 formed from the HNO_3 reacting with the remaining NH_3. HCN was not predicted to react very readily at the low temperatures of the AN1 propellant flame. This is consistent with the model predictions in HMX propellant flames. However, the reaction set may not include important HCN consuming reactions. The addition of hydrocarbon reactions to the mechanism will allow better predictions, especially for the GAP binder where Brill found significant amounts of hydrocarbons formed during thermolysis [70].

For comparison, the profiles for a pure AN flame (NH_3/HNO_3=0.5/0.5) of the same T profile and mass burning rate is shown in Figures 114 and 115. The profiles for NH_3, HNO_3, and NO_2 are similar to those in the propellant. Interestingly, the equilibrium O_2 concentration (0.14 mole fraction) is not reached, with relatively equal amounts of O_2 and NO formed as final products. At 15 atm, the equilibrium conditions are T_{fl}=1245 K, $H_2O/O_2/N_2$=0.57/0.14/0.29 mole fractions.

As a rough approximation to the diffusion flame behavior in the propellant, one could assume that the fast reactions involving HNO_3 and NH_3 occur in the monopropellant (AN) flame, with the "leftovers" from that flame reacting with the binder-generated species. For example, assuming that the species profiles at 0.55 mm in Figure 114 are the products from the AN monopropellant flame ($NH_4NO_3 \rightarrow 1.2\ H_2O + 0.25\ N_2 + 0.6\ NH_3 + 0.9\ NO_2$), the chemistry of the AN/binder diffusion flame could be roughly approximated as the flame between the AN monopropellant flame products and the binder pyrolysis products. This leads to a flame (approximated as premixed) with the following stoichiometry: $NO_2/CH_2O/N_2/H_2O/HCN/NH_3$ = 0.264/0.104/0.124/0.297/0.063/0.148. The species profiles from such a flame are shown in Figures 116 and 117. Reactions between the monopropellant flame products and the binder products do not begin until the maximum flame temperature is nearly reached. This indicates that the assumption that the monopropellant

94

products and the binder products have time to mix may not be unrealistic. This stoichiometry may be compared with the "secondary reaction" products seen by Brill from AN thermolysis (HNO$_3$ and NH$_3$ are the initial products seen) : NH$_4$NO$_3$ → 0.68 H$_2$O + 0.24 NH$_3$ + 0.6 H$_2$ + 0.96 NO$_2$ + 0.4 N$_2$O. This stoichiometry was estimated from Brill's data which did not include H$_2$O, H$_2$, N$_2$, or O$_2$.

Alternatively, one could assume that the AN reacted mostly in the liquid phase: NH$_4$NO$_3$ → 2 H$_2$O + N$_2$O. Then the gas phase reactions would be mostly fuel/N$_2$O reactions. The model predictions for this situation are shown in Figures 118 and 119. The behavior is similar to that shown in Figures 116 and 117 for the monopropellant products/binder flame, with little reaction before about 0.5 mm above the surface (T≈1200 K). This is because the model predicts that N$_2$O is less reactive at low temperatures than HNO$_3$.

AN Propellant, 200 psi
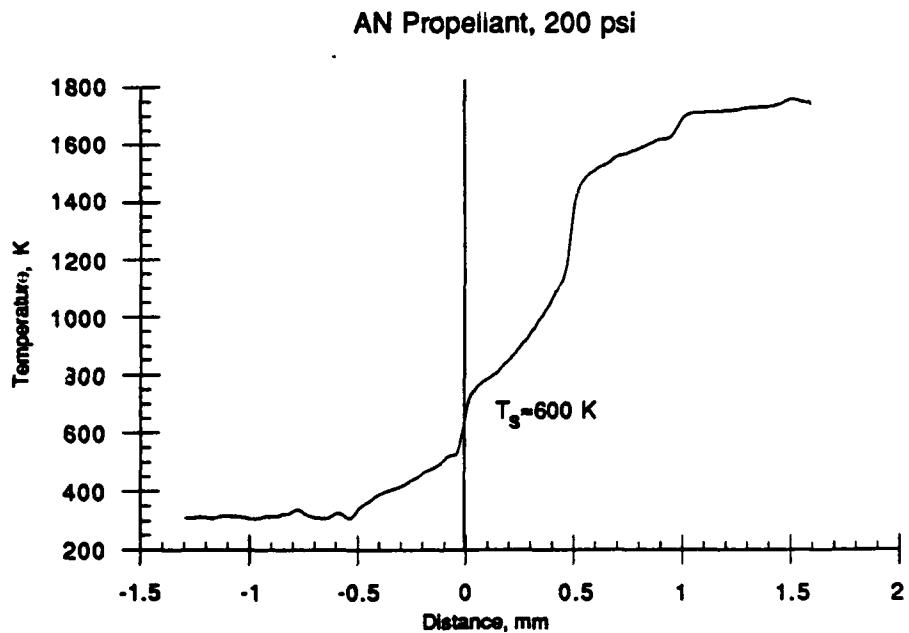
Figure 111. AN1 Propellant Temperature Profile - 15 atm. For model, gas phase T profile approximated as linear between x=0, T=600 K and x=0.9 mm, T=1700 K.

95
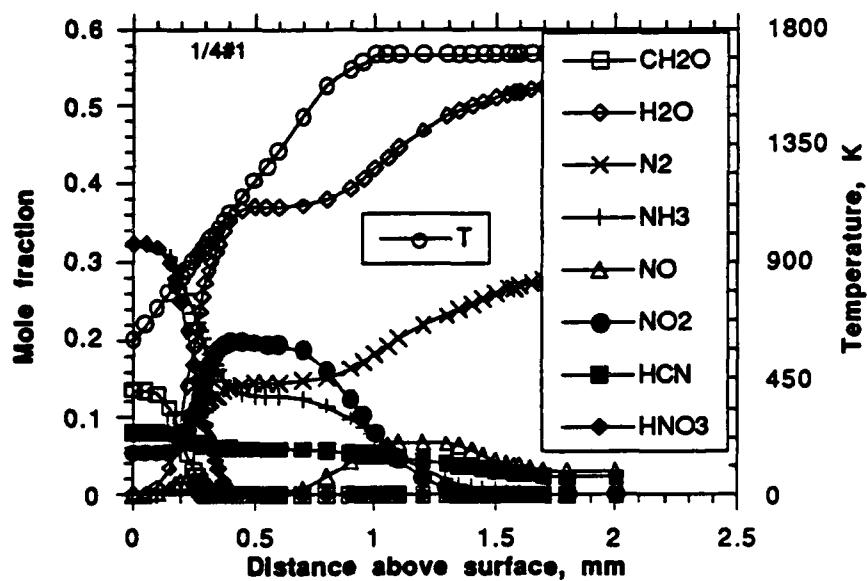
Figure 112. Model results for baseline case, major species.
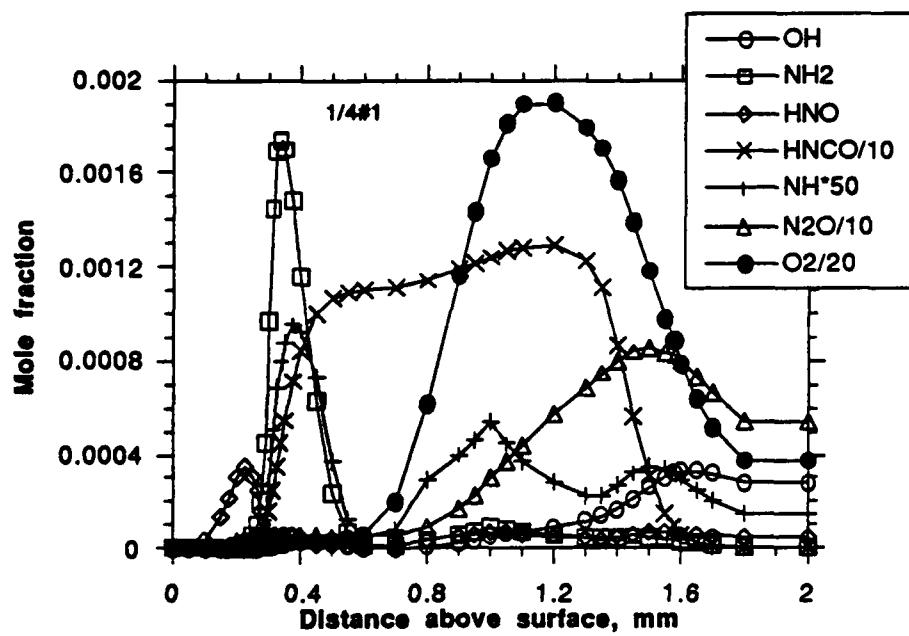
Figure 113. Model results for baseline case, selected minor species.

96
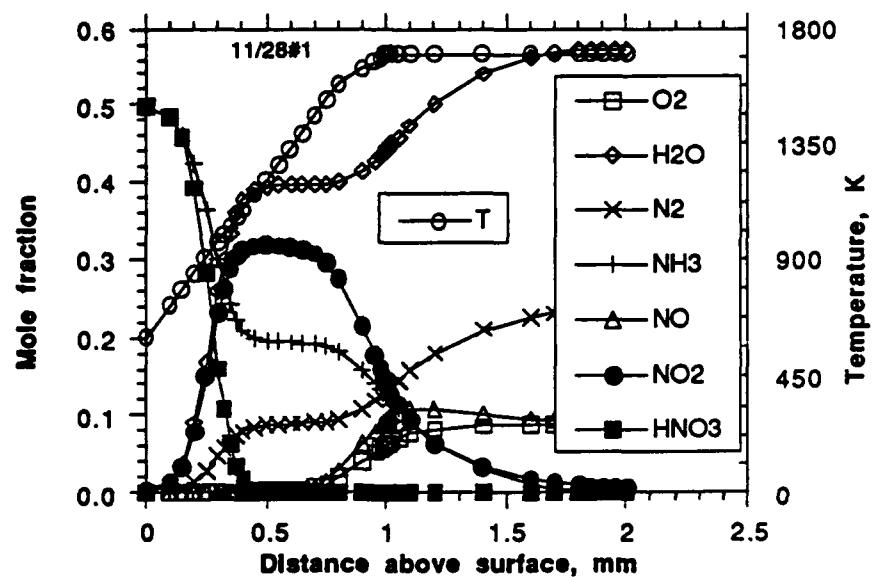
Figure 114. Model results for $NH_3/HNO_3=0.5/0.5$, major species.
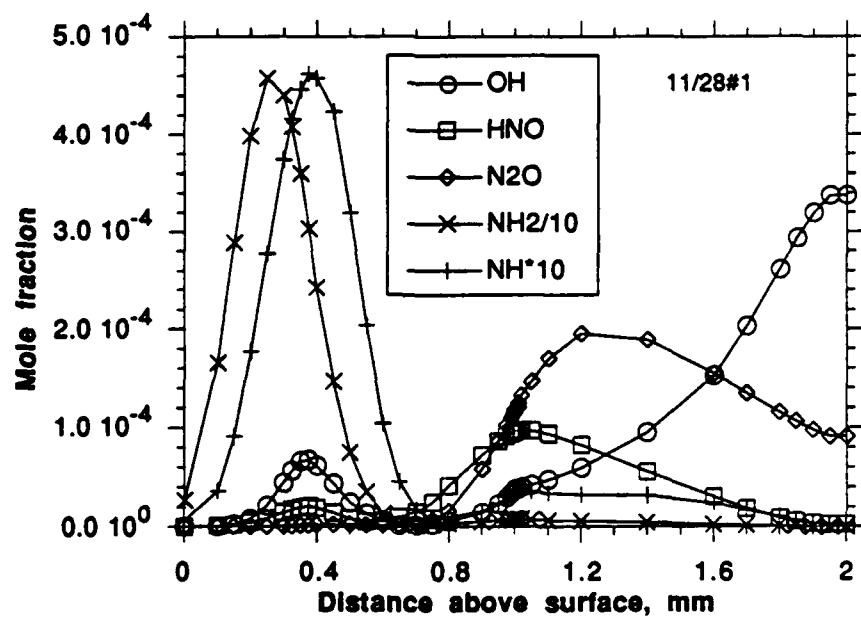
Figure 115. Model results for $NH_3/HNO_3=0.5/0.5$, minor species.
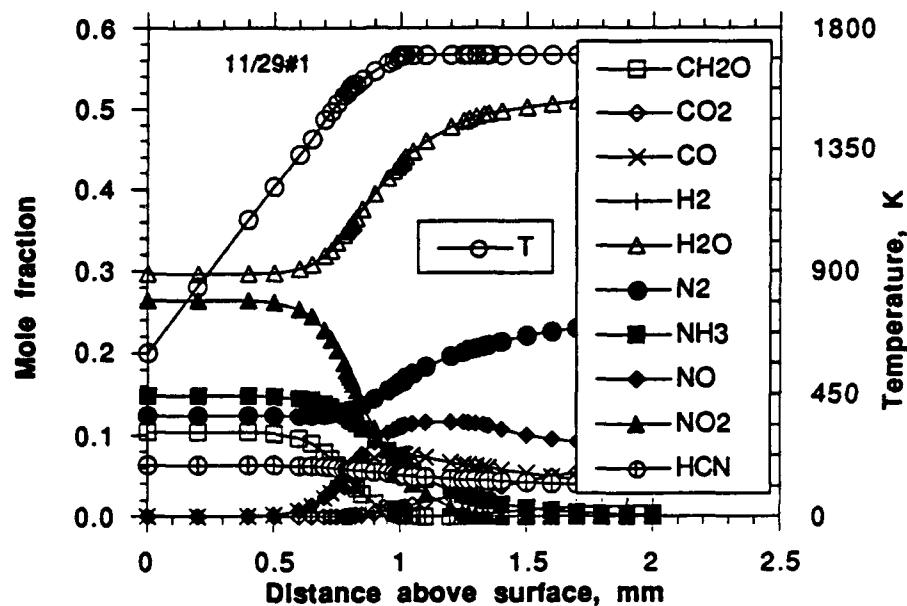
Figure 116. Model results for flame between monopropellant products and binder pyrolysis products, major species.
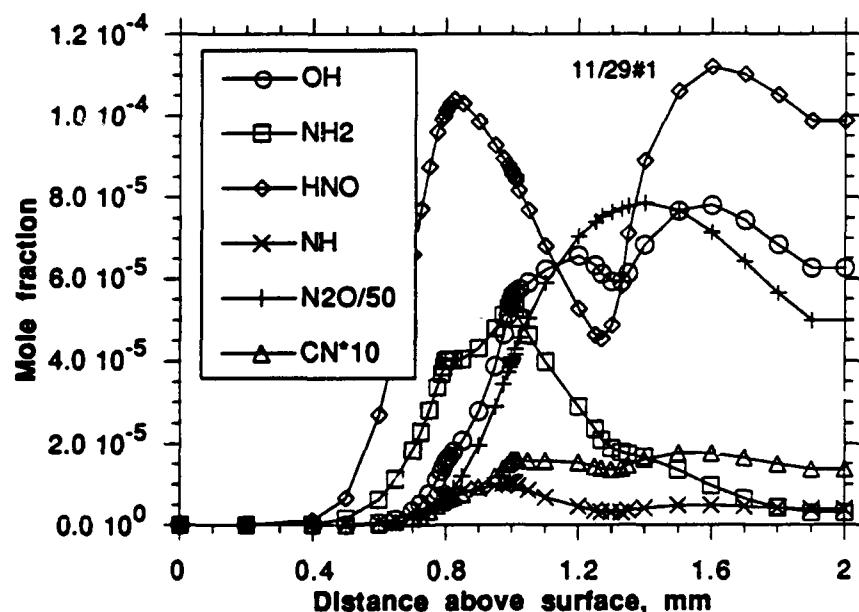
Figure 117. Model results for flame between monopropellant products and binder pyrolysis products, minor species.
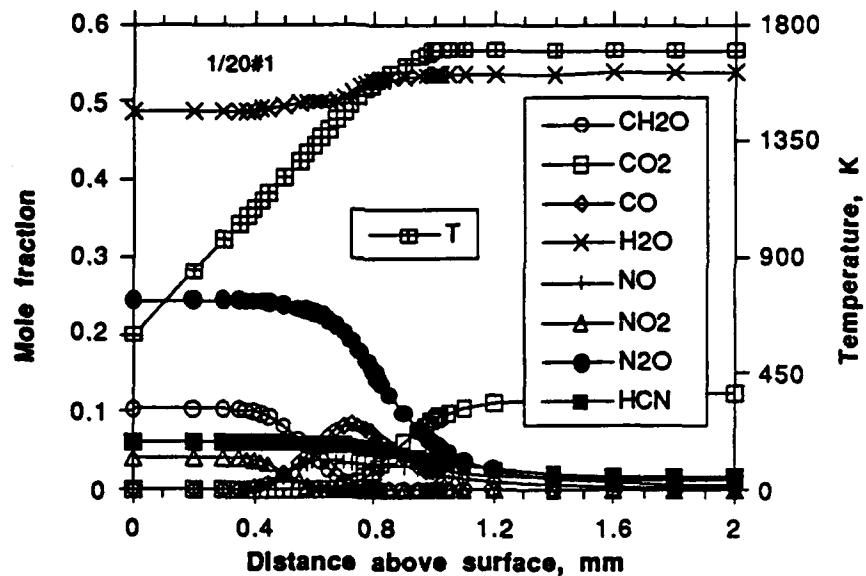
Figure 118. **Model results (major species) for AN propellant flame,** assuming AN → 2 H_2O + N_2O. Binder assumptions same as Figures 112 and 113.
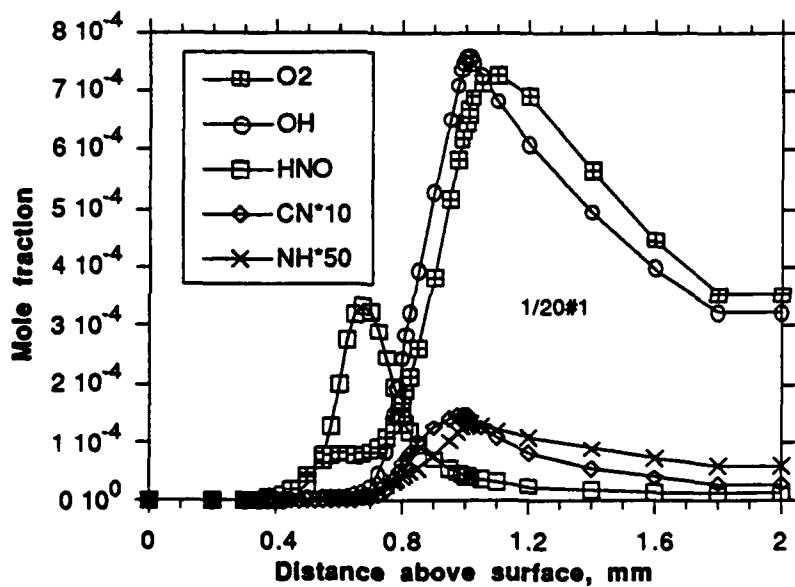
Figure 119. **Model results (minor species) for AN propellant flame,** assuming AN → 2 H_2O + N_2O. Binder assumptions same as Figures 112 and 113.

99

Some very recent modeling of the AN1 propellant has been done with the extended Miller-Bowman mechanism (described in the previous HMX propellant discussions). This mechanism includes hydrocarbons, so the stoichiometry for the various ingredients is somewhat different (but still based on the data of Brill):

AN: $NH_4NO_3 \rightarrow NH_3 + HNO_3$
GAP: $C_3H_5N_3O \rightarrow CH_4 + HCN + N_2 + CO$
TMETN: $C_5H_9N_3O_9 \rightarrow 3\ CH_2O + 3\ NO_2 + C_2H_4$
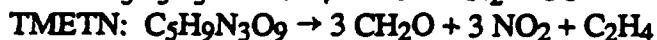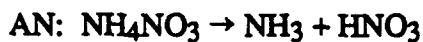
The initial results for this case are shown in Figure 120 (major species) and Figure 121 (minor species). The temperature profile is again that shown in Figure 111. It is evident from these figures that the Miller-Bowman mechanism predicts much more complete reaction close to the surface that does the Hatch mechanism. No intermediate HCN "plateau" is seen, with rapid reactions occurring when the flame temperature reaches about 800 K. For comparison, the species profiles for a NH_3/HNO_3 flame with the same temperature profile are shown in Figures 122 and 123. Again, reactions are rapid, with complete consumption of fuel and oxidizer within 0.4 mm of the surface. These rapid reactions cast some doubt on the multiple reaction zones seen with the Hatch mechanism. For completeness, models with the Hatch stoichiometry should be run with the Miller-Bowman mechanism. At the present time, this has not been done. It may be that the hydrocarbons in the mechanism are responsible for the rapid reactions, rather than the presence of more HCN-consuming reactions.
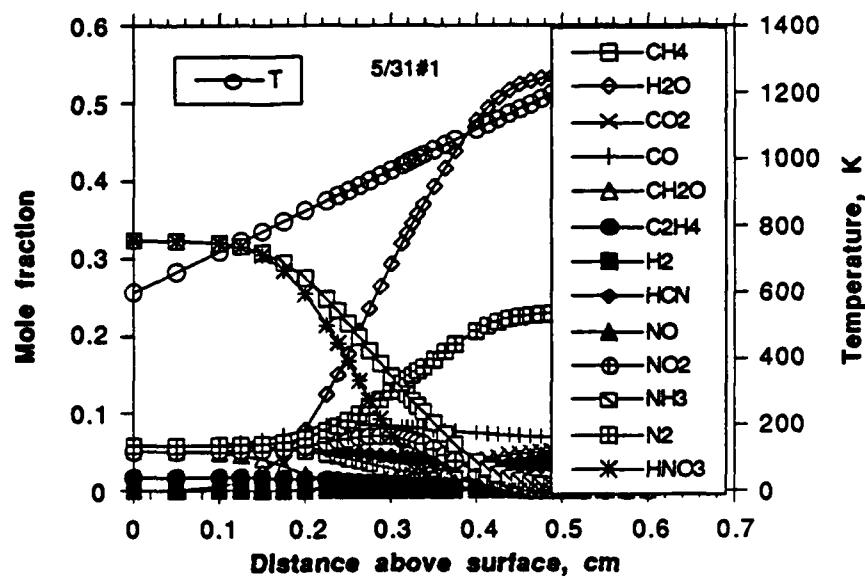
Figure 120. Model results (major species) for AN1 propellant flame, Miller-Bowman mechanism.
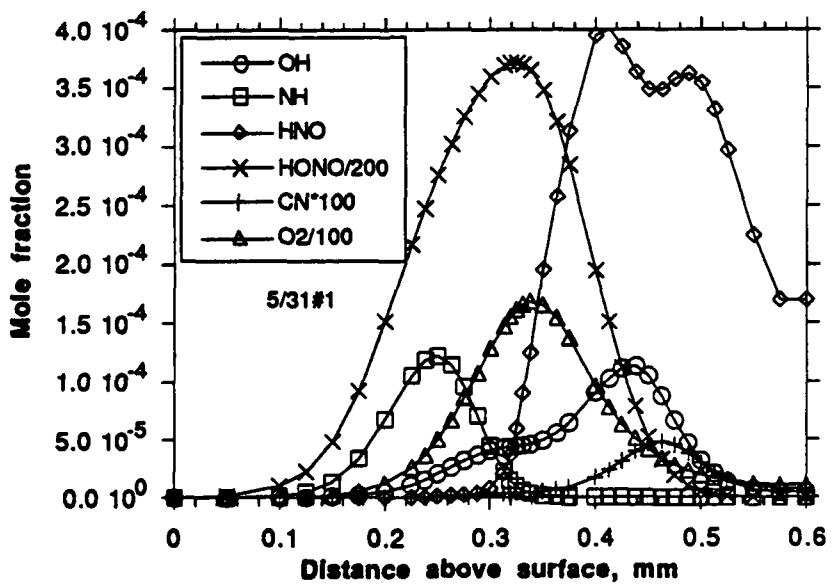
Figure 121. Model results (minor species) for AN1 propellant flame, Miller-Bowman mechanism.

101
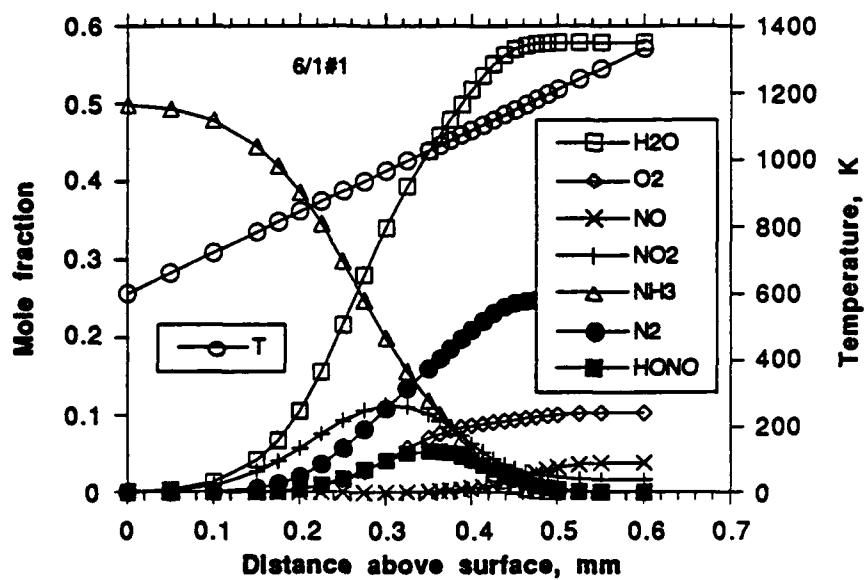
Figure 122. Model results (major species) for AN in AN1 propellant flame, assuming $AN \rightarrow HNO_3 + NH_3$.
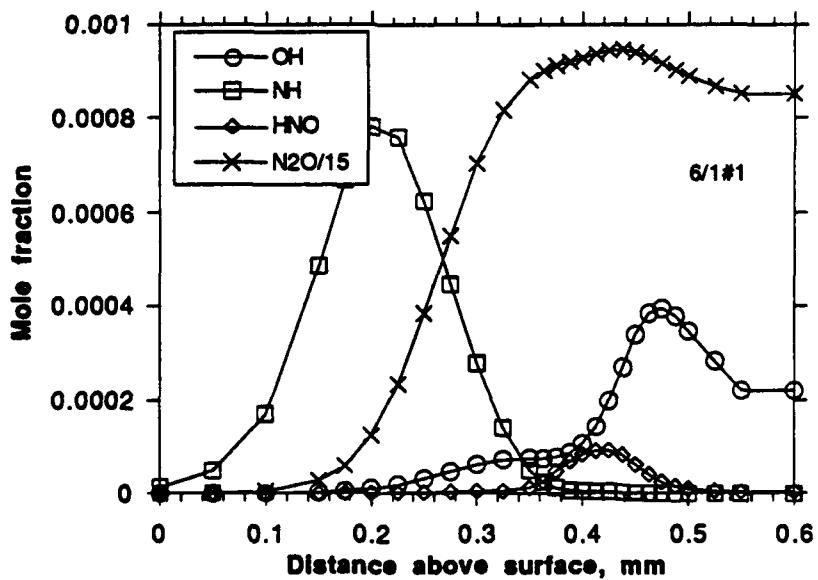
Figure 123. Model results (minor species) for AN in AN1 propellant flame.

Modeling of AN propellant flames using "global" kinetics has been performed by Beckstead [74] using the Separate Surface Temperature (SST) model, the most up-to-date version of the Beckstead-Derr-Price (BDP) model. AN will not burn as a monopropellant at 15 atm so the monopropellant flame is probably not an important part of the propellant combustion chemistry. At 15 atm, the "monopropellant flame height" can be found by extrapolation to be about 700 μm [74]. Thus the combustion is controlled by the diffusion flame between the AN and the binder (the "primary" flame). Beckstead calculates the diffusional distance for the primary flame and multiplies it by 3 to obtain the "primary flame height." The diffusional distance is calculated by a numerical approximation to a Burke Schumann calculation:

$$x^*/b_i = (\gamma_{st}/a1)^{a2}(\alpha_{fi}/\alpha_{oxi})^{a3}$$

where:

b_i=distance from center of oxidizer particle i to center of binder layer surrounding particle

γ_{st}=stoichiometric oxidizer to fuel ratio (mass)

α_{fi}=mass fraction of binder associated with oxidizer fraction i

α_{oxi}=mass fraction of oxidizer associated with oxidizer fraction i

a1,a2,a3=0.834,0.858,1.871 (flame closes over binder)

a1,a2,a3=0.472,0.929,1.604 (flame closes over oxidizer)

For AN propellants, the stoichiometric ratio was calculated assuming the final diffusion flame products were CO and H_2O. Defining the binder as TMETN ($C_5H_9N_3O_9$) + GAP ($C_3H_5N_3O$) yields a fuel $C_{0.87}H_{1.48}N_{0.78}O_{0.64}$. Assuming the AN contributes 0.5 mole O_2/mole AN ($NH_4NO_3 \rightarrow N_2 + 2 H_2O + 0.5 O_2$), the stoichiometric ratio for AN is 0.425 gm binder/gm AN (1.03 mole binder/mole AN), or γ_{st}=2.35 gm AN/gm binder. In other words, NH_4NO_3 + 1.03 $C_{0.87}H_{1.48}N_{0.78}O_{0.64} \rightarrow$ 0.90 CO + 1.40 N_2 + 2.76 H_2O. γ_{st} is about 10 for non-oxygenated (HTPB) binders [74]. The GAP/TMETN binder could also be modeled as an energetic binder with a separate flame. However, heat of explosion (H_{ex}) calculations, with an assumed stoichiometry of binder $\rightarrow$ 0.39 N_2 + 0.64 H_2O + 0.11 H_2 + 0.87 C_s (solid carbon), yield a H_{ex} value of $\approx$800 cal/g. Assuming the products are CO, H_2 and C_s yields a H_{ex} of $\approx$550 cal/g. The 800 cal/g result fits a correlation previously seen between H_{ex} and the adiabatic flame temperature [5], so the 800 cal/g value is probably more correct. With this low H_{ex} value, it was assumed that the energetic binder reactions between the HCN, CH_2O and NO_2 were slow enough that mixing between the AN and the binder products occurred before the energetic binder reactions. Chemical kinetic modeling of possible energetic binder reactions could not be made because of the lack of reactions involving C_s in the mechanism. It is possible that reactions involving C_s are important in AN propellant flames, so a better kinetic model should attempt to include reactions involving C_s. α_{fi} and α_{oxi} were calculated by assuming that the small AN particles burn with a stoichiometric flame, with the large particles burning the remaining fuel. This leads to $(\alpha_{fi}/\alpha_{oxi})_{15\mu m}$=0.425, $(\alpha_{fi}/\alpha_{oxi})_{190\mu m}$=0.56. The amount of binder associated with each particle is needed to calculate b:

$$b = D_i'/2[1+\varphi_{fi}/\varphi_{oxi}]^{0.5},$$

where $D_i' = (2D_i/3)^{0.5}$, a statistical average of the particle diameter (D_i) which changes as the particle burns, and φ_{fi} and φ_{oxi} are the volume fractions of the binder and AN, respectively, calculated from the densities of binder and AN (1.4 and 1.7 g/cm^3) and the propellant composition. These calculations lead to $b_{15\mu m}$=9.3 μm and $b_{190\mu m}$=130 μm. The diffusional distances are then calculated assuming the flame closes over the oxidizer for the 15 μm particles

103

and over the binder for the 190 μm particles [74]. The results are $x^*_{15\mu m}=10$ μm and $x^*_{190\mu m}=110$ μm. In the SST model, these diffusional distances are multiplied by 3 to obtain the "flame height". In Figures 112 and 113, the premixed "flame height" can be estimated as 300-400 μm (very dependent upon the T profile used [7]), whereas the Figures 120 and 121 yield a flame height of about 200 μm. From these calculations, it appears unreasonable to approximate the AN propellant flame as a premixed AN/binder flame at 15 atm since the diffusional distance is of the same order of magnitude as the premixed "flame height", i.e., the AN and binder species must diffuse together before reacting. This analysis could also be made for the more reactive AP propellant flames. For example, SST calculations for a stoichiometric AP/HTPB diffusion flame yield a diffusional distance of $x^*/b_i=0.14$ for large AP particles (flame closes over binder, $\gamma_{st}=5$ (CO), $\alpha_{fi}/\alpha_{oxi}=0.15$), or about 15 μm (maximum) for 200 μm AP particles. Chemical kinetic calculations involving fuel/ClO_x reactions would have to be made to determine if the kinetics or the diffusion controls AP/HTPB primary flames at low ($\approx$15 atm) pressures. Note also that some liquid phase mixing may occur in low-melting, slow-burning AN propellants [74]. Several factors may contribute to the much smaller particle size influence on burn rate for AN propellants versus AP propellants.

If future temperature measurements with smaller thermocouples determine that the temperature profile of Figure 111 is incorrect, with the correct temperature profile reaching the maximum closer to the surface, then the premixed flame approximation becomes more unreasonable. Model predictions using temperature profiles that are "compressed" closer to the propellant surface show that the species profiles are very similar to Figures 112-119, except that the profiles are also compressed in the same ratio as the temperature profile. In other words, the "reaction zone" is still close to the point where the temperature profile reaches its maximum. This is similar to the behavior found in HMX propellant modeling.

There is not a lot of experimental data available on species profiles/concentrations in AN flames or AN propellant flames, especially under combustion conditions. In addition to Brill's high rate thermolysis data [71], there is some laser-pyrolysis/gas analysis data [72]. In the laser pyrolysis experiments, gas analysis from pyrolyzed samples (200 cal/cm^2-s, 50 psi He) of AN yielded roughly equal amounts of NO and N_2, with relatively little N_2O. In contrast, most earlier work found large quantities of N_2O as a product [72]. Apparently, the products of AN decomposition are dependent upon pressure/heating rate, with high heating rates/low pressures yielding NH_3/HNO_3 and low rates/high pressures yielding N_2O/H_2O. Interestingly, the industrial production of N_2O involves the (slow) heating of pure AN to 200 C [73]. Thus, the composition of the gases just above the surface of AN propellants is still in doubt (as it is for HMX propellants).

These model predictions can be used to assess the chances for success of species measurements or to suggest good diagnostic targets. Successful optical diagnostic measurements have been made in high pressure HMX propellant flames, using techniques such as LIF [4,5,7], absorption [12], and CARS [13]. The radical measurements are difficult, with relatively low signal-to-noise ratios in the HMX propellant, and little success has been reported in the more opaque AN propellant flames [4,5]. In Table 15, the model predictions of the concentration of diagnostically accessible (with absorption or LIF) species in AN propellant flames for various assumed stoichiometries are compared with the model predictions for the

HMX propellant flame at 15 atm (for the Hatch mechanism). If the concentration of the particular species is much less than in the HMX propellant flame, the diagnostic results will be difficult to obtain. From Table 15, it can be seen that there is no easy target for species measurements in the AN propellant flame. The radicals (OH, CN, NH, and NO) have concentrations in the AN propellant flame at best equal to that in the HMX propellant flame. This is due to the low temperature and fuel-rich nature of AN propellant combustion. Not coincidentally, these same two characteristics of AN propellant flames lead to poor combustion performance (such as combustion efficiency in aluminized AN propellants) [74]. One interesting difference is in the O_2 concentration, however. O_2 is accessible by LIF [75], and measurements of O_2 concentration in AN propellant flames might help differentiate between the various possible AN decomposition pathways. CARS measurements of major species such as N_2O and NO would also be useful.

Table 15. Comparison of model predictions for HMX and AN propellants at 15 atm.* Hatch mechanism.

	HMX [2]	AN → HNO_3 + NH_3	AN → 2 H_2O + N_2O	AN products/ binder flame
[CN]$_{max}$, #/cm^3	3 X 10^{15}	2 X 10^{14}	1 X 10^{15}	1 X 10^{14}
OH	3 X 10^{16}	2 X 10^{16}	5 X 10^{16}	5 X 10^{15}
NH	2 X 10^{15}	2 X 10^{15}	2 X 10^{14}	7 X 10^{14}
NO	2 X 10^{19}	5 X 10^{18}	3 X 10^{18}	8 X 10^{18}
O_2	9 X 10^{14}	2 X 10^{18}	5 X 10^{16}	1 X 10^{18}

* Concentrations shown are the maximum concentrations predicted by the model. The HMX propellant is 73% HMX, 17% TMETN, and 10% polyester binder ("HMX1") [4,5,7,12,13]. The "AN products/binder flame" is discussed for Figures 114 and 115. The conversion from mole fraction of "A" to absolute concentration (molecules/cm^3, or #/cm^3) is done for each model point using the computed density (temperature dependent): mole fraction (moles A/moles gas) X 6.023×10^{23} (molecules A/moles A) X gas density (gm gas/cm^3) / MW$_{avg}$ (gm gas/mole gas) = #/cm^3. For AN propellants, MW$_{avg}$ was estimated as 23, an average of H_2O and N_2/CO.

SUMMARY AND CONCLUSIONS

Species data in propellant flames is difficult to obtain, especially at higher pressure. However, such data is slowly becoming available, as shown in Table 16. Of the reactive (radical) species, only the diatomics CN, NH, OH, and NO and the triatomic NO_2 (tentative) have been measured. Other important molecules, such as HNO and HCO, have been measured under specialized conditions but are probably not measurable in propellant flames. Stable species in high concentration that have been measured include H_2, CO, and N_2, with HCN identified. Thus, some data is available. This data can be used to validate or improve chemical kinetic models of propellant flames. There is also data available under noncombustion conditions that is very relevant [47,62]. One problem area is that kinetic mechanisms relevant to propellant combustion have not been tested in appropriate flames to determine the accuracy of the parts before inclusion in the complete mechanism. Thus, when experiment differs from model, the problem can either be in the assumptions of the model (e.g., initial gas phase species) or in the reaction mechanism itself (e.g., missing NO_2 reactions). Thus it is important to test the mechanism in well-controlled flames before inclusion in the propellant model. Some mechanism testing of this type is underway (Table 17), but more needs to be done. It may well be that many reaction rates need to (re)measured before successful propellant flame chemical kinetic models are created.

Table 16. Propellant flame species measurements. Most successful measurements usually in nitramine or nitramine composite propellants.

Author	Diagnostic	Species	Reference
Parr, Hanson-Parr	PLIF	CN, NH, OH, NO, NO_2, T	10
Stufflebeam	CARS	N_2, CO, H_2, T	13
Vanderhoff	Absorption	CN, NH, OH, T	12
Edwards	LIF	CN, NH, OH, T	4
Kubota	Probe	NO, N_2, N_2O, CO, CO2, H_2	40

Table 17. Propellant-related flame measurements/modeling

Author	Flame	Reference
Zabarnick	$CH_4/NO_2/O_2$	11
Thorne	HCN/NO_2, C_2N_2/NO_2	53
Branch	$CH_4/NO_2/O_2$, CH_2O/NO_2, CH_2O/N_2O, CH_4/N_2O	52

6.0 REFERENCES

1. Edwards, T., Weaver, D. P., Campbell, D. H., and Hulsizer, S., "A High Pressure Combustor for the Spectroscopic Study of Solid Propellant Combustion Chemistry," Review of Scientific Instruments, Vol. 56, No. 11, pp. 2131-2137, 1985.

2. Edwards, T., Weaver, D. P., Campbell, D. H., and Hulsizer, S., "Investigation of High Pressure Solid Propellant Combustion Chemistry Using Emission Spectroscopy," Journal of Propulsion and Power, Vol. 2, No. 3, pp. 228-236, 1986.

3. Campbell, D. H., Hulsizer, S., Edwards, T. and Weaver, D. P., "High Pressure Solid Propellant Combustion Zone Structure from Analysis of Hydroxyl Radical Chemiluminescence," Journal of Propulsion and Power, Vol. 2, No. 5, pp. 414-422, 1986.

4. Edwards, T., Weaver, D. P., and Campbell, D. H., "Laser-Induced Fluorescence in High Pressure Solid Propellant Flames," Applied Optics, Vol. 26, No. 17, pp. 3496-3509, 1987.

5. Edwards, T., Solid Propellant Flame Spectroscopy, AFAL-TR-88-076, Edwards AFB, CA, August 1988.

6. Edwards, T., OH LIF Temperature Measurements in High Pressure Solid Propellant Flames, AFAL-TR-89-003, Edwards AFB, CA, March 1989.

7. Edwards, T., "Investigation of High Pressure Solid Propellant Flame Chemistry," AIAA Paper 90-0547, presented at AIAA 28th Aerospace Sciences Meeting (January 1990).

8. Edwards, T., "Comparison of Kinetic Modeling and Experimental Measurements in Solid Propellant Flames," paper presented at 26th JANNAF Combustion Meeting, Pasadena, CA (October 1989).

9. Crosley, D. R., and Smith, G. P., "Rotational Energy Transfer and LIF Temperature Measurements," Combustion and Flame, Vol. 44, pp. 27-34, 1982.

10. Parr, T. P., and Hanson-Parr, D. M., "Nitramine Flame Structure as a Function of Pressure," 26th JANNAF Combustion Meeting, October 1989 (in press). Also, Parr, T., and Hanson-Parr, D., "Species and Temperature Profiles in Ignition and Deflagration of HMX, " Western States Section/Combustion Institute Paper WSS/CI 87-8, April 1987. Also, "The Application of Imaging Laser-Induced Fluorescence to the Measurement of HMX and Aluminized Propellant Ignition and Deflagration Flame Structure," 23rd JANNAF Combustion Meeting, CPIA Pub. 457, Vol. I, 249-267 (1986). Also, "Temperature and Species Profiles in Propellant Ignition and Combustion," 24th JANNAF Combustion Meeting, CPIA Pub. 476, Vol. I, 367-382 (1987).

11. Zabarnick, S., "Laser-Induced Fluorescence Diagnostics and Chemical Kinetic Modeling of a $CH_4/NO_2/O_2$ Flame at 55 Torr," submitted to Combustion and Flame. Also, Zabarnick, S., "Investigation of Solid Propellant Combustion," AL-TR-90-014, June 1990 (UDR-TR-89-68).

12. Vanderhoff, J. A., and Kotlar, A. J., "Simultaneous Determination of Temperatures and OH Concentrations in a Solid Propellant Flame," paper to be presented at 23rd Symposium (International) on Combustion, July, 1990. Also, Vanderhoff, J. A., "Spectral Studies of Solid Propellant Combustion: II. Emission and Absorption Results for M-30 and HMX1 Propellants," Technical Report BRL-TR-3055, December 1989. Also, "Spectral Emission and Absorption Studies of Solid Propellant Combustion," 25th JANNAF Combustion Mtg, Vol. IV, CPIA Pub. 498, pp. 537-547, 1988.

13. Stufflebeam, J. H., and Eckbreth, A. C., "CARS Diagnostics of Solid Propellant Combustion at Elevated Pressure," Combustion Science and Technology, Vol. 66, pp. 163-

179, 1989. Also, Stufflebeam, J. H., Temperature and Multiple Species CARS Measurements of Solid Propellant Flames," 26th JANNAF Combustion Meeting, October 1989 (in press). Also, "Stufflebeam, J. H., and Eckbreth, A. C., "Multiple Species CARS Measurements of High Pressure Solid Propellant Combustion," AIAA Paper 89-0060, presented at 27th Aerospace Sciences Meeting, January 1989. Also, Stufflebeam, J. H., "CARS Measurements in Solid Propellant Flames," 25th JANNAF Comb. Mtg, Vol. II, CPIA Pub. 498, pp. 113-122, 1988.

14. Herzberg, G., Spectra of Diatomic Molecules, Van Nostrand Reinhold, New York, 1950.

15. Jevons, W., "The More Refrangible Band System of Cyanogen as Developed in Active Nitrogen," PRS A, 112:407-422 (1926).

16. Engleman, R., "The $\Delta v=0$ and $+1$ Sequence Bands of the CN Violet System Observed During the Flash Photolysis of BrCN," Journal of Molecular Spectroscopy, 49:106-116 (1974).

17. Chidsey and Crosley, "Calculated Rotational Transition Probabilities for the A-X System of OH," JQSRT 23:187-199 (1980).

18. Eckbreth, A. C., Laser Diagnostics for Combustion Temperature and Species, Abacus Press, Kent, UK, 1988.

19. Shea, John D., "The Structure of the Swan Bands," Physical Review, Vol. 30, pp. 825-843, 1927.

20. Gaydon, A. G., and Wolfhard, H. G., Flames: Their Structure, Radiation, and Temperature, 4th Edition, Chapman and Hall, London, 1979.

21. Huber, K. P., and Herzberg, G., Molecular Spectra and Molecular Structure IV. Constants of Diatomic Molecules, 1978.

22. Pearse, R. W. B., and Gaydon, A. G., The Identification of Molecular Spectra, 4th Edition, Chapman and Hall, London, 1975

23. Engleman, R., and Rouse, P. E., "The β and γ Bands of Nitric Oxide Observed During the Flash Photolysis of Nitrosyl Chloride," J. Mol. Spectrosc., 37, 240 (1971).

24. Engleman, R., Rouse, P. E., Peek, H. M., Baiamonte, V. D., "Beta and Gamma Band Systems of Nitric Oxide," LANL Report LA-4364, 1970.

25. Ory, H. A., Gittleman, A. P., and Maddox, J. P., "Franck-Condon Factors for the NO Beta and Gamma baznd Systems," Astrophys. J., 139, 346 (1964).

26. Mallard, W. G., Miller, J. H., Smyth, K. C., "Resonantly enhanced two-photon photoionization of NO in an atmospheric flame," J. Chem. Phys, 76(7), 3483 (1982).

27. Gaydon, A. G., Spectroscopy of Flames, 2nd Edition, Chapman and Hall, London, 1974.

28. Guillaume, P., and Van Tiggelen, P. J., "Spectroscopic Investigation of Acetylene-Nitrous Oxide Flames, 20th Symposium (Int'l) on Combustion, Combustion Institute, Pittsburgh, PA, 1984, pp. 751-760.

29. Hepler, W. A., and Smith, O. I., "Numerical Simulation Study of a Hydrazine/Nitrogen Dioxide Diffusion Flame in a Burke-Schumann Burner," 22nd Symposium (Int'l) on Combustion, Combustion Institute, Pittsburgh, PA, 1989, pp. 1799-1806.

30. Miller, J. A., and Bowman, C. T., "Mechanism and Modeling of Nitrogen Chemistry in Combustion," Progress in Energy and Combustion Science, Vol. 15, pp. 287-338, 1989.

31. Reisler, H., Mangir, M., and Wittig, C., "The kinetics of free radicals generated by IR laser photolysis. I. Reactions of C_2 (a $^3\Pi_u$) with NO, vinyl cyanide, and ethylene," J. Chem. Phys., 71(5), 2109-2117 (1979).

32. Benson, S. W., Thermochemical Kinetics, Wiley-Interscience, New York, 1976.

33. Bertrand, W. T., Cowles, D. G., Smith, L. F., Kidd, P. D., "Spectral and Spatial Radiation from the Plume of a Model Rocket Engine Burning N_2O_4/MMH at High Simulated Altitude," AEDC-TR-76-32, ARO, Inc., Arnold AFS, TN, September 1976.

34. Melius, C. F., ΔH_f data, personal communication.

35. Burke, S. P., and Schumann, T. E. W., "Diffusion Flames," 1st/2nd Symposium on Combustion, pp 2-11, 1965, reprinted from Industrial and Engineering Chemistry, 1928.

36. Reid, R. C., Prausnitz, J. M., and Sherwood, T. K., The Properties of Gases and Liquids, 3rd edition, McGraw-Hill, New York, 1977.

37. Piper, L. G., and Cowles, L. M., "Einstein coefficients and transition moment variations for the NO ($A^2\Sigma^+$-$X^2\Pi$) transition," J. Chem. Phys, 85(5), 2419-2422 (1986).

38. Cohen, N. S., Lo, G. A., and Crowley, J. C., "Model and Chemistry of HMX Combustion," AIAA Journal, Vol. 23, No. 2, pp. 276-282, 1985 (AIAA Paper 83-1195).

39. Cohen, N. S., and Lo, G. A., "Modeling Effects of Composition on the Burn Rates of Nitrate Ester-Based Energetic Binders," 20th JANNAF Combustion Meeting, CPIA Pub. 383, Vol. I, pp. 621-628, 1983.

40. Kubota, N., "Physicochemical Processes of HMX Propellant Combustion," 19th Symposium (Int'l) on Combustion, pp. 777-785, 1983.

41. Yano, Y., Miyata, K., and Kubota, N., "Combustion Wave Structures of AP Composite Propellants," Propellants, Explosives, Pyrotechnics, Vol. 12, 137-140, 1987.

42. Zanotti, C., Colombo, G., Grimaldi, C., Carretta, U., Riva, G., and De Luca, L., "Oscillatory Burning of Composite Propellants Near Pressure Deflagration Limit," Proceedings of the Fifteenth International Symposium on Space Technology and Science, Tokyo, pp. 243-254, 1986.

43. Lengelle, G., Bizot, A., Duterque, J., and Trubert, J. F., "Steady-State Burning of Homogeneous Propellants," Chapter 7 (pp. 361-408) in Fundamentals of Solid Propellant Combustion, (Kuo, K., and Summerfield, M.(eds)), AIAA Progress in Astronautics and Aeronautics Series, Vol. 90, AIAA, New York, 1984.

44. Zenin, A. A., "Structure of Temperature Distribution in Steady State Burning of Ballistite Powder," Fizika Goreniya i Vzryva, Vol. 2, No. 3, pp. 67-76, 1966.

45. Miller, M S., "An Evaluation of Imbedded Thermocouples as a Solid Propellant Combustion Diagnostic," paper presented at 26th JANNAF Combustion Meeting, October 1989.

46. Korobeinichev, O. P., Kuibida, L. V., Orlov, V. N., Tereshchenko, A. G., Kutsenogii, K. P., Mavliev, R. A., Ermolin, N. E., Fomin, V. M., Emel'yanov, I. D., "Mass Spectrometric Probe Study of the Flame Structure and Kinetics of Chemical Reactions in Flames," Mass-Spectrum. Khim. Kinet., pp. 73-93, 1985 (English translation supplied by C. Melius, SNLL).

47. Oyumi, Y., and Brill, T. B., "Thermal Decomposition of Energetic Materials 3. A High-Rate, In Situ, FTIR Study of the Thermolysis of RDX and HMX with Pressure and Heating Rate as Variables," Combustion and Flame, Vol. 62, pp. 213-224, 1985.

48. Sotter, J. G., "Chemical Kinetics of the Cordite Explosion Zone," 10th Symposium (Int'l) on Combustion, Combustion Institute, Pittsburgh, 1965, pp. 1405-1411.

49. Guirao, C., and Williams, F. A., "A Model for Ammonium Perchlorate Deflagration between 20 and 100 atm," AIAA Journal, Vol. 9, No. 7, 1345-1356, July 1971.

50. Kee, R. J., Grcar, J. F., Smooke, M. D., and Miller, J. A., "A Fortran Program for Modeling Steady Laminar One-Dimensional Premixed Flames," Sandia Report SAND85-8240, 1985.

51. Branch, M. C., "Chemical Kinetics of Gas Phase Decomposition Products of Nitramine Propellants," 21st JANNAF Combustion Meeting, CPIA Pub. 412, Vol. I, pp. 409-415, 1984.

52. Branch, M. C., Sadeqi, M. E., Alfarayedhi, A. A., and Van Tiggelen, P. J., "Measurements of the Structure of Laminar, Premixed Flames of $CH_4/NO_2/O_2$ and $CH_2O/NO_2/O_2$ Mixtures," Combustion and Flame, in press (1990).

53. Thorne, L. R., and Melius, C. ., "The Structure of Hydrogen Cyanide-Nitrogen Dioxide Premixed Flames," 26th JANNAF Combustion Meeting (in press), October 1989. Thorne, L. R., and Smith, O. I., "The Structure of Cyanogen-Nitrogen Dioxide Premixed Flames," 25th JANNAF Combustion Meeting, CPIA Pub. 498, Vol. II, pp. 143-153, 1988.

54. Ermolin, N. E., Korobeinichev, O. P., Tereshchenko, A. G., and Fomin, V. M., "Kinetic Calculations and Mechanisms Definition for Reactions in an Ammonium Perchlorate Flame," Fizika Goreniya i Vzryva (Combustion, Explosion, and Shock Waves), Vol. 18, pp. 180-189, 1982 (English translation).

55. Ermolin, N. E., Korobeinichev, O. P., Kuibida, L. V., and Fomin, V. M., "Processes in Hexogene Flames," Fizika Goreniya i Vzryva (Combustion, Explosion, and Shock Waves), Vol. 24, No. 4, pp. 21-29, 1988 (English translation). Also, Ermolin, N. E., Korobeinichev, O. P., Kuibida, L. V., and Fomin, V. M., "Study of the Kinetics and Mechanism of Chemical Reactions in Hexogen Flames," Fizika Goreniya i Vzryva (Combustion, Explosion, and Shock Waves), Vol. 22, pp. 544-553, 1986 (English translation).

56. Combourieu, J., Moreau, R., Hall, A. R., and Pearson, G. S., "Chlorine Dioxide and Perchloric Acid Flames," Combustion Science and Technology (?), Vol. 13, pp. 596-604, Nov. 1969.

57. Hatch, R. L., "Chemical Kinetics Modeling of HMX Combustion," 24th JANNAF Combustion Meeting, CPIA Pub. 476, Vol. I, pp. 383-391, 1987; also 23rd JANNAF Combustion Meeting, CPIA Pub. 457, Vol. I, pp. 157-165, 1986.

58. Melius, C. F., 24th JANNAF Comb. Mtg, Vol. I, pp. 359-366, 1987, and "The Gas-Phase Flame Chemistry of Nitramine Combustion," 25th JANNAF Comb. Mtg, Vol. II, pp. 155-162, 1988.

59. Melius, C., and Binkley, J. S., "Quantum Mechanical Calculations of the Decomposition of Nitramines: Thermochemistry and Reaction Pathways, 23rd JANNAF Combustion Meeting, CPIA Pub. 457, Vol. I, pp. 241-248, 1986.

60. Kubota, N., and Sakamoto, S., "Combustion Mechanism of HMX," Propellants, Explosives, Pyrotechnics, Vol. 14, pp. 6-11, 1989.

61. Trulove, P. C., Chapman, R. D., and Shackleford, S. A., "Deuterium Isotope Effects in the Combustion of Formulated Nitramine Propellants," 24th JANNAF Combustion Meeting, CPIA Pub. 476, Vol. I, pp. 303-308, 1987.

62. Oyumi, Y., and Brill, T. B., "Thermal Decomposition of Energetic Materials 14. Selective Product Distributions Evidenced in Rapid, Real-Time Thermolysis of Nitrate Esters at Various Pressures," Combustion and Flame, Vol. 66, pp.9-16, 1986.

63. Westbrook, C. K., and Dryer, F. L., "Chemical Kinetic Modeling of Hydrocarbon Combustion," Progress in Energy and Combustion Science, Vol. 10, pp. 1-57, 1984.

64. Sabadell, A. J., Wenograd, J., and Summerfield, M., "Measurement of Temperature Profiles through Solid Propellant Flames Using Fine Thermocouples," AIAA Journal, Vol. 3, No. 8, pp. 1580-1584, 1965.

65. Hepler, W. A., and Smith, O. I., "Numerical Simulation Study of a Hydrazine/Nitrogen Dioxide Diffusion Flame in a Burke-Schumann Burner," 22nd Symposium (Int'l) on Combustion, Combustion Institute, Pittsburgh, PA, 1989, pp. 1799-1806.

66. Fifer, R. A., and Holmes, H. E., "Kinetics of Nitramine Flame Reactions," 16th JANNAF Combustion Meeting, CPIA Pub. 308, Vol. II, pp. 35-50, 1979.

67. Fifer, R. A., "Chemistry of Nitrate Ester and Nitramine Propellants," Chapter 4 (pp. 177-238) in Fundamentals of Solid Propellant Combustion, (Kuo, K., and Summerfield, M.(eds)), AIAA Progress in Astronautics and Aeronautics Series, Vol. 90, AIAA, New York, 1984.

68. Jeffrey, W., and Wolfhard, H., "Carbon Formation in Rocket Plumes," paper presented at the 26th JANNAF Combustion Meeting, October 1989.

69. Alspach, D., "Temperature Measurements Through A Solid Propellant Combustion Wave Using Imbedded Fine Wire Thermocouples ," AL-TR-89-085, Edwards AFB, CA, January 1990

70. Oyumi, Y., and Brill, T. B., "Thermal Decomposition of Energetic Materials 12. Infrared Spectral and Rapid Thermolysis Studies of Azide-Containing Monomers and Polymers," Combustion and Flame Vol. 65, pp.127-135, 1986.

71. Russell, T. P., and Brill, T. B., "Thermal Decomposition of Energetic Materials 31. Fast Thermolysis of Ammonium Nitrate, Ethylenediammonium Nitrate and Hydrazinium Nitrate and the Relationship to the Burning Rate," Combustion and Flame Vol. 76, pp. 393-401, 1989.

72. Mihlfeith, C. M., et al, "A Study of Ammonium Nitrate Propellant Combustion," AFAL-TR-89-016, Vol. 1, Hercules, Inc., Magna, UT, March 1990.

73. Austin, G. T., Shreve's Chemical Process Industries, Fifth Edition, McGraw-Hill, New York, 1984, p. 128.

74. Beckstead, M. W., "A Model for Ammonium Nitrate Combustion," AFAL-TR-89-016, Vol. 2, Brigham Young University, Provo, UT, March 1990.

75. Laufer, G., Fletcher, D., and McKenzie, R., "A Method for Measuring Temperatures and Densities in Hypersonic Wind Tunnel Air Flows Using Laser-Induced O_2 Fluorescence," AIAA Paper 90-0626, Jan. 1990.

APPENDIX 1. HATCH MECHANISM [57]

Rate constants for reactions listed in form $k = AT^{-B}\exp(-E/RT)$

Reaction	A	B	E
NH3+M=NH2+H+M	.920E16	0.	84800
HNO+M=H+NO+M	.300E17	0.	48680
N2H+M=N2+H+M	.200E15	0.	20000
H2+M=H+H+M	.223E13	0.5	92600
O2+M=O+O+M	.185E12	0.5	95560
N2O+M=N2+O+M	.162E15	0.	51600
CH2O+M=HCO+H+M	.331E17	0.	81000
HCO+M=H+CO+M	.145E15	0.	19000
NO2+M=NO+O+M	.110E17	0.	66000
H2O2+M=OH+OH+M	.120E18	0.	45500
NCO+M=N+CO+M	.310E17	-0.5	48000
NCO+OH=NO+CO+H	.100E14	0.	0
NH3+H=NH2+H2	.246E14	0.	17071
NH3+O=NH2+OH	.150E13	0.	6040
NH2+OH=NH+H2O	.125E14	0.	2200
NH3+OH=NH2+H2O	.325E13	0.	2120
H+HNO=NH+OH	.200E12	0.5	1300
HNO+OH=NO+H2O	.360E14	0.	0
NH2+HNO=NH3+NO	.500E14	0.	1000
NH2+NO=N2H+OH	.468E20	-2.46	1876
NH2+NO=N2+H2O	.702E20	-2.46	1876
NH+O2=HNO+O	.112E12	0.	3250.
N2H+NO=N2+HNO	.500E14	0.	0.
N2H+OH=N2+H2O	.300E14	0.	0.
NH2+NH2=NH3+NH	.630E13	0.	10000.
CO+OH=CO2+H	.151E8	1.3	-758.
H2+OH=H2O+H	.520E14	0.	6500.
H+O2=OH+O	.719E17	-0.861	16523.
O+H2=OH+H	.180E11	1.	8826.
OH+OH=O+H2O	.170E7	2.03	-1190.
N2O+O=NO+NO	.100E15	0.	28200.
N2O+O=N2+O2	.100E15	0.	28200.
N2O+H=N2+OH	.760E14	0.	15200.
N2O+NH=N2+HNO	.100E12	0.5	3000.
CH2O+OH=HCO+H2O	.753E13	0.	167.
CH2O+H=HCO+H2	.331E15	0.	10500.
CH2O+O=HCO+OH	.501E14	0.	4600.
HCO+OH=CO+H2O	.100E15	0.	0.
HCO+H=CO+H2	.200E15	0.	0.
HCO+O=OH+CO	.100E15	0.	0.
H+NO2=NO+OH	.350E15	0.	1500.
O+NO2=NO+O2	.100E14	0.	600.
O+N2=NO+N	.184E15	0.	76250.
N+O2=NO+O	.640E10	1.	6280.
H+NO=N+OH	.222E15	0.	50500.
HNO+HNO=N2O+H2O	.395E13	0.	5000.
HNO+NO=N2O+OH	.200E13	0.	26000.
H+HO2=H2+O2	.251E14	0.	700.
H+HO2=OH+OH	.251E15	0.	1900.
H+HO2=H2O+O	.501E14	0.	1000.
HO2+OH=H2O+O2	.501E14	0.	1000.
HO2+O=O2+OH	.501E14	0.	1000.

HO2+HO2=H2O2+O2	.100E14	0.	1000.
H2O2+OH=H2O+HO2	.100E14	0.	1800.
H2O2+H=H2O+OH	.316E15	0.	8940.
H2O2+H=HO2+H2	.170E13	0.	3750.
CO+HO2=CO2+OH	.575E14	0.	22930.
CH2O+HO2=HCO+H2O2	.100E13	0.	8000.
HCO+O2=CO+HO2	.331E13	0.	7000.
HCN+OH=CN+H2O	.440E13	0.	9000.
HCN+O=NCO+H	.121E05	2.64	4980.
HCN+O=NH+CO	.517E04	2.64	4980.
HCN+O=CN+OH	.270E10	1.58	26600.
CN+H2=HCN+H	.545E12	0.7	4885.
CN+O=CO+N	.180E14	0.	0.
CN+O2=NCO+O	.560E13	0.	0.
CN+OH=NCO+H	.500E14	0.	0.
NCO+H=NH+CO	.500E14	0.	0.
NCO+O=NO+CO	.300E14	0.	0.
NCO+N=N2+CO	.200E14	0.	0.
NCO+NO=N2O+CO	.190E14	0.	0.
NCO+H2=HNCO+H	.858E13	0.	9000.
HNCO+H=NH2+CO	.200E14	0.	3000.
NH+H=N+H2	.300E14	0.	0.
H+OH+M=H2O+M	.750E24	-2.6	0.
O+H+M=OH+M	.100E17	0.	0.
H+O2+M=HO2+M	→151E16	0.	-1000.
H2CN+M=HCN+H+M	.100E17	0.	30000.

APPENDIX 2. EXTENDED MILLER-BOWMAN MECHANISM [11,30]

Rate constants for reactions listed in form $k = AT^{-B}\exp(-E/RT)$

Reaction	A	B	E
CH4+O=CH3+OH	1.02E9	1.5	8604.
CH4+O2=CH3+HO2	7.90E13	0.0	56000.
2CH3(+M)=C2H6(+M)	9.03E16	-1.2	654.
LOW/1.7E38-6.051292./			
TROE/0.6046927.132./			
H2/2/CO/2/CO2/3/H2O/5/			
CH3+H(+M)=CH4(+M)	6.0E16	-1.0	0.0
LOW/8.00E26-3.00.0/			
SRI/0.45797.979./			
H2/2/CO/2/CO2/3/H2O/5/			
CH4+H=CH3+H2	2.20E4	3.000	8750.
CH4+OH=CH3+H2O	1.60E6	2.1	2460.
CH4+HO2=CH3+H2O2	1.80E11	0.0	18700.
CH3+HO2=CH3O+OH	2.00E13	0.0	0.0
CH3+O2=CH3O+O	2.05E19	-1.570	29229.
CH3+O=CH2O+H	8.00E13	0.0	0.0
CH2OH+H=CH3+OH	1.00E14	0.0	0.0
CH3O+H=CH3+OH	1.00E14	0.0	0.0
CH3+OH=CH2+H2O	7.50E6	2.0	5000.
CH3+H=CH2+H2	9.00E13	0.0	15100.
CH3O+M=CH2O+H+M	1.00E14	0.0	25000.
CH2OH+M=CH2O+H+M	1.00E14	0.0	25000.
CH3O+H=CH2O+H2	2.00E13	0.0	0.0
CH2OH+H=CH2O+H2	2.00E13	0.0	0.0
CH3O+OH=CH2O+H2O	1.00E13	0.0	0.0
CH2OH+OH=CH2O+H2O	1.00E13	0.0	0.0
CH3O+O=CH2O+OH	1.00E13	0.0	0.0
CH2OH+O=CH2O+OH	1.00E13	0.0	0.0
CH3O+O2=CH2O+HO2	6.30E10	0.0	2600.
CH2OH+O2=CH2O+HO2	1.48E13	0.0	1500.
CH2+H=CH+H2	1.00E18	-1.560	0.0
CH2+OH=CH+H2O	1.13E7	2.0	3000.
CH2+OH=CH2O+H	2.50E13	0.0	0.0
CH+O2=HCO+O	3.30E13	0.0	0.0
CH+O=CO+H	5.70E13	0.0	0.0
CH+OH=HCO+H	3.00E13	0.0	0.0
CH+CO2=HCO+CO	3.40E12	0.0	690.
CH+H=C+H2	1.50E14	0.0	0.0
CH+H2O=CH2O+H	5.72E12	0.0	-380.0
CH+CH2O=CH2CO+H	9.46E13	0.0	-515.
CH+C2H2=C3H2+H	1.00E14	0.0	0.0
CH+CH2=C2H2+H	4.00E13	0.0	0.0
CH+CH3=C2H3+H	3.00E13	0.0	0.0
CH+CH4=C2H4+H	6.00E13	0.0	0.0
C+O2=CO+O	2.00E13	0.0	0.0
C+OH=CO+H	5.00E13	0.0	0.0
C+CH3=C2H2+H	5.00E13	0.0	0.0
C+CH2=C2H+H	5.00E13	0.0	0.0
CH2+CO2=CH2O+CO	1.10E11	0.0	1000.
CH2+O=CO+2H	5.00E13	0.0	0.0
CH2+O=CO+H2	3.00E13	0.0	0.0
CH2+O2=CO2+2H	1.60E12	0.0	1000.

117

CH2+O2=CH2O+O	5.00E13	0.0	9000.
CH2+O2=CO2+H2	6.90E11	0.0	500.
CH2+O2=CO+H2O	1.90E10	0.0	-1000.
CH2+O2=CO+OH+H	8.60E10	0.0	-500.
CH2+O2=HCO+OH	4.30E10	0.0	-500.
CH2O+OH=HCO+H2O	3.43E9	1.180	-447.
CH2O+H=HCO+H2	2.19E8	1.770	3000.
CH2O+M=HCO+H+M	3.31E16	0.0	81000.
CH2O+O=HCO+OH	1.80E13	0.0	3080.
HCO+OH=H2O+CO	1.00E14	0.0	0.0
HCO+M=H+CO+M	2.50E14	0.0	16802.
CO/1.9/H2/1.9/CH4/2.8/CO2/3.0/H2O/5.0/			
HCO+H=CO+H2	1.19E13	0.250	0.0
HCO+O=CO+OH	3.00E13	0.0	0.0
HCO+O=CO2+H	3.00E13	0.0	0.0
HCO+O2=HO2+CO	3.30E13	-0.400	0.0
CO+O+M=CO2+M	6.17E14	0.0	3000.
CO+OH=CO2+H	1.51E7	1.300	-758.
CO+O2=CO2+O	1.60E13	0.0	41000.
HO2+CO=CO2+OH	5.80E13	0.0	22934.
C2H6+CH3=C2H5+CH4	5.50E-1	4.000	8300.
C2H6+H=C2H5+H2	5.40E2	3.5	5210.
C2H6+O=C2H5+OH	3.00E7	2.000	5115.
C2H6+OH=C2H5+H2O	8.70E9	1.05	1810.
C2H4+H=C2H3+H2	1.10E14	0.0	8500.
C2H4+O=CH3+HCO	1.60E9	1.200	746.
C2H4+OH=C2H3+H2O	2.02E13	0.0	5955.
CH2+CH3=C2H4+H	3.00E13	0.0	0.0
H+C2H4(+M)=C2H5(+M)	2.21E13	0.0	2066.
LOW/6.37E27-2.8-54./			
H2/2/CO/2/CO2/3/H2O/5/			
C2H5+H=2CH3	1.00E14	0.0	0.0
C2H5+O2=C2H4+HO2	8.43E11	0.0	3875.
C2H2+O=CH2+CO	1.02E7	2.000	1900.
C2H2+O=HCCO+H	1.02E7	2.000	1900.
H2+C2H=C2H2+H	4.09E5	2.390	864.
H+C2H2(+M)=C2H3(+M)	5.54E12	0.0	2410.
LOW/2.67E27-3.52410./			
H2/2/CO/2/CO2/3/H2O/5/			
C2H3+H=C2H2+H2	4.00E13	0.0	0.0
C2H3+O=CH2CO+H	3.00E13	0.0	0.0
C2H3+O2=CH2O+HCO	4.00E12	0.0	-250.
C2H3+OH=C2H2+H2O	5.00E12	0.0	0.0
C2H3+CH2=C2H2+CH3	3.00E13	0.0	0.0
C2H3+C2H=2C2H2	3.00E13	0.0	0.0
C2H3+CH=CH2+C2H2	5.00E13	0.0	0.0
OH+C2H2=C2H+H2O	3.37E7	2.000	14000.
OH+C2H2=HCCOH+H	5.04E5	2.300	13500.
OH+C2H2=CH2CO+H	2.18E-4	4.500	-1000.
OH+C2H2=CH3+CO	4.83E-4	4.000	-2000.
HCCOH+H=CH2CO+H	1.00E13	0.0	0.0
C2H2+O=C2H+OH	3.16E15	-0.6	15000.
CH2CO+O=CO2+CH2	1.75E12	0.0	1350.
CH2CO+H=CH3+CO	1.13E13	0.0	3428.
CH2CO+H=HCCO+H2	5.00E13	0.0	8000.
CH2CO+O=HCCO+OH	1.00E13	0.0	8000.
CH2CO+OH=HCCO+H2O	7.50E12	0.0	2000.
CH2CO(+M)=CH2+CO(+M)	3.00E14	0.0	70980.

```
LOW/3.60E150.059270./
C2H+O2=2CO+H                    5.00E13      0.0      1500.
C2H+C2H2=C4H2+H                 3.00E13      0.0         0.0
H+HCCO=CH2(S)+CO                1.00E14      0.0         0.0
O+HCCO=H+2CO                    1.00E14      0.0         0.0
HCCO+O2=2CO+OH                  1.60E12      0.0       854.
CH+HCCO=C2H2+CO                 5.00E13      0.0         0.0
2HCCO=C2H2+2CO                  1.00E13      0.0         0.0
CH2(S)+M=CH2+M                  1.00E13      0.0         0.0
H/0.0/
CH2(S)+CH4=2CH3                 4.00E13      0.0         0.0
CH2(S)+C2H6=CH3+C2H5           1.20E14      0.0         0.0
CH2(S)+O2=CO+OH+H              3.00E13      0.0         0.0
CH2(S)+H2=CH3+H               7.00E13      0.0         0.0
CH2(S)+H=CH2+H               2.00E14      0.0         0.0
C2H+O=CH+CO                    5.00E13      0.0         0.0
C2H+OH=HCCO+H                  2.00E13      0.0         0.0
2CH2=C2H2+H2                   4.00E13      0.0         0.0
CH2+HCCO=C2H3+CO               3.00E13      0.0         0.0
CH2+C2H2=C3H3+H               1.20E13      0.0      6600.
C4H2+OH=C3H2+HCO              6.66E12      0.0      -410.
C3H2+O2=HCO+HCCO              1.00E13      0.0         0.0
C3H3+O2=CH2CO+HCO             3.00E10      0.0      2868.
C3H3+O=CH2O+C2H               2.00E13      0.0         0.0
C3H3+OH=C3H2+H2O             2.00E13      0.0         0.0
2C2H2=C4H3+H                   2.00E12      0.0     45900.
C4H3+M=C4H2+H+M               1.00E16      0.0     59700.
CH2(S)+C2H2=C3H3+H           3.00E13      0.0         0.0
C4H2+O=C3H2+CO               1.20E12      0.0         0.0
C2H2+O2=HCCO+OH              2.00E8       1.500    30100.
C2H2+M=C2H+H+M               4.20E16      0.0    107000.
C2H4+M=C2H2+H2+M             1.50E15      0.0     55800.
C2H4+M=C2H3+H+M              1.40E15      0.0     82360.
H2+O2=2OH                      1.70E13      0.0     47780.
OH+H2=H2O+H                    1.17E9       1.3      3626.
O+OH=O2+H                      4.00E14     -0.5         0.0
O+H2=OH+H                      5.06E4       2.67     6290.
H+O2+M=HO2+M                   3.61E17     -0.72        0.0
H2O/18.6/CO2/4.2/H2/2.9/CO/2.1/N2/1.3/
OH+HO2=H2O+O2                  ·7.50E12     0.0         0.0
H+HO2=2OH                      1.40E14      0.0      1073.
O+HO2=O2+OH                    1.40E13      0.0      1073.
2OH=O+H2O                      6.00E8       1.3         0.0
2H+M=H2+M                      1.00E18     -1.00        0.0
H2/0.0/H2O/0.0/CO2/0.0/
2H+H2=2H2                      9.20E16     -0.600        0.0
2H+H2O=H2+H2O                  6.00E19     -1.25         0.0
2H+CO2=H2+CO2                  5.49E20     -2.00         0.0
H+OH+M=H2O+M                   1.60E22     -2.00         0.0
H2O/5.0/
H+O+M=OH+M                     6.20E16     -0.60         0.0
H2O/5.0/
2O+M=O2+M                      1.89E13      0.0      -1788.
H+HO2=H2+O2                    1.25E13      0.0          0.0
2HO2=H2O2+O2                   2.00E12      0.0          0.0
H2O2+M=2OH+M                   1.30E17      0.0      45500.
H2O2+H=HO2+H2                  1.60E12      0.0       3800.
H2O2+OH=H2O+HO2               1.00E13      0.0       1800.
```

119

CH+N2=HCN+N	3.00E11	0.0	13600.
CN+N=C+N2	1.04E15	-0.5	0.0
CH2+N2=HCN+NH	1.00E13	0.0	74000.
H2CN+N=N2+CH2	2.00E13	0.0	0.0
H2CN+M=HCN+H+M	3.00E14	0.0	22000.
C+NO=CN+O	6.60E13	0.0	0.0
CH+NO=HCN+O	1.10E14	0.0	0.0
CH2+NO=HCNO+H	1.39E12	0.0	-1100.
CH3+NO=HCN+H2O	1.00E11	0.0	15000.
CH3+NO=H2CN+OH	1.00E11	0.0	15000.
HCCO+NO=HCNO+CO	2.00E13	0.0	0.0
CH2(S)+NO=HCN+OH	2.00E13	0.0	0.0
HCNO+H=HCN+OH	1.00E14	0.0	12000.
CH2+N=HCN+H	5.00E13	0.0	0.0
CH+N=CN+H	1.30E13	0.0	0.0
CO2+N=NO+CO	1.90E11	0.0	3400.
HCCO+N=HCN+CO	5.00E13	0.0	0.0
CH3+N=H2CN+H	3.00E13	0.0	0.0
C2H3+N=HCN+CH2	2.00E13	0.0	0.0
C3H3+N=HCN+C2H2	1.00E13	0.0	0.0
HCN+OH=CN+H2O	1.45E13	0.0	10929.
OH+HCN=HOCN+H	5.85E4	2.4	12500.
OH+HCN=HNCO+H	1.98E-3	4.0	1000.
OH+HCN=NH2+CO	7.83E-4	4.00	4000.
HOCN+H=HNCO+H	1.00E13	0.0	0.0
HCN+O=NCO+H	1.38E4	2.64	4980.
HCN+O=NH+CO	3.45E3	2.64	4980.
HCN+O=CN+OH	2.70E9	1.58	26600.
CN+H2=HCN+H	2.95E5	2.45	2237.
CN+O=CO+N	1.80E13	0.0	0.0
CN+O2=NCO+O	5.60E12	0.0	0.0
CN+OH=NCO+H	6.00E13	0.0	0.0
CN+HCN=C2N2+H	2.00E13	0.0	0.0
CN+NO2=NCO+NO	3.00E13	0.0	0.0
CN+N2O=NCO+N2	1.00E13	0.0	0.0
C2N2+O=NCO+CN	4.57E12	0.0	8880.
C2N2+OH=HOCN+CN	1.86E11	0.0	2900.
HO2+NO=NO2+OH	2.11E12	0.0	-479.
NO2+H=NO+OH	3.50E14	0.0	1500.
NO2+O=NO+O2	1.00E13	0.0	600.
NO2+M=NO+O+M	1.1E16	0.0	66000.
NCO+H=NH+CO	5.00E13	0.0	0.0
NCO+O=NO+CO	2.00E13	0.0	0.0
NCO+N=N2+CO	2.00E13	0.0	0.0
NCO+OH=NO+CO+H	1.00E13	0.0	0.0
NCO+M=N+CO+M	3.10E16	-0.5	48000.
NCO+NO=N2O+CO	1.00E13	0.0	-390.
NCO+H2=HNCO+H	8.58E12	0.0	9000.
HNCO+H=NH2+CO	2.00E13	0.0	3000.
NH+O2=HNO+O	1.00E13	0.0	12000.
NH+O2=NO+OH	7.60E10	0.0	1530.
NH+NO=N2O+H	2.40E15	-0.80	0.0
N2O+OH=N2+HO2	2.00E12	0.0	10000.
N2O+H=N2+OH	7.60E13	0.0	15200.
N2O+M=N2+O+M	1.60E14	0.0	51600.
N2O+O=N2+O2	1.00E14	0.0	28200.
N2O+O=2NO	1.00E14	0.0	28200.
NH+OH=HNO+H	2.00E13	0.0	0.0

NH+OH=N+H2O	5.00E11	0.50	2000.
NH+N=N2+H	3.00E13	0.0	0.0
NH+H=N+H2	1.00E14	0.0	0.0
NH2+O=HNO+H	6.63E14	-0.50	0.0
NH2+O=NH+OH	6.75E12	0.0	0.0
NH2+OH=NH+H2O	4.00E6	2.00	1000.
NH2+H=NH+H2	6.92E13	0.0	3650.
NH2+NO=NNH+OH	6.40E15	-1.25	0.0
NH2+NO=N2+H2O	6.20E15	-1.25	0.0
NH3+OH=NH2+H2O	2.04E6	2.04	566.
NH3+H=NH2+H2	6.36E5	2.39	10171.
NH3+O=NH2+OH	2.10E13	0.0	9000.
NNH=N2+H	1.00E4	0.0	0.0
NNH+NO=N2+HNO	5.00E13	0.0	0.0
NNH+H=N2+H2	1.00E14	0.0	0.0
NNH+OH=N2+H2O	5.00E13	0.0	0.0
NNH+NH2=N2+NH3	5.00E13	0.0	0.0
NNH+NH=N2+NH2	5.00E13	0.0	0.0
NNH+O=N2O+H	1.00E14	0.0	0.0
HNO+M=H+NO+M	1.50E16	0.0	48680.
H2O/10.0/O2/2.0/N2/2.0/H2/2.0/			
HNO+OH=NO+H2O	3.60E13	0.0	0.0
HNO+H=H2+NO	5.00E12	0.0	0.0
HNO+NH2=NH3+NO	2.00E13	0.0	1000.
N+NO=N2+O	3.27E12	0.30	0.0
N+O2=NO+O	6.40E9	1.00	6280.
N+OH=NO+H	3.80E13	0.0	0.0
CH4+NO2=CH3+HONO	1.20E14	0.0	30000.
CH3+NO2=CH3O+NO	1.50E13	0.0	0.0
HO2+NO2=HONO+O2	4.64E11	0.0	-479.
CH+NO2=HCO+NO	1.01E14	0.0	0.0
HONO+M=OH+NO+M	1.8E17	0.0	44900.
NO2+NO2=NO+NO+O2	2.0E12	0.0	26825.
NO2+NO2=NO+NO3	3.9E11	0.0	23844.
HNO3+M=NO2+OH+M	1.6E15	0.0	30600.
NO2+NO=N2O+O2	1.0E12	0.0	60000.
NO+M=N+O+M	4.0E20	-1.5	150000.
NO+NO=N2+O2	1.3E14	0.0	75630.
NO+HNO=N2O+OH	2.0E12	0.0	26000.
NO+HO2=HNO+O2	2.0E11	0.0	2000.
HCO+NO2=CO+HONO	1.5E13	0.0	-430.
HCO+NO2=CO2+H+NO	1.5E11	0.0	-430.
CO+NO2=CO2+NO	1.26E14	0.0	27600.
HONO+H=H2+NO2	1.0E12	0.0	1000.